Design Challenges for Ultra-High-Temperature Energy Storage with Thermophotovoltaics

by

Colin Clancy Kelsall

S.M. Mechanical Engineering
Massachusetts Institute of Technology, 2018

B.S. Mechanical Engineering
Georgia Institute of Technology, 2016

Submitted to the Department of Mechanical Engineering in
Partial Fulfillment of the Requirements for the
Degree of Doctor of Philosophy in Mechanical Engineering
at the
MASSACHUSETTS INSTITUTE OF TECHNOLOGY
February 2023

Author .....
Department of Mechanical Engineering
February 10th, 2023

Certified by .....
Asegun Henry
Department of Mechanical Engineering
Thesis Supervisor

Accepted by .....
Nicolas Hadjiconstantinou
Professor of Mechanical Engineering
Chairman, Committee on Graduate Students

Design Challenges for Ultra-High-Temperature Energy Storage with Thermophotovoltaics

by

Colin Clancy Kelsall

Submitted to the Department of Mechanical Engineering on February 10th, 2023

in Partial Fulfillment of the Requirements for the Degree of Doctor of Philosophy

Abstract

Decarbonization of the electricity grid is an important part of mitigating the extent and effects of human-caused climate change. Some of the most promising carbon-free and renewable energy resources, like wind and solar, have intermittent production that could be addressed, in part, with widespread deployment of electrical energy storage. There are few storage technologies, however, that are suited to this task, partially due to their high cost, rare constituent materials, and geographic constraints. This thesis investigates several pressing design challenges for a new electrical energy storage technology, termed Thermal Energy Grid Storage (TEGS), with the potential for low cost and deployment at scale. TEGS stores electricity as heat in graphite blocks at ultra-high temperatures (>2000°C) and can extract that heat as electricity, on demand, using a thermophotovoltaic (TPV) heat engine. Thermophotovoltaic systems convert thermally emitted light from a high-temperature heat source to electricity using a photovoltaic cell. By operating at extremely high temperatures and utilizing multi-junction PV cells typically intended for solar energy conversion, high conversion efficiencies can be achieved (i.e. > 50%) at low cost. When operating at such high temperatures, however, sublimation of the thermal emitter material (i.e. tungsten) and deposition on the cell surface can cause significant performance degradation. To prevent this contamination process, a layer of gas can be blown across the cell, effectively sweeping the evaporated material away before it gets to the surface. This thesis examines the relevant design parameters of this Sweeping Noble Gas Curtain (SNGC) system with the goal of developing a functional and scalable TPV generator for implementation in the TEGS ultra-high-temperature thermal battery. This work consists of several analytical and numerical models predicting deposition behavior under different geometric and flow conditions, experimental validation of these models, a scalable design for an integrated SNGC-TPV system, a summary of the numerous challenges and solutions devised for testing this system above 2000°C, and finally a proof-of-concept demonstration showing the remarkable efficacy of the SNGC approach. The demonstrated long-term durability enhancement of thermophotovoltaic devices is a critical step towards the economic viability of such systems and their potential for deployment at scale.

Thesis Committee:

Professor Asegun Henry, Department of Mechanical Engineering (Thesis Supervisor)
Professor John Lienhard, Department of Mechanical Engineering
Professor Gang Chen, Department of Mechanical Engineering
Professor Evelyn Wang, Department of Mechanical Engineering (Former Committee Member)

Acknowledgments

The work in this thesis would not have been possible without many people, too many to name but here are some highlights….

My advisor, Dr. Asegun Henry, who inspired me to go to grad school during an undergrad research project.

Atomistic Simulation & Energy Research Group for constant collaboration and help running almost every experiment described in this thesis.

Device Research Lab and Dr. Evelyn Wang for excellent training during my Masters work and continued support long after.

Friends throughout the years, who made Cambridge a very fun place to be.

And finally, the constant love and support of my family.

Table of Contents

List of Figures

List of Tables

Chapter 1

1. Introduction

1.1. MOTIVATION

Energy storage is needed to enable dispatchable renewable energy supply and thereby full decarbonization of the grid. However, this can only occur with order of magnitude cost reductions compared to current battery technology. There are a number of storage technologies with the potential to achieve these cost targets, and this thesis focuses on thermal energy storage, storing electricity as heat and converting it back to electricity on demand.

1.1.1. Transitioning Energy Landscape

The energy generation landscape of today has changed drastically compared to even 10 years ago. In 2021, the vast majority of newly built generating capacity was either renewable sources or batteries to support them [1]. If this trend continues over the next several decades, storage will become a vital part of global energy infrastructure. Figure 1 shows US generating capacity additions by type over the past 11 years, and projected to 2023. This metric indicates what the US grid generation mix will look like once the currently operating power plants reach their end of life. Though natural gas still accounts for a significant part of new installations, the vast majority consist of wind and solar. Batteries have also become much more prevalent and have the opportunity to replace some of the peaking gas plants for grid resiliency and load management [2].

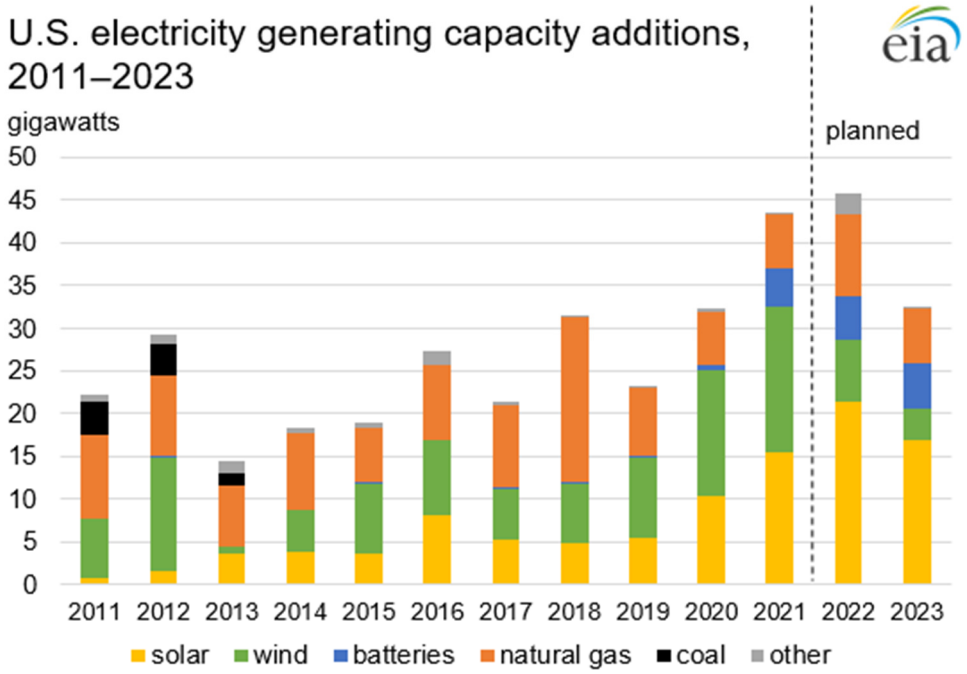

Figure 1 – New generating capacity additions including historical and planned. Renewables dominate all new construction in the US. [1]

1.1.2. Grid-Scale Energy Storage

The increase in battery deployments shown in Figure 1 suggests that grid-scale energy storage is becoming a priority for utilities interested in ensuring grid reliability in the face of changing energy economics and regulations. The available storage technologies, however, are insufficient in cost and availability to allow intermittent renewable resources (e.g. wind and solar) to compete with traditional fossil fuel generating technologies for dispatchable electricity on-demand.

1.1.2.1. Technology Evaluation Metrics

When considering the costs of storage, there are a number of metrics that help to compare technologies with highly varied operating conditions and physical embodiments. Storage systems are inherently different than generators, in that they do not just have a rated power output, but an associated storage capacity as well. To simplify this distinction, these systems are often described with a power rating (e.g. 100 kWe, kilowatts of electricity), and a duration that they can discharge at that power (e.g. 4 hours). Using this method, a 100 kW_e system with 4 hours of storage has roughly 400 kWh_e (kilowatt-hours of electricity) of "dischargeable" storage capacity. This gets a little more complicated when considering a term known as the round-trip efficiency (RTE), given by Eq. (1). This term incorporates

both charging and discharging efficiency and is defined as the ratio of the electrical energy available for discharge ($E_{\text{discharge}}$, kWh_e) to the energy used for charging (E_{charge}, kWh_e). A low discharge efficiency will result in a low RTE, requiring more electricity to charge than is available for discharge, and will also require a larger volume of storage material (i.e. cost). The cost associated with building a storage system can be divided into two components as well; Cost per Energy, Eq. (2) in $/kWhe, and Cost per Power, Eq (3) in $/kWe. This approach allows comparison between systems with vastly different storage characteristics, for example a 50 MW pumped-hydropower storage plant with 100 hours of discharge (5000 MWhe) available and a 100 MW lithium-ion battery pack with 4 hours of storage (400 MWhe). Just comparing the full system costs does not show the full picture. These three metrics will be used for the next few sections to compare existing technologies, and identify some cost targets that storage technologies need to hit for widespread implementation.

$$\text{Round Trip Efficiency:} \quad \eta_{RTE} = \frac{E_{\text{discharge}}}{E_{\text{charge}}} \approx \eta_{\text{charge}}\eta_{\text{discharge}} \tag{1}$$

$$\text{Cost Per Energy:} \quad CPE = \frac{C_{system}}{\eta_{RTE} * E_{stored}} \left[\frac{\$}{kWh_e}\right] \tag{2}$$

$$\text{Cost Per Power:} \quad CPP = \frac{C_{system}}{P_{discharge}} \left[\frac{\$}{kW_e}\right] \tag{3}$$

1.1.2.2. Predicted Storage Need

There is significant ongoing research both in academia and industry on how much electricity storage will be needed on the grid and by when [3]–[7]. It is an immensely complex problem that has economic, technological, geopolitical, and even human factors at play.

Trancik et al. published a paper recently that predicts, for several locations and resource mixes, the CPE and CPP required to allow renewables to achieve cost-parity with dispatchable fossil resources [6]. *Figure 2* is reproduced from this publication and shows that to compete favorably with fossil plants, a LCOSE (Levelized Cost of Shaped Electricity) must be lower than $0.14/kWh. This metric is further defined in Trancik et al., and corresponds to the maximum a consumer might pay for electricity from one

of these sources, at any time of the day. The key takeaway from this figure is that in order for an optimal mix (for the region) of wind and solar to be cheaper than fossil power, CPE (Storage energy capacity cost in this plot) must be <20 $/kWh. CPP (storage power capacity cost in this plot) is much less influential, though still important, especially in the Peaker configuration. This CPE cost target is very aggressive, and there are few scalable storage technologies with the capability to achieve it.

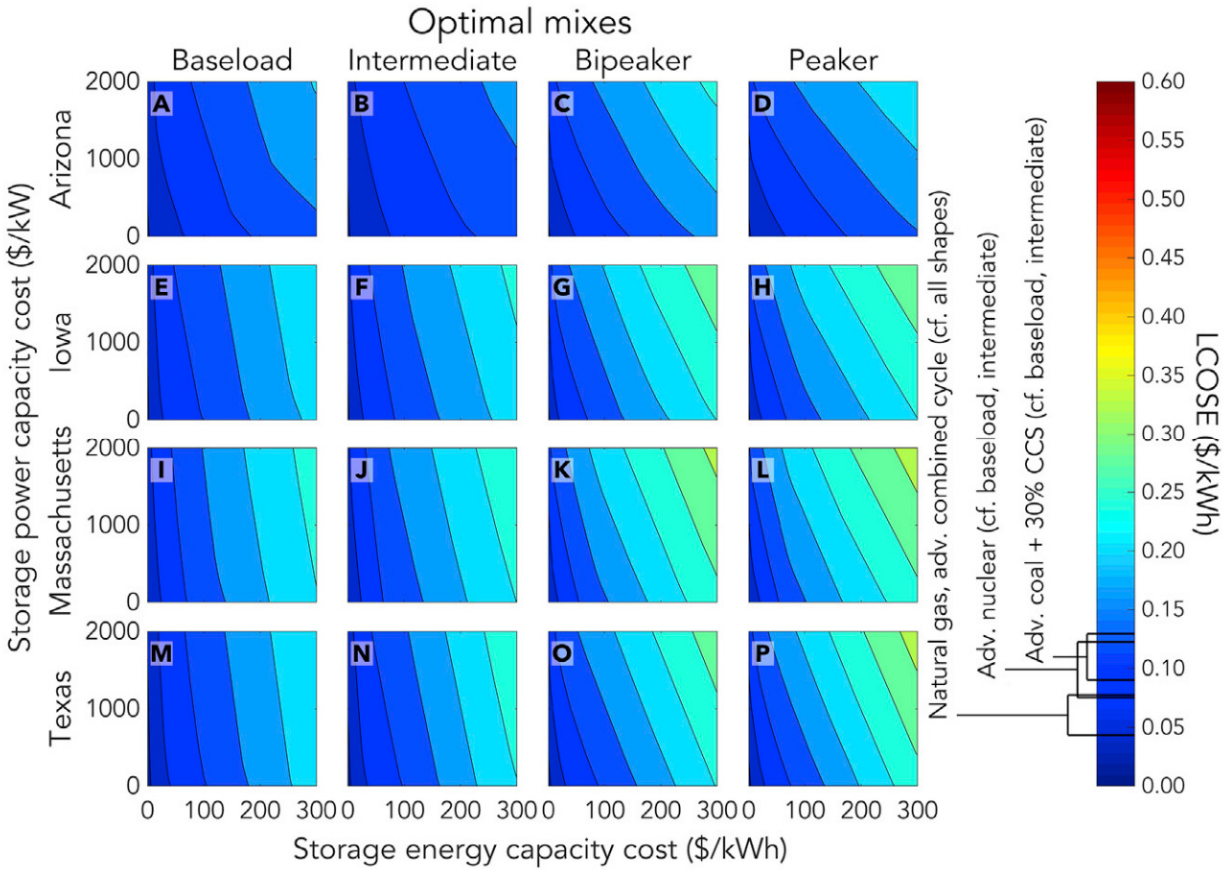

Figure 2 – Levelized cost of shaped energy (LCOSE) of optimal wind/solar renewable resource mixes in several locations in the US. Only regions corresponding to LCOSE values of less than $0.14 are cost competitive with current natural gas generating technologies. These regions require Storage energy capacity costs of less than $20/kWh. Reproduced from Ziegler et al. [6]

1.2. CURRENT GRID-SCALE ENERGY STORAGE TECHNOLOGIES

Storing energy on the grid is not a brand new concept, and storage systems have been implemented for decades. Many of these technologies, however, are challenging to implement at large scale for reasons including materials scarcity, geographic restrictions, environmental impacts, etc. Figure 3 compares three general classes of technologies and their rough cost regimes. Even the best new flow-battery technologies

barely hit the 20 $/kWh$_e$ cost target. This regime is dominated by mechanical, thermal, and chemical storage technologies. There are a number of experimental and emerging developments in this area; the rest of this thesis will address some challenges and opportunities with one such implementation, Thermal Energy Grid Storage (TEGS).

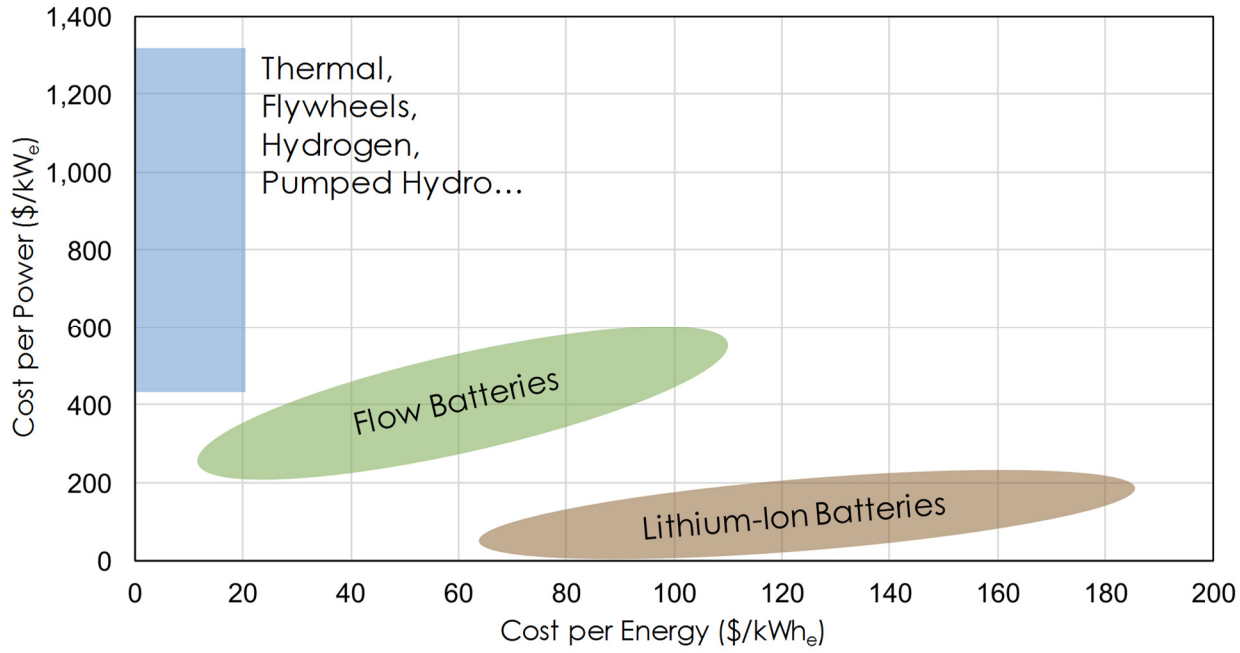

Figure 3 – Comparison of three energy storage technology classes. Reproduced from the MITEI Future of Energy Storage study [8]

1.3. THERMAL ENERGY GRID STORAGE (TEGS)

Thermal Energy Grid Storage is a thermal battery that is charged with electricity, stores that electricity as thermal energy or heat in large blocks of low-cost graphite, and can convert that heat back into electricity on demand. Storing electricity as heat has a number of advantages, namely a much lower-cost and widely available storage medium. Thermal energy storage systems using rocks or thick masonry to dampen temperature fluctuations in built environments have been used for thousands of years, but the challenge arises when trying to convert that heat, efficiently, back into much more useful electricity. TEGS addresses these issues through a number of innovations and has the potential to achieve the cost target identified in *Figure 2*.

1.3.1. System Summary

The envisaged system is illustrated in Figure 4, whereby excess electricity from the grid is first used to power resistive heating elements (i.e., made of either graphite or tungsten), which then convert the electricity to extremely high temperature heat (~ 2500°C). The energy is then transferred to graphite pipes via thermal radiation, and the pipes carry liquid tin, which is used as a heat transfer fluid (HTF). Nominally, just like in the prior work of Amy et al., the tin is envisaged to be heated from 1900°C up to 2400°C, thereby converting the energy input into sensible heat in the tin, by raising its enthalpy. The tin is pumped through the piping continuously, and is then routed to the storage unit, which contains large graphite blocks. As the 2400°C tin is pumped through pipes that run through the graphite blocks, the tin heats the graphite blocks up from 1900°C to 2400°C via thermal radiation, which correspondingly causes the tin to cool back to 1900°C. The tin is then pumped back through the resistance heaters to be reheated, and this process, which constitutes the charging process, continues until the graphite storage is fully heated to the peak temperature.

Since the graphite storage unit is large, on the order of 1000 m^3, its thermal mass is sufficiently large, that it can retain the energy used to charge it for long periods of time (e.g., multiple days or even > 1 week) with minimal i.e., < 10% loss of the energy stored – note that the heat loss design point in prior work by Amy et al., was 1% loss per day, and this is significant/important design choice. Thus, the energy is stored as sensible heat in the graphite until electricity is needed again. When electricity is desired, the system is discharged by pumping liquid tin through the graphite storage unit, which heats it to the peak temperature 2400°C, after which it is routed to the power block. The power block consists of an array of graphite pipes that form vertically oriented unit cells. Each unit cell of piping creates a square or rectangular cavity that is lined with tungsten foil, which is used as a diffusion barrier to prevent graphite deposition onto the TPV cells. Inside each cavity, a water/oil cooled heat sink that is covered in TPV cells can be lowered into the unit cell cavity. This causes the TPV cells to be illuminated with the light emitted by the tungsten foil, which is in turn heated by the light emitted by the graphite piping carrying the tin. This net transfer of energy converts a large fraction $\geq$ 50% of the energy to electricity, which in turn causes the tin's temperature to decrease back to 1900C, and the remaining waste heat is removed by the coolant running through the heat sink. The coolant subsequently dissipates the waste heat to the environment via a dry cooling unit, while the tin is pumped back to the graphite storage unit to be reheated by the stored sensible heat. In this way the entire system serves effectively as a rechargeable grid scale thermal battery that can store energy cheaply and supply it to the grid on demand, with an estimated

RTE of ~ 50%. It should be noted here that as concluded by Amy et al., the RTE is almost fully determined by the TPV conversion efficiency.

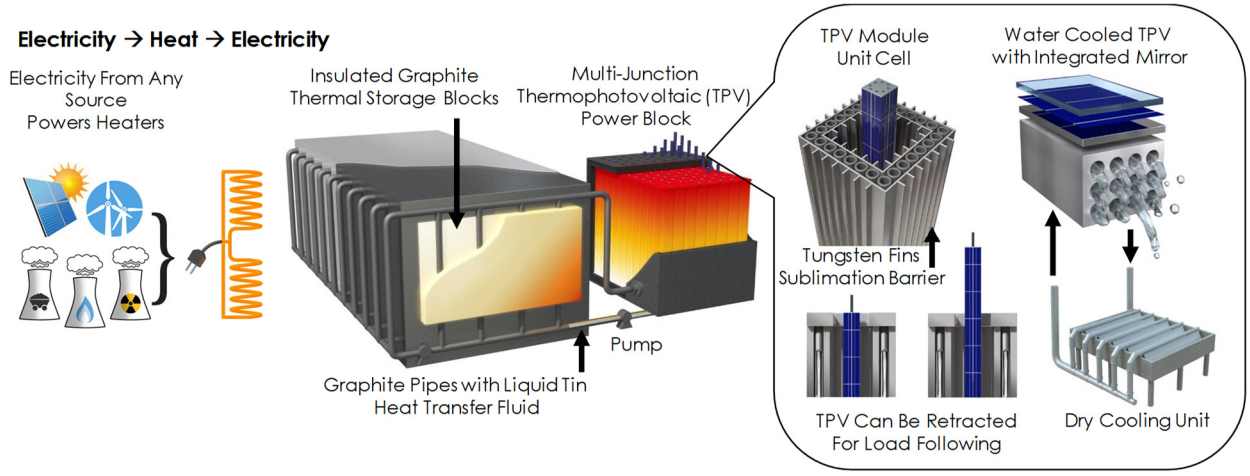

Figure 4 – Thermal Energy Grid Storage Schematic identifying the storage and power block subcomponents, with detailed views on the thermophotovoltaic energy conversion system to convert the high-temperature stored heat back to electricity.

1.3.2. Thermophotovoltaic (TPV) Heat Engines

1.3.2.1. Theory

Thermophotovoltaic systems (TPVs) are solid-state heat engines capable of converting heat to electricity through the emission and conversion of thermal radiation. These systems can utilize a spectrally selective emitter material (i.e. tungsten) heated to incandescence and capture the radiant emission using a photovoltaic cell. By operating at extremely high emitter temperatures (~2400°C) and utilizing cell chemistries/band gaps typically intended for solar power conversion, very high conversion efficiencies can be achieved (i.e., > 50%) [9]. Figure 5 shows how thermophotovoltaics fit in to the portfolio of heat engines already implemented in various thermal energy generation technologies. As temperatures exceed the limits of this chart, thermophotovoltaics become competitive with some of the highest efficiency heat engines, all without any moving parts.

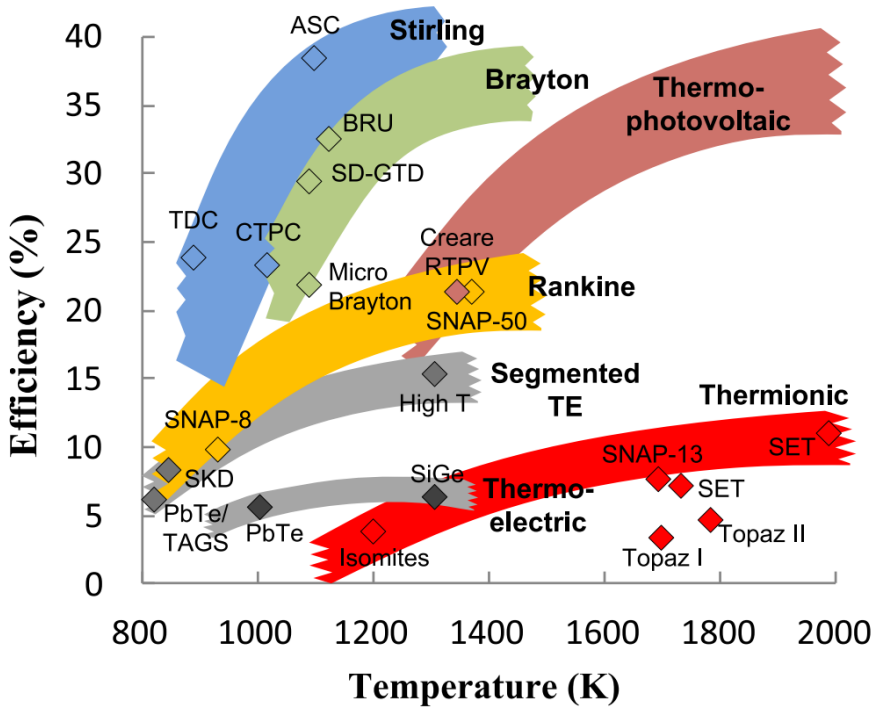

Figure 5 – Heat engine technologies over a range of temperatures. Thermophotovoltaics have the potential to operate and high temperatures with very high efficiencies. Reproduced from Datas et al. [10]

Figure 6(a) shows the subcomponents of a representative TPV generator designed to operate with a 2400°C heat source. The thermal emitter is heated to this operating temperature, and emits a significant amount of light via thermal radiation. At this temperature, black body (maximum) thermal emission is around 300 W/cm^2, about 3000 times stronger than sunlight and roughly three times the critical heat flux of water. This high optical power density requires very carefully designed cells and cooling apparatus to convert a majority of the light to electricity and prevent overheating. TPV cells often have multiple junctions to enable this high conversion efficiency, as single junction cells have fundamental limits on conversion efficiency due to thermalization losses (high energy photons not being converted as efficiently as lower energy photons). Additionally, the gold back surface reflector (BSR) reflect the very low energy photons that are unable to be converted to electricity by either PV junction. These photons are primarily in the infrared spectrum and would otherwise be absorbed as heat in the cell. There are additional subtleties to the cell design itself, but they are outside the scope of this thesis. A recent paper by LaPotin et al. demonstrating a world record TPV efficiency addresses these design components more directly [11]. Figure 6(b) shows one of the fabricated TPV cells from this work ready for characterization under a high intensity lamp.

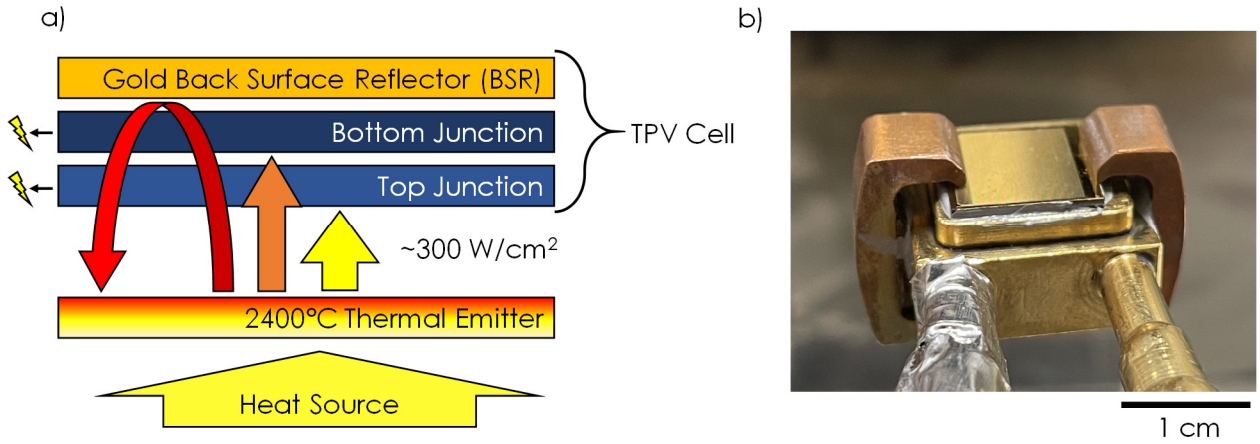

Figure 6 – a) TPV cell and emitter schematic. b) Example TPV cell mounted on a microchannel cold plate for characterization.

Figure 7 shows a more careful accounting of the power emission, conversion, and absorption for a TPV system operating at 2150°C, the nominal operating condition for the TEGS system described in Section 1.3.1. The emitted power density is about 1/3rd lower at this temperature compared to 2400°C, but conversion efficiency is still predicted to be above 50%. One interesting thing to note is that while tungsten is advantageous as an emitter material, it an emittance significantly below 1 (~0.3) which further reduces power density of the light emitted by a tungsten emitter compared to something with a higher emittance, like graphite.

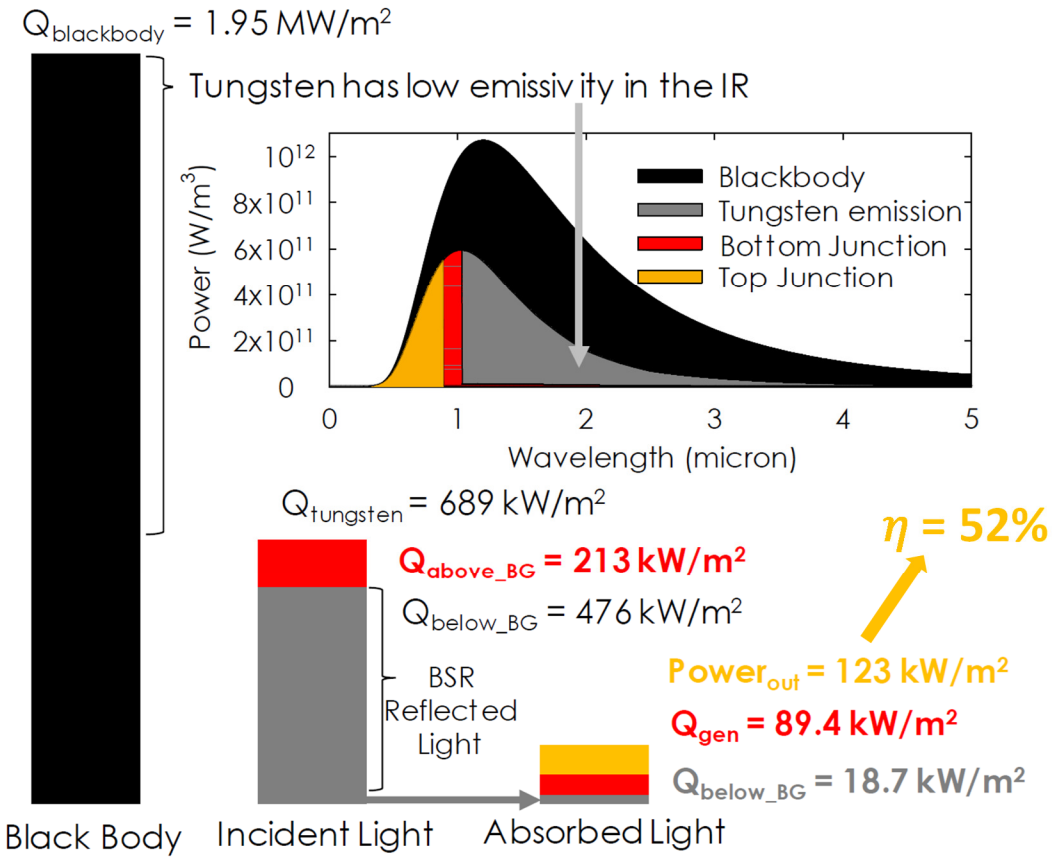

Figure 7 – Emitted, converted, and absorbed power components for a TPV system with two junctions with a 2150°C emitter. This case corresponds to the nominal operating condition of the TEGS system.

1.3.2.2. TPV Literature

There has been significant academic interest in thermophotovoltaics over the past decade, mainly focusing on improving cell efficiency at temperatures below 1500°C through the development of selectively emitting materials and nanostructures [12]–[14]. The previously demonstrated world record for TPV efficiency was set in 1981 with Swanson demonstrating 29% conversion efficiency with a silicon PV cell and a 2000°C heat source [15]. Figure 8 shows the progress in TPV efficiency since then, only exceeding Swanson's work in the past several years.

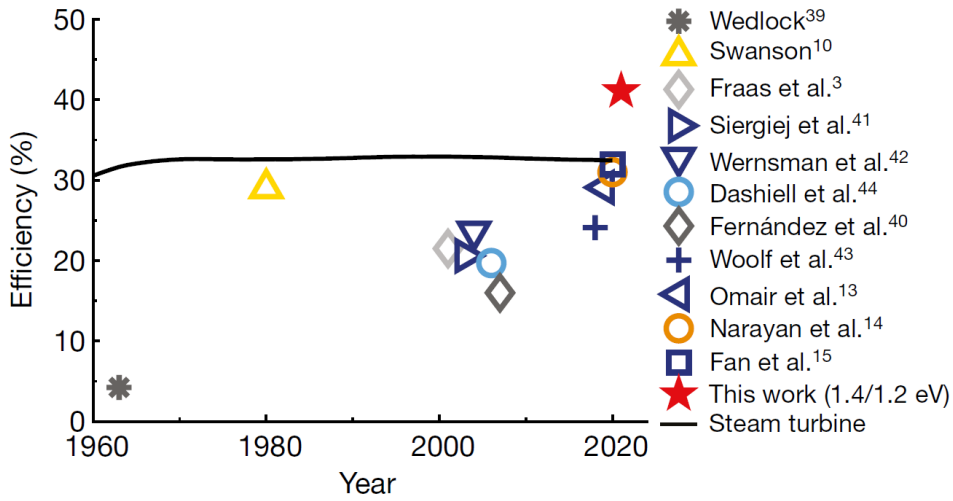

Figure 8 – TPV cell efficiency progress since 1960. Swanson's record for efficiency of 29% held until recent years, with LaPotin et al. demonstrating the record efficiency of 40% in 2022. Figure reproduced from LaPotin et al. [11].

Selective emitters enable high efficiency through the suppression of infrared emission. The TPV design shown in Figure 6 reflects these photons back to the emitter, recycling them, but another approach is to suppress the initial emission of the photons entirely. Figure 9 shows three such approaches, bulk material with an anti-reflective coating (ARC), a rare earth doped semiconductor with a back reflector, and a nano-structured photonic crystal. These approaches each have advantages in terms of selectivity over non-selective emitter materials, but typically cannot survive long term operation at temperatures above 1500°C [14]. In addition to the efficiency concerns of operating at lower temperatures, the technoeconomic analysis in the next section indicates how operating at temperatures above this limit is critical for an economical thermal energy converter for storage applications.

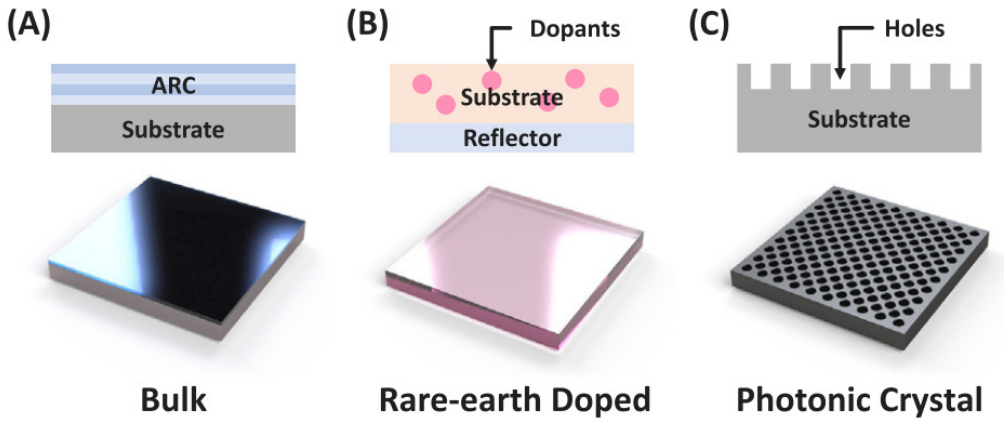

Figure 9 – Selective emitter options. (A) Bulk selective materials with a anti-reflective coating (ARC) are the simplest approach, with bulk materials like tungsten exhibiting weakly selective behavior. (B) Doped materials with a back reflector represents an alternative approach, acting like a optical filter coupled with a reflecting material. (C) The most complex selective emitter uses nanometric cavities in a typically metallic substrate to suppress certain wavelengths of light. Figure reproduced from Wang et al. [16].

1.3.3. Enabling Technologies

The TEGS storage concept is enabled by a number of technological innovations over the past decade. These can be generally grouped into hot-side and cold-side technologies and include but are not limited to the molten tin containment and pumping infrastructure (hot-side) as well as new multi-junction fabrication and development techniques (cold-side).

1.3.3.1. Liquid Metal Heat Transfer Fluids

The high heat flux and operating temperature of TEGS require a heat transfer fluid with unique properties, primarily surrounding thermal performance and high temperature stability. Table 1 compares a number of fluids, including three liquid metals, next-generation concentrating solar power molten salt, supercritical CO_2, and air. Tin was chosen for the TEGS system for several reasons including the metrics presented in this table, but the advantage of liquid metals is clear from a thermal perspective.

Table 1 – Comparison of heat transfer fluids including gas, solar salt and liquid metals. All properties were taken at 1000°C and 1 bar, with the exception of CO_2 at 200 bar pressure representing a supercritical CO_2 cycle. [17]

Material	T_{melt} [°C]	T_{boil} [°C]	k [W/m-K]	c_p [kJ/kg-K]	ρ [kg/m³]	μ [mPa-s]	Thermal Effusivity [J/s$^{1/2}$m^{2}K]	Thermal Diffusivity [mm^2/s]	Prandtl Number	Cost ($/kg)
Aluminum (Al)	933	2470	114	1.2	2291	0.92	17.5	42.36	0.010	2
Silicon (Si)	1414	3217	62	1.0	2520	0.79	12.5	24.50	0.013	2
Tin (Sn)	232	2602	47	0.31	6452	0.98	9.7	23.14	0.007	16.7
Chloride solar salt (KCl-$MgCl_2$)	708	>900	0.55	1.2	1425	0.83	0.95	0.33	1.75	0.50
CO_2	-	-	0.08	1.3	92	0.045	0.097	0.68	0.73	-
Air	-	-	0.008	1.2	0.27	0.050	0.005	257	0.72	-

The first six properties show: melting temperature, boiling temperature, thermal conductivity, specific heat, density, and dynamic viscosity, respectively. From these, several figures of merit can be derived including thermal effusivity, defined as $\sqrt{\rho c_{\mathrm{p}} k}$; thermal diffusivity, $\frac{k}{\rho c_{\mathrm{p}}}$; and Prandtl number ($Pr$), $\frac{c_{\mathrm{p}}\mu}{k}$. In general, a higher effusivity indicates an energy dense heat transfer fluid, minimizing flowrates and the volumes of HTF for a given power requirement. High thermal diffusivity, on the other hand, indicates the ease with which heat can be supplied or removed from the fluid, minimizing heat exchanger area and cost. Prandtl number compares viscous effects to heat transfer and can provide an indication of fluids that may be too viscous for a practical application.

Typically, the liquid metals provide the highest thermal effusivities and diffusivities. This indicates they are very effective heat transfer fluids, but they are also hampered by high costs. Salts are much cheaper, but have roughly an order of magnitude lower thermal effusivity and two orders lower diffusivity, indicating a larger required flowrate of HTF as well as a larger heat exchanger. In some situations, the cost savings in HTF can be negated with the additional pumping and heat exchanger investment.

To further illustrate the advantages of metals as HTFs, Figure 10 compares the ratio of required pump power to heat transfer rate (W/W) as a function of heat flux for three example fluids, holding pipe sizes constant. In applications that require high heat transfer rates (i.e. CSP or thermophotovoltaic power generation), metals require significantly lower pumping power for the same thermal performance.

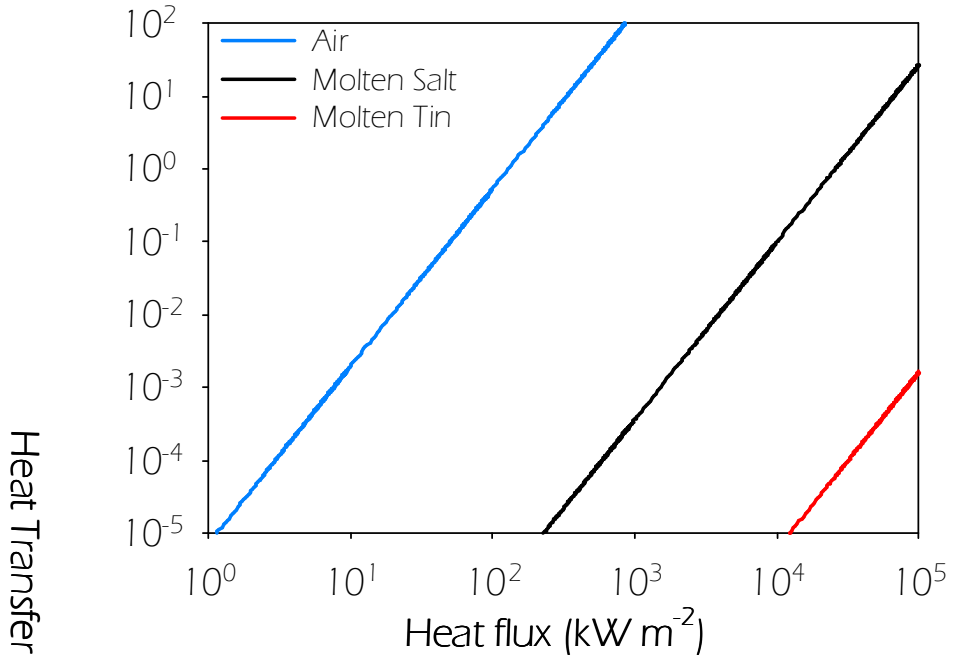

Figure 10 – Ratio of pumping power to heat transfer rate as a function of heat exchanger surface heat flux for three representative materials (air, solar salts, and tin).

1.3.3.2. Liquid Metal Containment and Pumping

There are several containment and pumping technologies that readily allow for liquid metal heat transfer fluids to be used in ultra-high temperature thermal systems. Figure 11 shows several of these components including tungsten and graphite compression fittings, tungsten and AlN-BN ceramic gear pumps, and a schematic of a pumping apparatus used to demonstrate the world record pumping temperature [18][19].

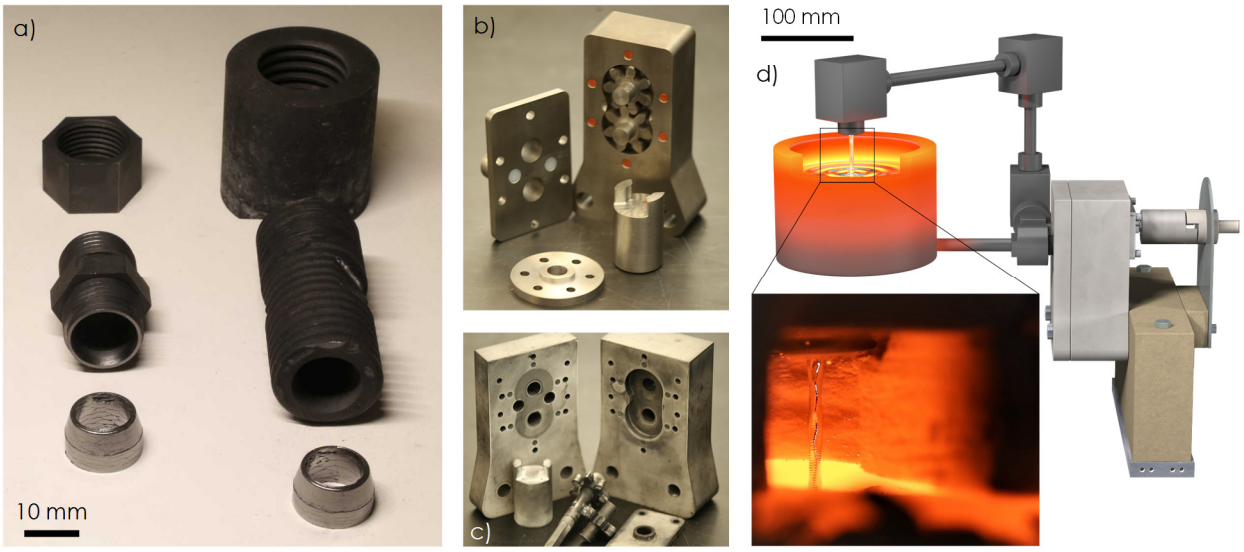

Figure 11 – Molten Tin Pumping and Plumbing. a) Tungsten (left) and graphite (right) compression fittings use for connecting graphite fluid transfer pipes. b) Tungsten gear pump c) Ceramic (AlN-BN) gear pump used for 1600℃ operation. d) Schematic of experimental demonstration of tin pumping at 1400℃ [18]

1.3.3.3. Multi-Junction Thermophotovoltaic Cells

Improvements in multi-junction cell fabrication techniques for thermophotovoltaics is another essential enabling technology for TEGS. Figure 12 shows the multi-layer stack used in a recent world-record TPV efficiency demonstration [11]. Details on the specific fabrication techniques and cell design, however, is outside the scope of this thesis.

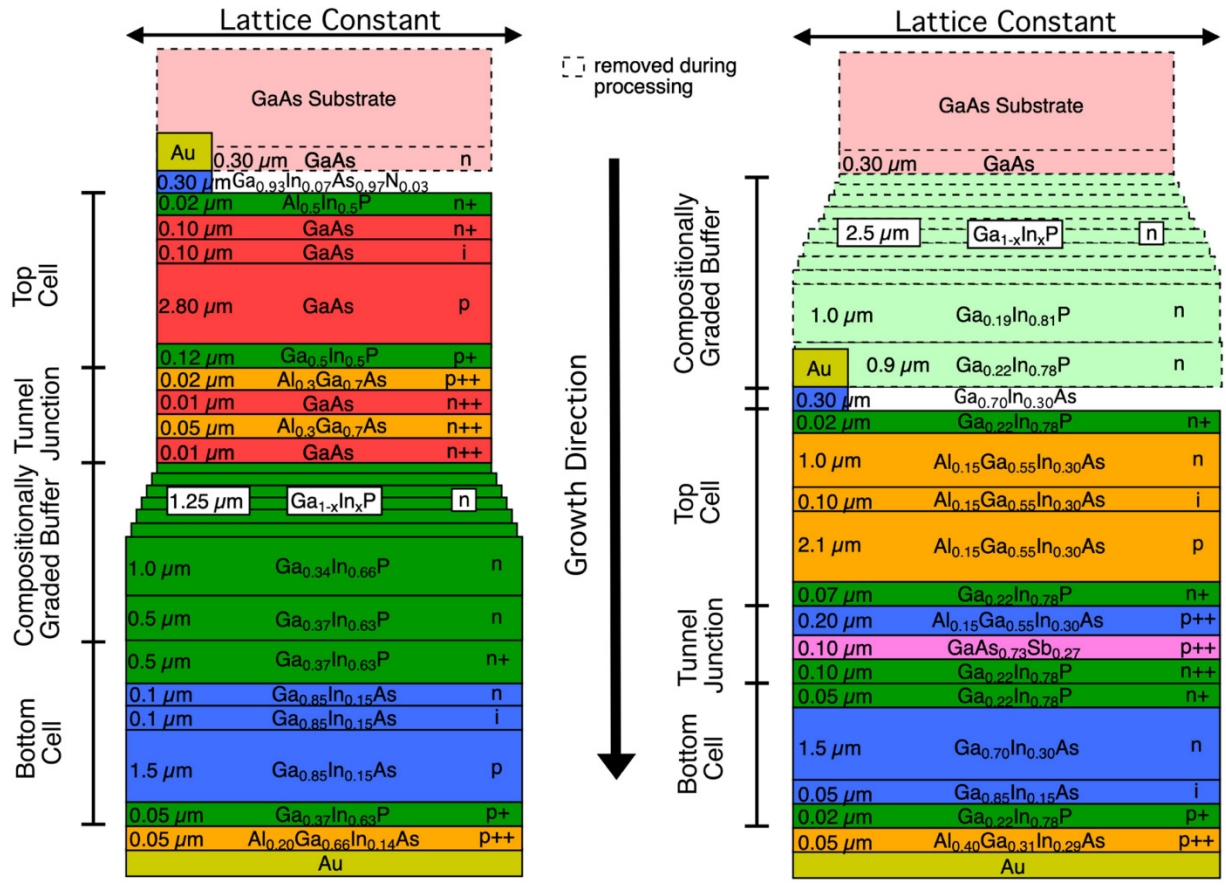

Figure 12 – Multi-Junction TPV Cell Configurations. Figure reproduced from LaPotin et al. [11]

1.3.4. Technoeconomics

To evaluate the potential of the TEGS design for deployment at scale, a technoeconomic model was developed for a nominal design. This model incorporates simple heat transfer and fluid flow calculations to estimate piping sizes, insulation thicknesses, graphite and tin volumes, and required TPV cell area. The full system has not yet been fully designed, but this model provides a good baseline for how the costs of the system scale with operating temperature and size.

To properly capture the range of useful implementations of energy storage, the predicted costs have been split into CPP in the units of dollars per watt-electric of the power block, and CPE in the units of dollars per kWh-electric of storage capacity. Four potential systems are considered as well: a 100MW-10 hour (1 GWh-e) system, a 100 MW-4 hour (400 MWh-e) system, a 10 MW-10 hour (100 MWh-e) system, and a 10 MW-4 hour (40 MWh-e) system. This technoeconomic model replicates the same

methodology and references for pricing as Amy *et al.*[9], with added cost components for the heat transfer fluid and increased quantities of graphite. Tin was chosen as the heat transfer fluid based on previous work showing that it can be pumped and contained within an all graphite infrastructure.[18] The cost of tin was taken as $17/kg based on a review of bulk tin prices. The material prices used for this analysis are shown in Table 1. This analysis does not consider site-specific development and balance-of-plant costs.

Table 2 – Bulk TEGS material prices including graphite storage medium, tungsten foil, and insulation

Material	**Density (kg/m^3)**	**Cost ($/kg)[9], [20]**
Extruded Graphite	1700	0.5
Graphite Insulation	24	540
Aluminum Silicate Insulation	100	4.0
Fiberglass Insulation	12	7.1
Tungsten Foil	19000	350

In general, the cost effectiveness/profitability of an energy storage system is determined by three main quantities: (1) the initial one-time total capital expenditure to create and install the system (CAPEX), (2) the recurring costs associated with operating the system (OPEX), and (3) its lifetime i.e., the number of charge/discharge cycles it can endure, before requiring replacement. Based on prior analysis, the predicted OPEX for the proposed system shown in Figure 4 is very low and the lifetime is anticipated to be > 30 years, since there is no known physical degradation mechanism within the system that would require replacement of components on a time scale less than 100 yrs. Therefore, the focus in this analysis is on the main cost component that would determine its cost effectiveness relative to other competing options, which is its CAPEX. The CAPEX here, denoted by K ($/kWh) is given by a combination of the CPE ($/kWh), CPP ($/kW), discharge duration t (hours) as follows: K = (CPE + CPP/t). With these inputs, one can estimate the total CAPEX for a given system configuration, and the major changes that occur in this work, as compared to the prior work of Amy et al., are associated with CPE, since the rest of the system is essentially unchanged.

In Figure 13, the calculated CPE is shown, which represents the cost of one kWh-e of storage capacity, independently of all the components that scale with the charge/discharge rate of the system. These results show how changing the size and storage duration affects the system cost. Here, it becomes clear that the graphite insulation, used to retain the heat is the predominant cost that changes with size. This is due to the change in surface area to volume ratio, and heavily favors larger system sizes, where the

fixed insulation thickness (i.e., skin thickness) comprises a smaller fraction of the total volume. It is also important to note here that the heat loss rate can be adjusted to affect this cost significantly. For the results in Figure 13, the heat loss rate was limited to 1% of the energy stored being lost each day. If, for example, one was building a smaller system that was expected to discharge every day, one might be able to tolerate a higher heat loss rate or > 2%, which could significantly reduce the costs associated with smaller systems. Furthermore, when systems are made very large, one could potentially afford to reduce the heat losses below 1%. Nonetheless, the results in Figure 13 show that once the proposed system reaches sizes on the order of 100 MW, the CPE can be less than the targets outlined in previous studies, namely < $20/kWh, which are needed to reach full decarbonization of the grid.

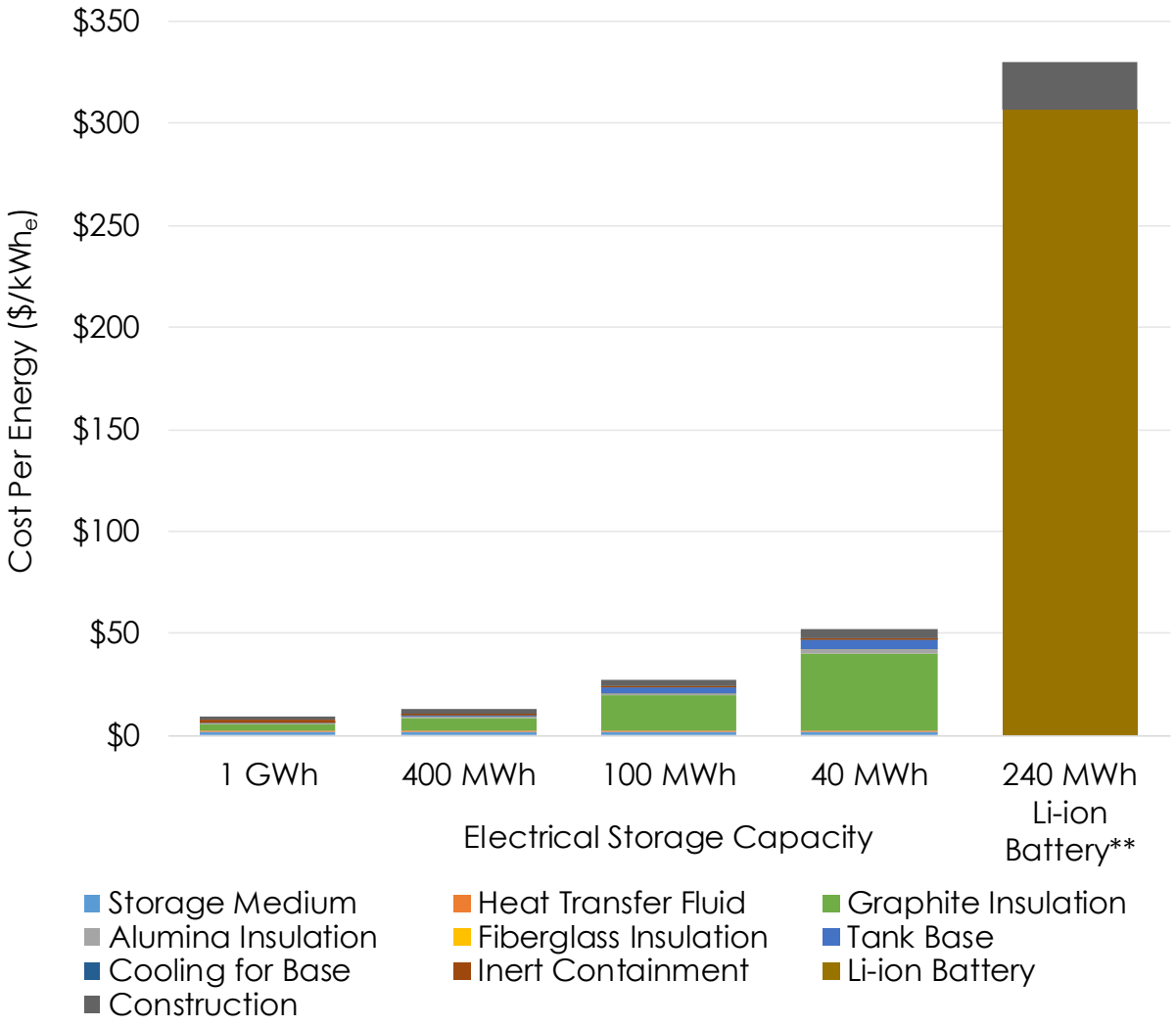

Figure 13 – Cost per Energy at multiple scales for the energy storage component of TEGS

Cost per Power (CPP) is more or less independent of scale in this model, but is a strong function of operating temperature. Figure 14 shows how the CPP compares between four systems operating with a 500°C temperature sweep, and varying maximum temperatures. For example, the 2400°C case operates between 1900°C and 2400°C during a full discharge/charge cycles, while the 1900°C case operates between 1400°C and 1900°C. Also included in the plot is the CPP of a gas peaker plant, the current state-of-the-art for ensuring reliable grid operation. From this analysis, the advantage of operating a higher temperature is clear. This is primarily a function of the higher optical and thereby electrical power densities achievable with a higher temperature TPV emitter.

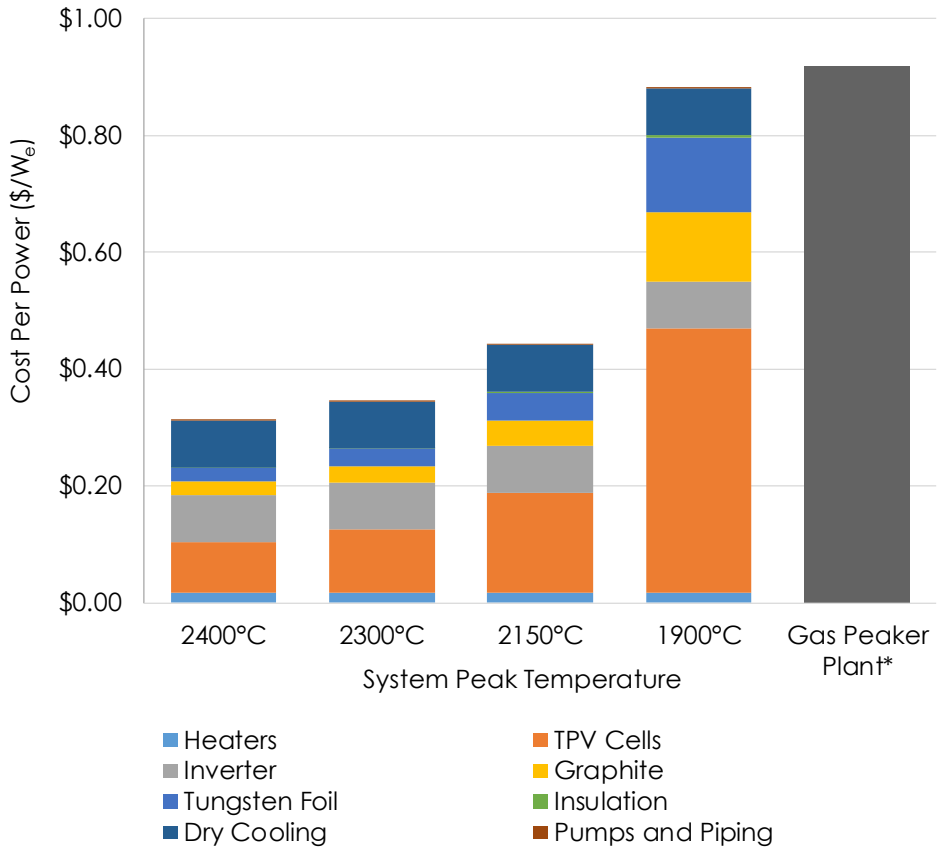

Figure 14 – CPP for the power block at multiple scales. Due to the decoupled power and energy components of the TEGS system, this cost does not scale with size of the storage system and changes minimally with varying power scales.

Figure 15 shows how the total CAPEX, K, is affected by the changes with system size for CPE and the size independent CPP. These results indicate that the proposed system is one of the lowest cost options reported in the literature, and therefore increased attention and development is warranted. Based on this analysis, the CPE for this embodiment can be < $20/kWh-e, while the CPP can be < $0.40/W-e, which is considerably lower than the cost of alternative heat engine technologies such as a turbine. With these cost estimates, the system costs can reach ~$40/kWh-e as system sizes > 1 GWh are employed, which is lower than any other technology option.

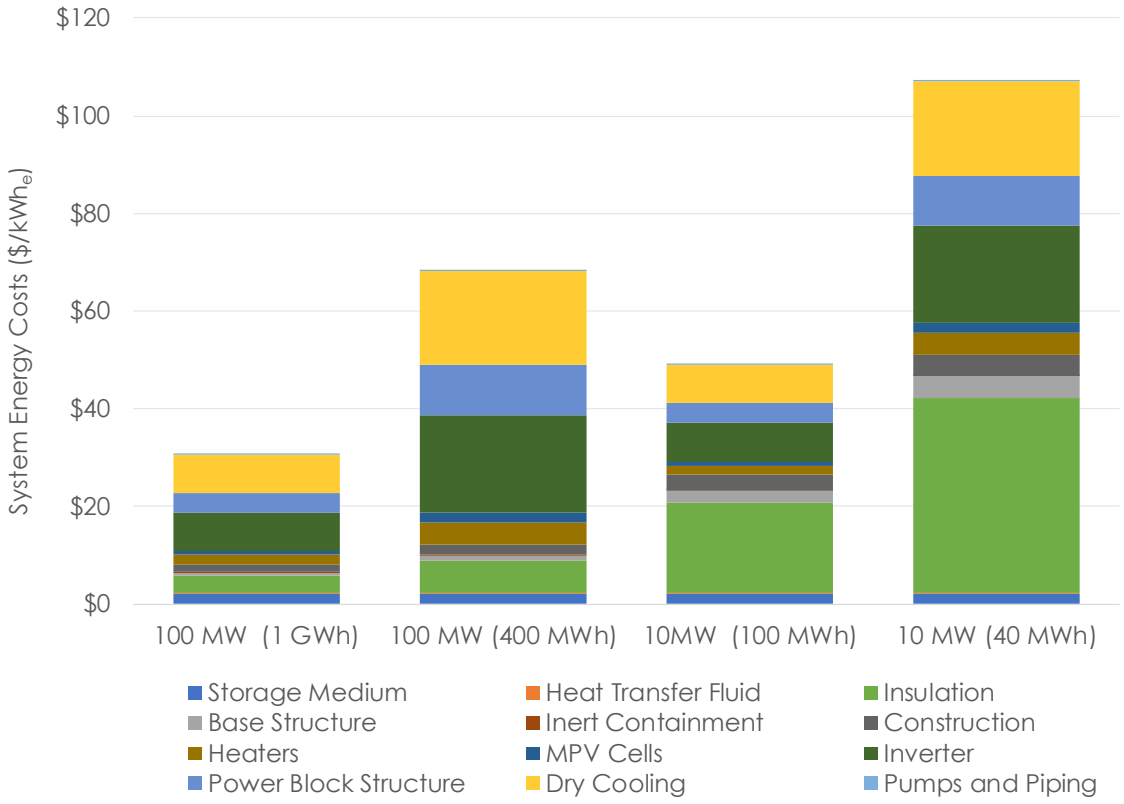

Figure 15 – Total cost of energy incorporating the Cost per Energy and Cost per Power into a system energy cost for the four proposed cases.

1.4. RESEARCH QUESTIONS AND OUTLINE

The primary objective of this thesis is to propose, design, and evaluate a durability enhancement device for a thermophotovoltaic heat engine used in an ultra-high-temperature, grid-scale, energy storage system. A secondary objective is to highlight the numerous challenges of designing and operating devices at temperatures above 2000°C. The remaining chapters will discuss these topics as follows:

Chapter 1 discusses the changing energy landscape and how grid-scale energy storage is necessary to ensure a reliable grid heavy with intermittent renewable energy resources. Additionally, a new storage technology, Thermal Energy Grid Storage, is proposed and some of its key technological components are explained. A technoeconomic model shows that it has the potential to provide a low cost and geographically unconstrained alternative to current storage technologies.

Chapter 2 summarizes some of the challenges experienced developing ultra-high-temperature experiments. Solutions to several of these issues are also shown, which are in used to inform the design of a TPV emitter capable of operating at temperatures above 2000°C.

Chapter 3 presents several models predicting the behavior of a Sweeping Noble Gas Curtain (SNGC) approach to preventing TPV cell degradation, a problem common in high-temperature TPV systems. These models were validated using a low-temperature proxy experiment, and the experimental findings were used to inform the design of a high-temperature experimental device.

Chapter 4 highlights a number of design components of an SNGC integrated cold plate capable of keeping cells cool and clean in a >2000°C thermal emitter cavity. The challenges associated with the manufacturing of this integrated SNGC-TPV device are also discussed in detail.

Chapter 5 explains the experimental apparatus used for testing of the designed SNGC-TPV device and shows results from a number of tests. These tests showed the effectiveness of the device at preventing deposition in the region protected by the SNGC and suggests it could be a vital and useful part of a larger-scale system.

Chapter 6 summarizes this work, proposes future studies that could help further evaluate the potential of TPVs at scale, and emphasizes the importance of the findings presented here on the energy community at large.

Chapter 2

2. TPV Emitter High Temperature Design Components

2.1. INTRODUCTION

One significant challenge to widespread deployment of TPVs is the extreme temperatures that they need to operate efficiently. Special care has to be taken in materials selection and thermal design to ensure these systems are able to hold temperatures in excess of 2000°C without degradation over time. This section summarizes some of the experimental challenges encountered and resolved when building apparatus in this regime. Additionally, and explanation is provided for the design constraints of a TPV emitter at these temperatures and how they are accounted for in a prototype, scalable emitter design.

2.2. ULTRA-HIGH-TEMPERATURE EXPERIMENTAL SYSTEMS

A significant amount of time was spent identifying and solving the problems that arise in ultra-high-temperature experiments. These problems included but were by no means limited to premature thermal degradation, electrical arcing, and chemical contamination. This section provides a selected set of the problems experienced, and will help inform future ultra-high-temperature experimental designs.

2.2.1. Materials Limitations

Many reactions follow an Arrhenius rate law, or something similar, whereby the kinetics of reaction increase exponentially with temperature. As a result, the kinetics of many thermal degradation reactions (e.g. oxidation) increase exponentially with temperature, so special care has to be taken to ensure compatibility between the materials used in ultra-high-temperature experiments.

When considering high-temperature stability, there are a limited number of materials capable of operating at 1500°C or hotter for extended periods of time. Options are mainly limited to refractory ceramics (i.e. alumina, zirconia, etc.), refractory metals (i.e. tungsten, tantalum, etc.), and various forms of carbon (i.e. diamond, graphite). An advantage of the refractory ceramics, particularly oxides like alumina, is that they are able to achieve the high operating temperatures in an oxidizing environment, something the metals and carbon compounds cannot.

A more restrictive constraint is to have both high-temperature stability, as well as high thermal conductivity. In this category, ceramics are particularly bad. Sintered alumina materials typically have thermal conductivities in the range of 8-34 W/m-K [21] compared to tungsten at around 175 W/m-K [22] and graphite at around 100 W/m-K [23].

Figure 16 shows a number of thermally damaged components from various experimental runs. These include oxidized tungsten leads from slight oxygen leaks in the apparatus, evaporated carbon heating elements, and overheated ceramic electrical and thermal insulators. This damage occurred primarily between 1400°C and 2000°C, illustrating the challenges this environment places on materials.

Figure 16 – Thermally damaged materials from overheating (bottom, right), oxidation (top left), and evaporation (top middle)

The low thermal conductivities of certain ceramics previously mentioned, can be advantageous in certain situations. There are a number of "high-temperature" insulation materials made from silica and alumina fibers. While oxide materials such as these have certain stability advantages in oxidizing environments (e.g. air), the reverse is true in inert or reducing environments. Figure 17 shows an Ellingham diagram that compares the relative stability of oxides at different temperatures. Higher on the chart represents more stable, and carbon oxides (CO and CO_2) are more stable than either alumina or silica over a wide range of temperatures. In an experimental environment with a graphite (C) heating element, the oxygen in these oxide materials will be stripped away by carbon, causing breakdown at temperatures far below their rated operating conditions in air. Figure 18 shows some of this degradation in hot regions where carbon and oxide-based materials coexist.

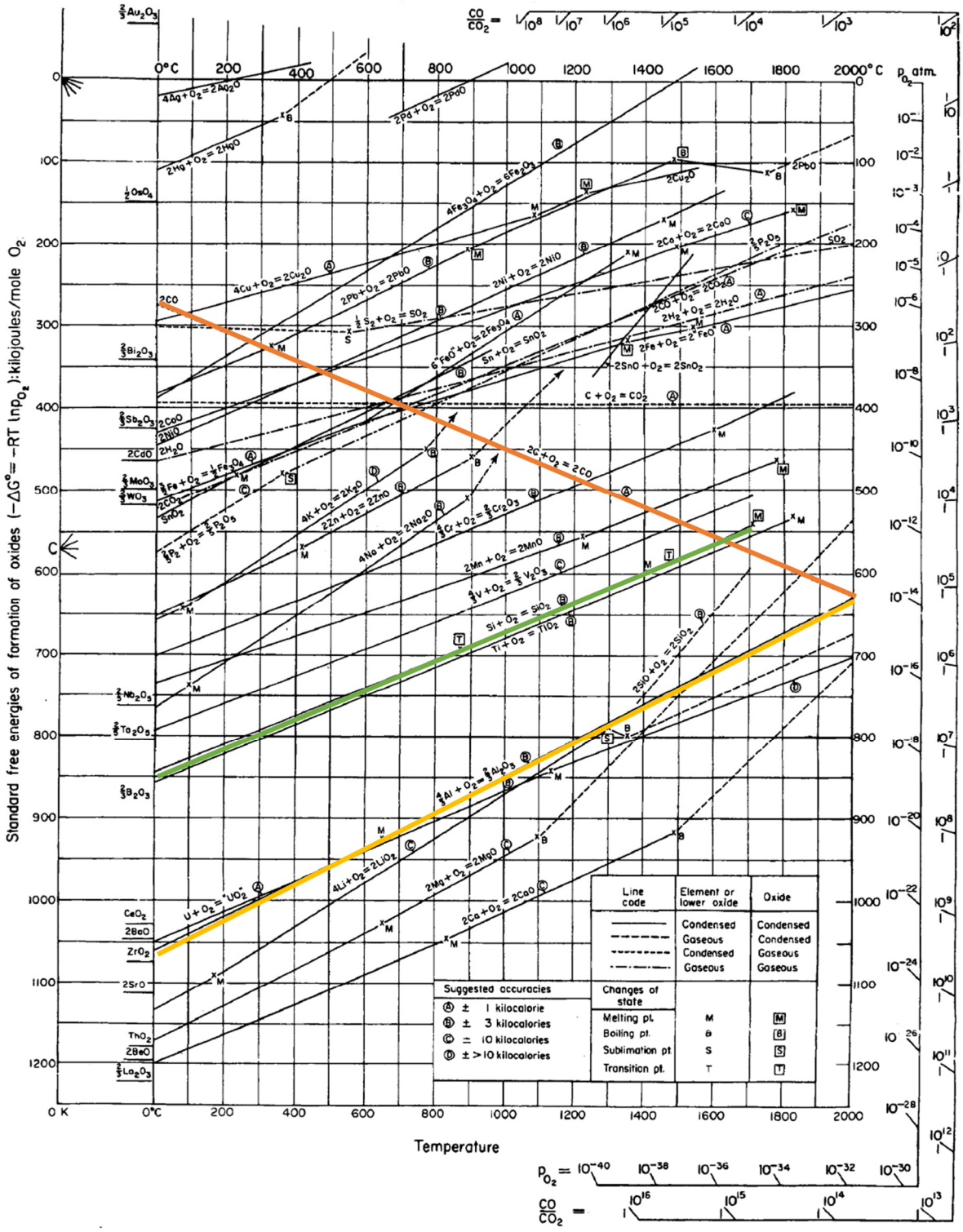

Figure 17 – Ellingham diagram showing relative oxide stability for numerous common oxides. Orange line represents the CO/CO_2 reaction, green represents silica (SiO_2), and yellow represents alumina (Al_2O_3). The higher up on the chart the line is, the more stable the oxide. Alumina and silica will therefore be reduced by carbon across a wide temperature range, causing the premature decomposition of oxides such as these [24].

Figure 18 – Degraded oxide materials from high-temperature experimentation. In environments with very low oxygen content, oxides more readily reduce and often fall short of their rated operating temperatures. Contact between graphite and alumina tube (left) has eaten away both materials due to this accelerated decomposition. Alumina silicate boards (middle, right) show breakdown of structure and chemistry due to the reduced operating temperatures in the presence of carbon.

Based on prior experiences with oxide-based insulation materials and their potential volatility even below rated temperatures, the system was changed to a pure graphite insulation approach. This came with its own set of challenges, as the graphite insulation has nearly an order of magnitude higher thermal conductivity. Table 3 summarizes the different insulation material options, and shows some of the cost disadvantages of this graphite pathway.

Table 3 – Summary of high-temperature insulation materials and relevant parameters including thousands of dollars per cubic meter, ($/m^3) [20]

Material	**Density (kg/m^3)**	**Thermal Cond. – *k* (W/m-K)**	**Max Temp. (°C)**	**Cost ($/m^3)**
Graphite Insulation	24	0.6-1	-	12900
Alumina Refractory Cement (WAM AL II)	1710	1.5	1700	6000
Alumina Silicate Insulation	100	0.1	1350	400
Fiberglass Insulation	12	0.05	540	80

2.2.2. Arcing

Another unforeseen issue experienced during high temperature testing was arcing at relatively low voltages (<30V). The graphite heating elements used to maintain operating temperatures of >2000°C would arc between terminals and the graphite insulation, damaging connections and shorting the heating path. This resulted in a significant reduction in input power, and corresponding drop in operating temperatures. Figure 19 shows how the arcing breakdown voltage, where an arc starts spontaneously, for two inert gasses. The high temperature experiments were typically done in argon, due to its low cost and low thermal conductivity, which shows arcing potential in the 30-40V range for the operating temperature range.

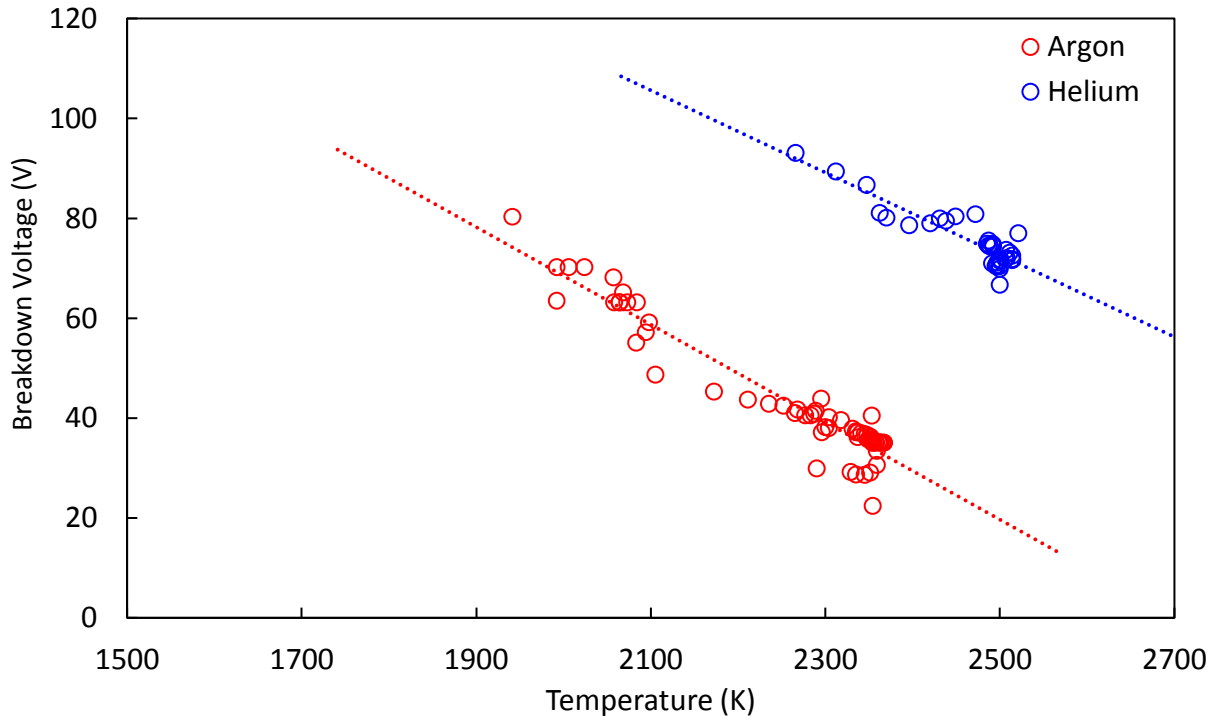

Figure 19 – Arcing breakdown voltage at various temperatures for two gas environments. Figure reproduced from Amy [20] *and corresponds to a gap size of 15mm and a gas pressure of 1 bar.*

Figure 20 shows the damage caused by arcing both to graphite heaters and the tungsten leads used to power them. The melting temperature of tungsten is 3422°C, which the arc reached during operation, causing a number of melted electrical leads.

Figure 20 – Arc-melted tungsten leads and damaged graphite heater due to arcing during high-temperature operation.

To reduce the arcing potential, the heaters were redesigned to operate at a lower voltage (~20V) and higher current (~500A) than before. This introduced its own set of complications involving much higher gauge electrical wiring and increased resistive losses, but resolved the catastrophic damage caused by the arcing.

2.2.3. Oxygen Partial Pressure and Gettering

At temperatures above 2000°C, few things are as problematic as oxygen. The very high temperatures accelerate oxidation reactions and many of the materials, namely graphite and tungsten, would be consumed quickly in an oxygen rich environment. More importantly, the highest temperature components would be consumed or oxidized first. This is particularly problematic for a system where the main heater is graphite, with tungsten electrical leads. Figure 16 shows some of the damage that can occur under these conditions, therefore great care was taken to remove as much oxygen as possible from the gas environment. The most obvious solution, and the tried first, was just vacuuming, backfilling, and purging the chamber with an inert gas with low oxygen content, namely ultra-high-purity (UHP) argon. Unfortunately, even in UHP argon, there is still ~1 ppm (part-per-million volumetric) oxygen. When heating, the oxygen content in the gas typically dropped to below 10^{-10} ppmO_2. A number of options were

considered for dropping the oxygen content before the primary heat up, to reduce the aforementioned oxidation damage in the heaters. The first approach, shown in Figure 21, used a zirconium metal powder heated to over 300°C to preferentially react with the oxygen in the gas environment. This method worked, but took a very long time to reduce the oxygen content. Also, the produced zirconia (ZrO2) formed a protective scale (seen as white in the figure), that shielded the underlying zirconium from reacting. This approach was deemed insufficient to reduce oxygen content in a timely manner.

Figure 21 – Zirconium metal oxygen getter. Powdered metal heated in a zirconia crucible to >300℃ to accelerate oxidation kinetics. Partially consumed getter material appears different colors as it oxidizes.

The updated and more successful approach was to use a sacrificial graphite heater to consume any oxygen in the gas. Graphite has the advantage of forming a gas (CO or CO_2) as an oxide, which prevented any protective oxide scales from forming. Figure 22 shows two iterations of this approach, both using a graphite heater for both a heat source and a source of reactive material. The downside of this approach is that the heater is slowly consumed over several cycles and must be frequently replaced. Besides that, this approach worked very well, and was able to lower the oxygen content to 10^{-13} ppmO2 relatively quickly, shown in Figure 23.

Figure 22 – Sacrificial graphite heater oxygen getters. Heated to >500℃ to accelerate oxidation kinetics. Graphite insulation blocks in left figure increase available surface area for oxidation reaction.

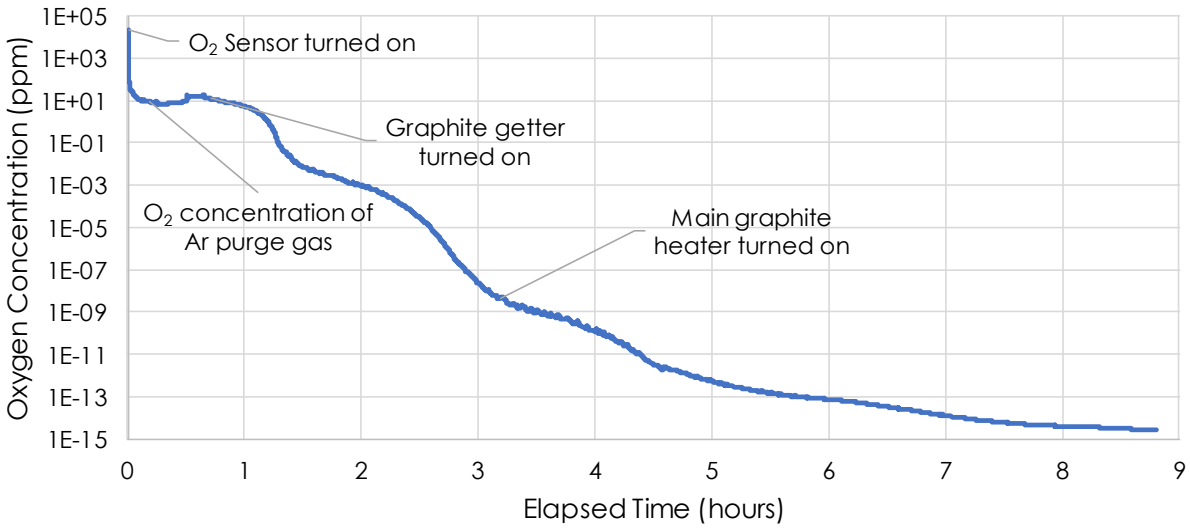

Figure 23 – Oxygen content in chamber environment drops significantly after heating graphite getter

2.2.4. Water Desorption

Another challenge with oxygen removal, was water in the experimental chamber. Water is problematic for a number of reasons, primarily its oxygen content. Even after vacuuming the gas from the experimental chamber, water worked its way out of the graphite insulation material and contaminated the experiment. The theory was that water was adsorbing in the insulation, forming a thin layer on all exposed surface area. This is normally not a problem, as the layer is merely a few atomic layers thick, but due to the fibrous and porous nature of the insulation, shown in Figure 24, the total internal surface area of the insulation blocks (~0.5 m^3) was enormous (~10,000 m^2).

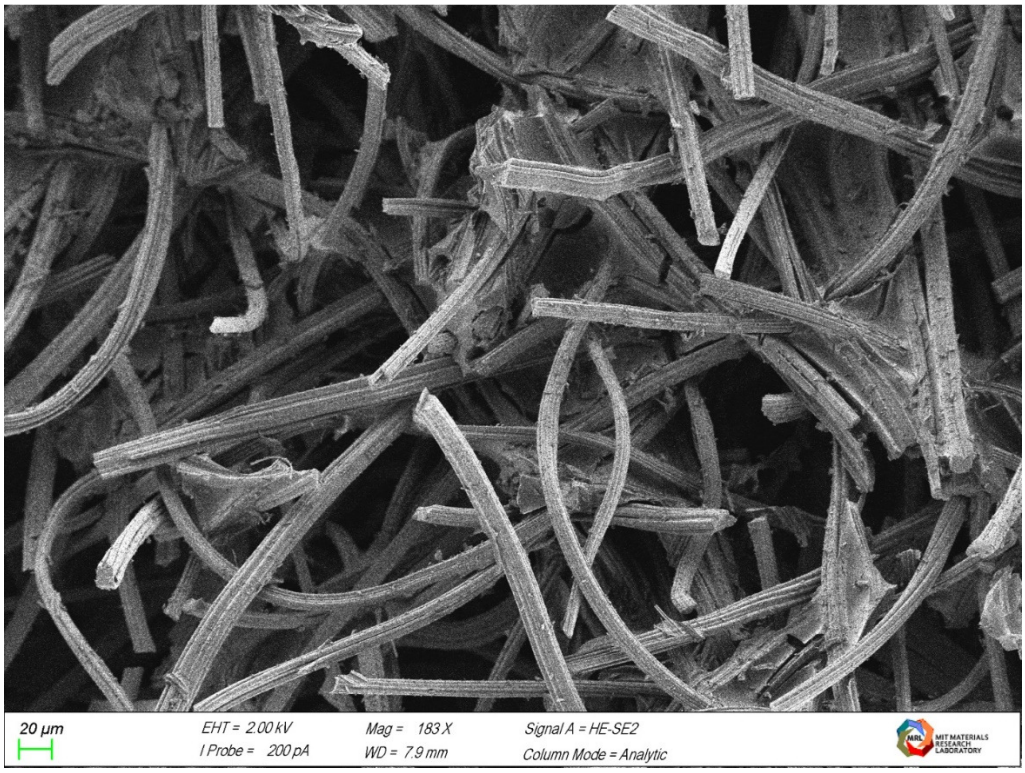

Figure 24 – Rigid graphite insulation fibers (Rayon-precursor fabrication technique). High surface area adsorbs significant water when resting in laboratory environment

Desorption of water from the surfaces does occur in vacuum, as evidenced from the oxygen contamination of the experiments, but occurs much more quickly at elevated temperatures. Heating the insulation to 200°C overnight while holding vacuum on the experimental chamber proved sufficient to eliminate much of the adsorbed water. Figure 25 shows a block of graphite insulation, encasing a

>2000°C experimental apparatus, wrapped in heating tapes to ensure uniform heating of the insulation during the bake-out process. Heating using the main graphite heater would result in a significant thermal gradient between the core and surfaces of the block, reducing the effectiveness of the bakeout.

Figure 25 – Heat tapes for baking out insulation block in vacuum to remove adsorbed water

Measuring the water content in the experimental gas environment is challenging, but hydrogen content can be used as a helpful analog. Some portion of the water in the gas decomposes into oxygen and hydrogen, allowing a gas chromatography measurement to indicate relative water content. Figure 26 shows two gas chromatography measurements taken during experiments, with and without baking out beforehand. The scales are different, but the relative concentration of hydrogen is significantly reduced in the case with a preparatory bakeout, suggesting the water content is as well. This approach proved helpful, and reduced the oxidation related damage shown in Figure 16 in subsequent experiments.

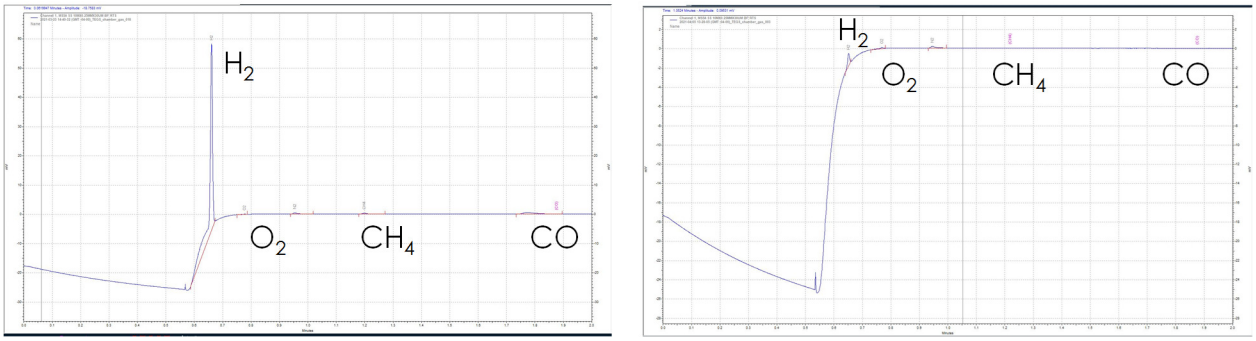

Figure 26 – Gas chromatography analysis of the chamber gas environment during experiments with (right) and without (left) an overnight bakeout to desorb water from the insulation. The size of the peak relative to the main curve represents relative concentration of species.

2.2.5. Insulation Contamination

One particularly problematic challenge was the issue of impurities and contaminants in the otherwise very helpful graphite insulation. After a number of high-temperature tests, a white deposition layer was visible on several components, shown in Figure 27. There were a few remaining oxide components in the experiment, primarily in the form of high-density alumina electrical insulators which were initially thought to be the culprits. The deposition remained, however, even with a purely graphite hot region.

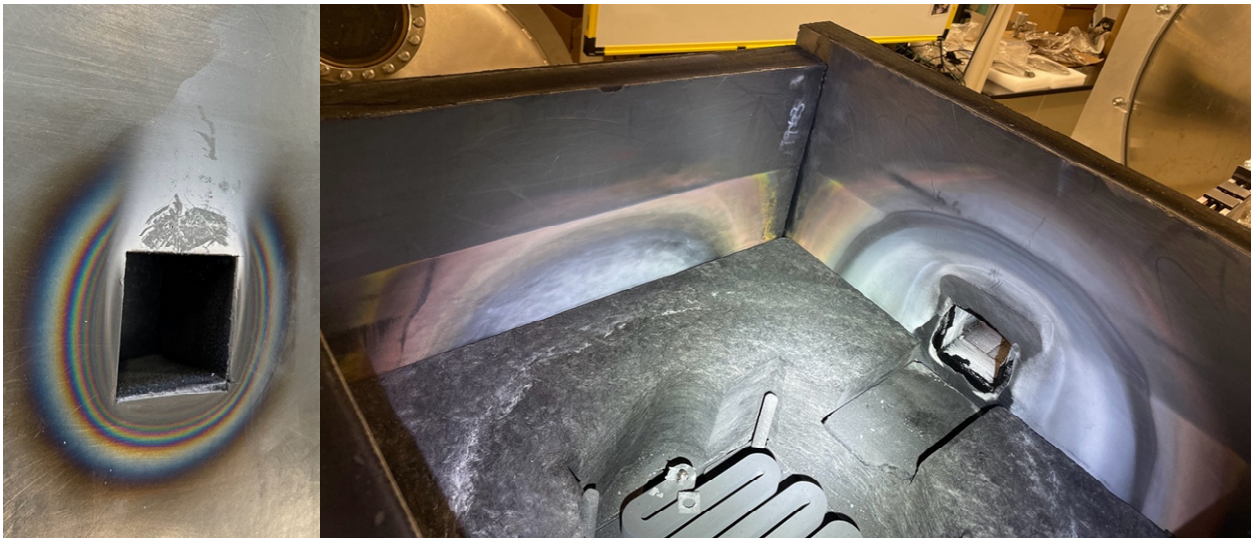

Figure 27 – Insulation contaminant deposition (white/pink material) on graphite insulation boards. All hot components should be pure carbon, apart from impurities. Left image is the opening in the insulation from the outside, rings are optical refractions from a varying thickness deposition layer.

Samples of the deposited material on a copper substrate, shown in Figure 28, were analyzed them using scanning-electron microscopy (SEM) to determine composition. Figure 29 shows the results of this analysis, suggesting a significant amount of oxygen, sodium, phosphorous, and copper. Further research showed that sodium, the dominant contaminant, is part of the manufacturing process for the graphite insulation. Discussion with the manufacturer determined that the presence of these contaminants was not unexpected, but purification could be done to remove them.

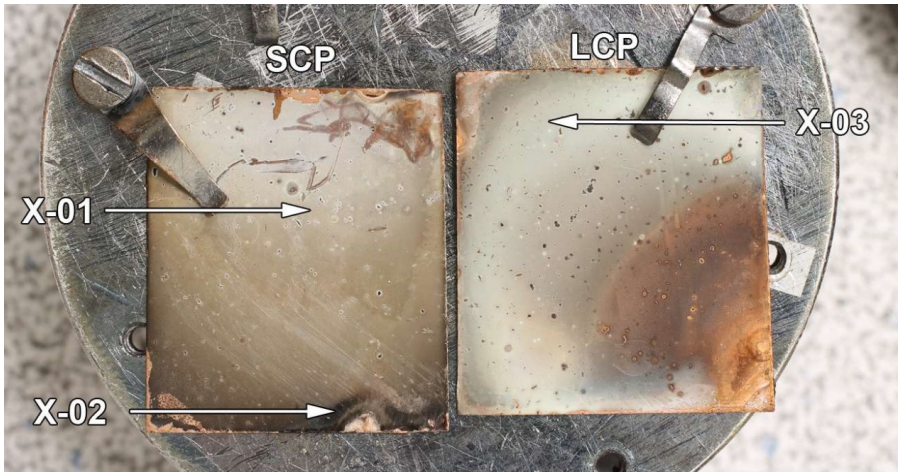

Figure 28 – Copper samples with insulation contaminants deposited. SEM measurements were taken at several locations to determine composition.

Element Line	Norm. Wt.%	Atom %
C K	4.4	8.8
N K	1.1	1.9
O K	28.6	42.8
Na K	21.0	21.8
Al K	1.1	0.9
Si K	2.8	2.4
P K	9.7	7.5
S K	0.9	0.7
Cl K	0.2	0.1
K K	1.9	1.1
Ca K	4.7	2.8
Cr K	0.2	0.1
Fe K	1.6	0.7
Ni K	0.5	0.2
Cu K	21.2	8.0
Total	100.0	100.0

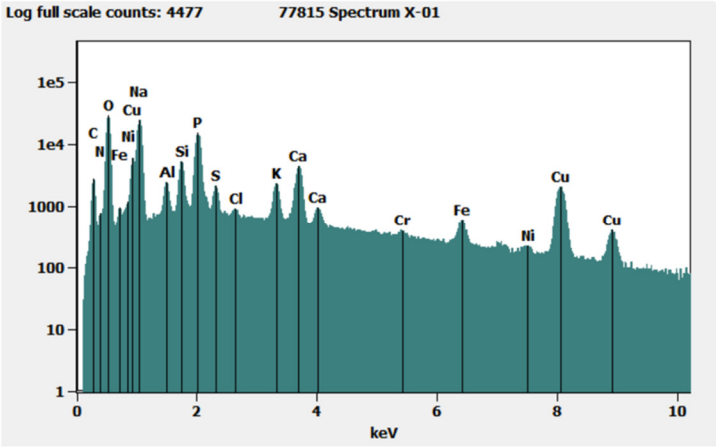

Figure 29 – Contamination composition. Plot and table of SEM analysis of white deposited material.

2.3. EMITTER DESIGN

A thermophotovoltaic emitter has several important design constraints, both at the lab and industrial scales. In this section, a selection of these constraints is summarized and incorporated into a prototype emitter design capable of achieving a 2400°C emitting surface for thermophotovoltaic system testing. Topics include materials selection, geometry, scalability, sealing against contaminants, and fabrication approaches.

2.3.1. Material Sublimation and Deposition

A major question addressed by this thesis is how to prevent deposition on the TPV cells, degrading their performance over time. The simplest approach is to select the material that sublimates the least at the maximum nominal operating temperature, 2400°C. The material set is limited at these temperatures, with tungsten and graphite representing some of the best options for emitters. Past work on thermophotovoltaics has typically used these materials for non-spectrally selective emitters [12], [15].

In the simplest case, rate of sublimation of a material is proportional to its vapor pressure, as this is the primary driving force for Fick's law of diffusion. Eq. (4) shows how molar flux, J (mol/m^2-s), is a function of concentration, C, gradient and a diffusion coefficient, D. Concentrations can be estimated at a surface as a function of temperature, T, and material vapor pressure, P_{vap}. Using this simple analysis, it is clear that a lower vapor pressure should result in lower material flux down the concentration gradient.

$$J = -D\frac{\Delta C}{\delta} \tag{4}$$

$$C = \frac{P_{\text{vap}}}{R \cdot T} \tag{5}$$

Figure 30 compares the vapor pressures of tungsten, graphite and silicon. Silicon is a common material for certain classes of selective emitters and is included as a comparison, but its low melting (1414°C) and boiling points (2355°C) eliminate it as an option for ultra-high-temperature TPV devices. Tungsten has the lowest vapor pressure of any element, roughly 4 order of magnitude lower than graphite. This suggests the sublimation and deposition rate of tungsten should be much lower than that of graphite.

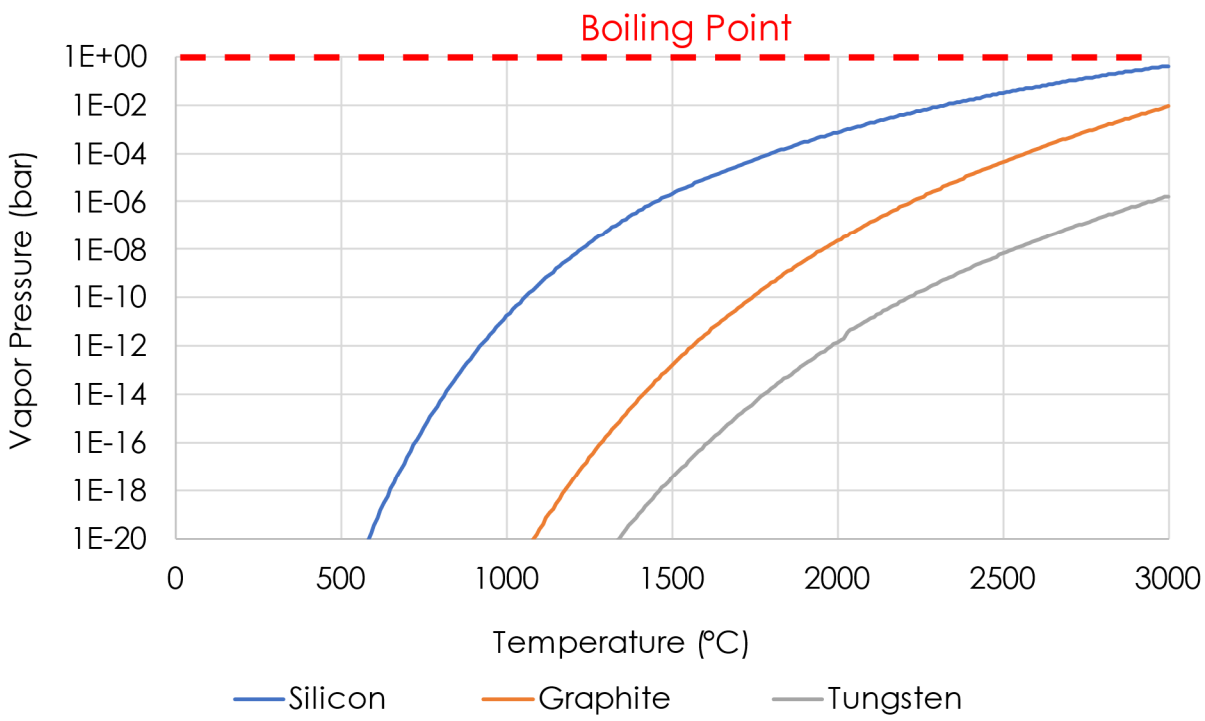

Figure 30 – Vapor pressure comparison for silicon, a common selective emitter material, graphite and tungsten. Tungsten has the lowest vapor pressure of any metal.

Graphite, or carbon, deposition was observed during several experiments, further suggesting that the emitter material sublimating could be a problem for cell durability. Figure 31 shows this deposited layer on a small microchannel heat sink.

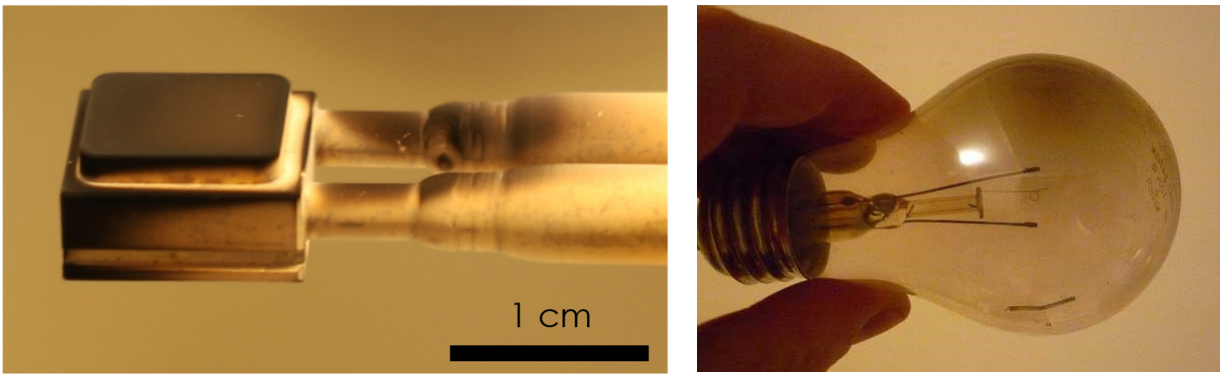

Figure 31 – Carbon deposition on a microchannel cold plate (left) and representative tungsten deposition on a blown light bulb (right).

To further evaluate the rate of sublimation and deposition that would be expected, a simple mass transfer diffusive model was developed. Figure 32 shows the schematic for the model, placing a hot emitter and cold PV cell distance, δ, away from each other. Using Eq. (5) to estimate concentration of the sublimating species at the emitter surface, and Eq. (4) to determine diffusive flux. The temperature dependent diffusion coefficient (D_{AB}) of emitter material ($_A$) in an argon ($_B$) inert gas environment can be determined using the following equation from Skelland [25] derived from Chapman-Enskog kinetic theory.

$$D_{AB} = \frac{0.00186T^{3/2}}{P(\sigma_{AB})^2\Omega_{\mathrm{D},AB}}\sqrt{\frac{1}{M_A}+\frac{1}{M_B}} \tag{6}$$

where T is temperature in K, P is absolute pressure in atm, M is molar mass in angstroms, and D_{AB} is in cm^2/s. The Lennard-Jones force constant σ_{AB} is tabulated in Skelland and the collision integral $\Omega_{\mathrm{D},AB}$ is of order 1 and was estimated based on an experimentally determined empirical relationship [26].

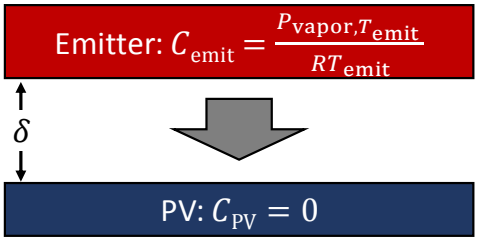

Figure 32 – Simple diffusion model schematic showing an emitter and PV cell separated by a gap of height δ.

Figure 33 (left) shows the results of this analysis for a gap distance of 10 cm between the cell and hot emitter. At the peak TEGS operating temperature of 2400°C, the deposition rate of tungsten on the cell surface should be around 3 nm/year, while graphite is many times that (~20 μm/year).

$$\alpha_\lambda = \frac{4\pi\kappa_\lambda}{\lambda} \tag{7}$$

$$A_\lambda = e^{-\alpha_\lambda \delta} \tag{8}$$

$$R_\lambda = \left|\frac{1 - n_\lambda - i\kappa_\lambda}{1 + n_\lambda + i\kappa_\lambda}\right|^2 \tag{9}$$

The reflection and absorption of a tungsten layer deposited on the cell surface can be estimated using the complex refractive index of tungsten [27], and a method described by Chen [28]. Eq. (7) was used to calculate the wavelength dependent (λ) absorption coefficient (α), which can be used to estimate wavelength dependent absorptance, A, when combined with layer thickness δ, using Eq. (8). Eq. (9) was used to calculate the reflectivity of the layer also using the wavelength dependent complex index of refraction (n and κ). Each of these values was calculated for each wavelength and integrated over the black body spectrum at the emitter temperature to determine total reflectance and absorptance. The results of this analysis are also shown in Figure 33 (right). Although 3 nm is thin, only 6 unit atomic layers, this model estimates roughly 10% absorption of incoming light from a 2400°C emitter. With even tungsten deposition posing a concern, using a material with a higher vapor pressure would be much worse, and tungsten is the clear choice of an emitter material for the TEGS temperature range (1900°C-2400°C).

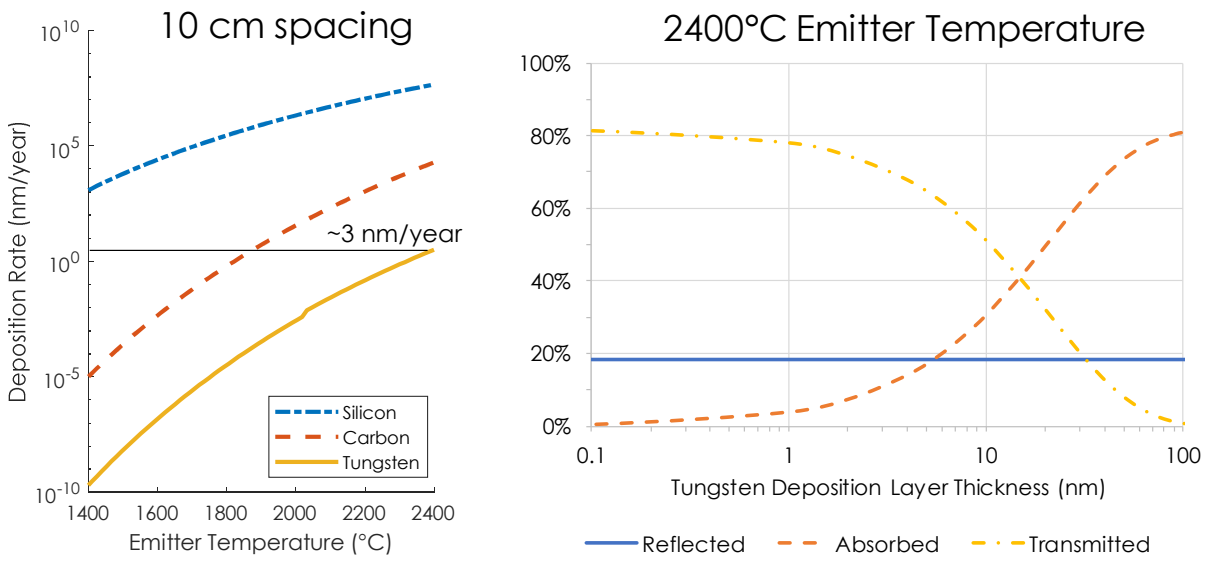

Figure 33 – Deposition rate comparison (left). Absorption, reflection and transmission of a thin tungsten film deposited on a cell (right).

2.3.2. Geometry

Tungsten's low vapor pressure makes it a good option for an emitter, but it comes at a cost in optical properties. Figure 34 shows how the emissivity of tungsten is relatively low across a wide wavelength range. This would result in a lower optical power density on the cell, resulting in lower power generation, and a less economical system, illustrated in the previous Technoeconomic section. Fortunately, the lower emissivity can be compensated for geometrically, allowing one to use a tungsten emitter without sacrificing optical or electrical power density.

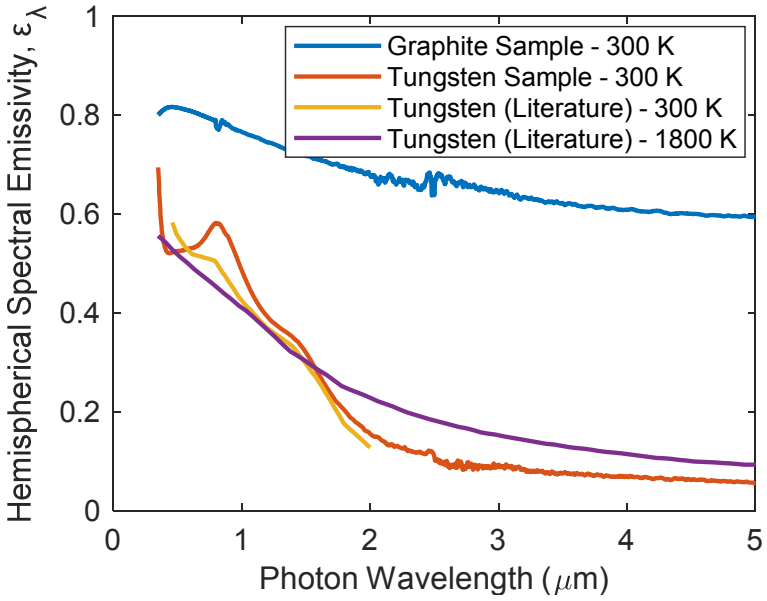

Figure 34 – Comparison of graphite and tungsten spectral hemispherical emissivity profiles at 300 K (measured) and 1800 K (literature) [29].

To increase optical intensity on the cell, three paths can be taken. Increase emitter temperature, increase the emittance of the emitter material to as close to 1 (black body) as possible, or increase the area of the emitter relative to the cell. Eq. (10), shows the relationship between emitted radiative power, q_{emit} (W/m^2); temperature, T (K); and emittance, ε. The optical power actually getting to the cell, however, can be quite a bit lower than that, shown in Eq. (11). In this equation, the incident power on the cell is a function of both emitted power, as well as a view factor, F, and ratio of areas, A. This "view factor" can be estimated for parallel flat plates using Eq. (12) where d is the distance between the cell and emitter. Eq. (13) incorporates all these components into an approximation for how incident optical power on the cell is influenced by emittance, emitter area, distance, and temperature.

$$q_{\text{emit}} = \varepsilon \sigma T^4 \tag{10}$$

$$q_{\text{cell}} = q_{\text{emit}} F_{\text{emit-cell}} \frac{A_{\text{emit}}}{A_{\text{cell}}} \tag{11}$$

$$F_{\text{emit}-\text{cell}} \approx \frac{A_{\text{cell}}}{\pi d^2} \quad \left(\underline{\text{when}}\ \frac{A_{\text{emit}}}{d^2} < 0.04\right) \tag{12}$$

$$q_{\text{cell}} \approx \frac{\varepsilon\sigma}{\pi}\frac{A_{\text{emit}}}{d^2}T^4 \tag{13}$$

Figure 35 visually shows how some of these variables might be manipulated geometrically to account for limitations in emittance while holding temperature constant. In Figure 35(a), having an emitter and cell so close together poses numerous practical challenges (namely unintended and destructive physical contact between the emitter and cell) so moving them apart is a logical next step. Eq. (13), however, shows how increased separation, Figure 35(b), will decrease intensity on the cell quite significantly, due to the reduced view factor. This can be accounted for with a larger emitter area, Figure 35(c), but the view factor drops if the emitter area becomes too much larger than the cell, since much of the emitted light escapes. Surrounding the cell with an emitter is the next logical step, Figure 35(d), but again poses challenges where the emitter and cell are very close together. Figure 35(e), an emitter cavity with cells covering an internal, cooled, structure provides the best design. It allows a large emitter area, adequate distance between hot and cold system components, and no loss of light to the environment – except from the ends. A square geometry is one of the simplest cases taking advantage of this cavity effect while still allowing the use of large flat TPV cells. For the rest of this thesis, the square cavity and cold plate are used as a nominal design case.

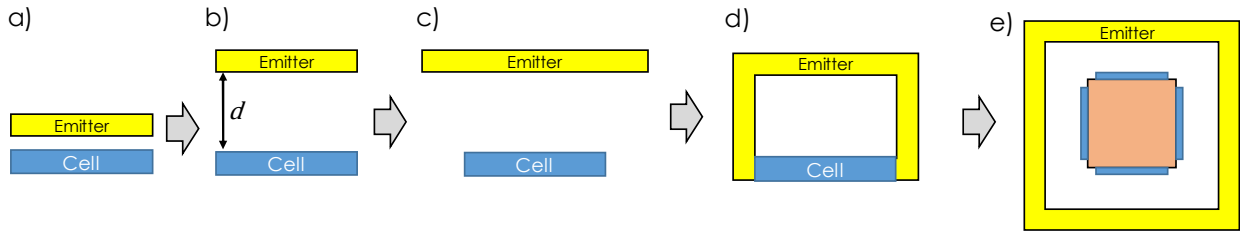

Figure 35 – Enclosed cavity maximizes optical intensity by eliminating edge effects. Square cavity is the simplest shape for flat TPV cells.

2.3.3. Scalability

With the reduced emissivity of tungsten compensated by an increased area ratio, tungsten remains a viable and advantageous option for emitter material, at least in concept. However, when actually building

such an emitter, the cost and machinability challenges of tungsten become important practical considerations. Tungsten is roughly 75 times the cost of graphite by volume (366,000 $/m^3 and 5,000 $/m^3 [30][31]). Also, its high hardness and brittleness make it very challenging to machine. Making an entire cavity from tungsten is cost prohibitive, even at the lab scale. However, a combination of graphite and tungsten could potentially overcome these issues.

Figure 36 shows a simple hybrid approach where a graphite cavity or scaffold is lined with thin tungsten foil to harness the low vapor pressure without the aforementioned challenges. Since tungsten becomes quite soft (like wet clay) at temperatures above 1500°C the first iteration of this design, a simple coil of foil, proved mechanically unstable.

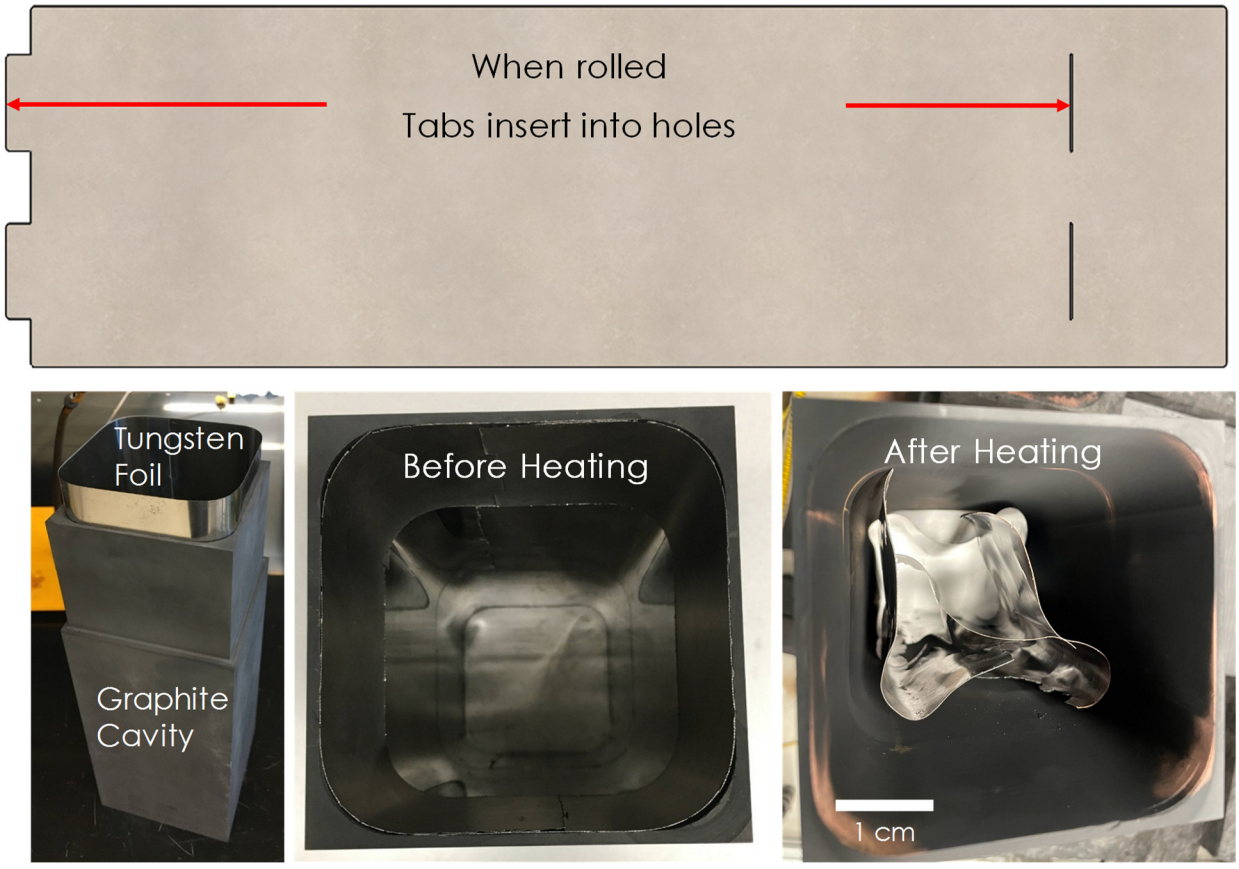

Figure 36 – Graphite scaffold or shell with a tungsten foil liner to reduce cost. Simple coil of foil proved mechanically unstable at high temperatures and collapsed on itself.

Mechanical stability concerns notwithstanding, another question is whether carbon will eventually diffuse through the tungsten lining, which would negate the low-vapor pressure advantage of tungsten. At these temperatures, the carbon vapor will react with the tungsten and form a tungsten carbide layer on the outside of the foil liner. This the diffusion coefficient of carbon in bulk tungsten carbide is significantly lower than that of carbon in bulk tungsten, so this layer acts like a protective scale [32]. Figure 37 shows a simple diffusion model of carbon in three materials and estimates how long it would take to diffuse through a 1 cm thick layer of tungsten using Eq. (14), a rearrangement of the diffusive penetration depth equation. The time, t, is related to the layer thickness, δ, and diffusion coefficient, D [32], [33].

$$t \approx \frac{\delta^2}{D} \tag{14}$$

It remains unclear whether grain boundary or bulk diffusion will dominate in the tungsten layer, but the results of this analysis suggest diffusion of carbon through the tungsten foil layer could be mitigated with a sufficiently thick layer. Literature suggests that grain boundary diffusion dominates at diffusion depths larger than 1 μm [32], which would cause full carburization of the tungsten layer relatively quickly. If this is indeed the case, an additional diffusion barrier like silicon-carbide may be necessary to prevent cell carbon contamination.

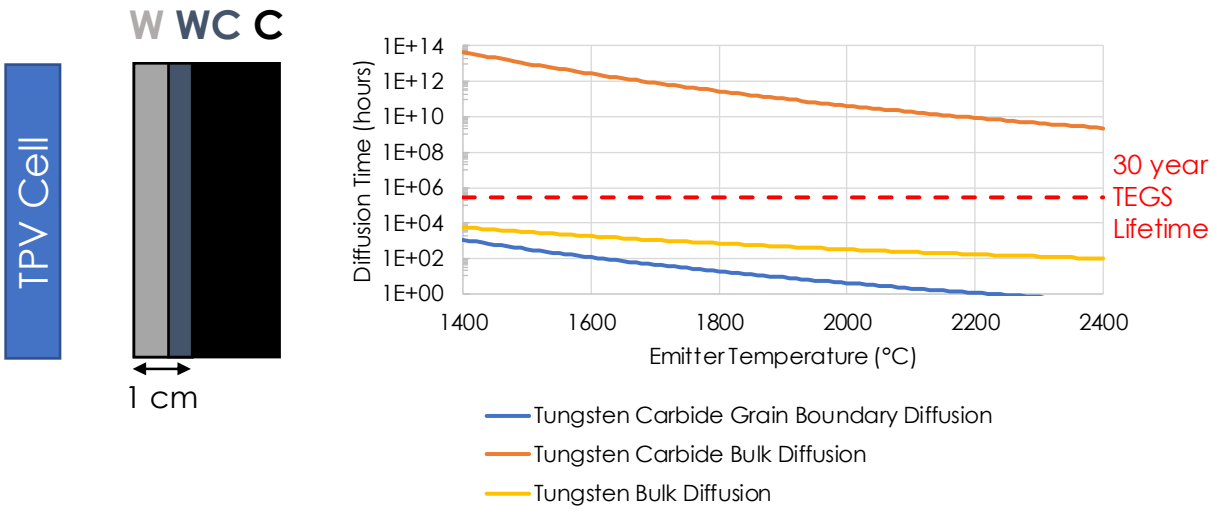

Figure 37 – Carbon diffusion time for a 1 cm thick layer of tungsten and tungsten carbide, with both bulk and grain boundary diffusion considered.

2.3.4. Sealing

Another issue with the tungsten coil wrapped approach is potential leaks in the corners. Any break in the tungsten lining is a path by which carbon can diffuse through as a gas, bypassing the protective tungsten carbide layer, and deposit on the cells directly. To address this, a corner sealing concept was developed that solves both the mechanical strength issue, by supporting each sheet of tungsten on all four sides, and the sealing issue by sintering the sheets to themselves in the corners. Figure 38 illustrates this concept; angled corners with filleted edges allow two sheets of foil to push against each other and seal along each edge.

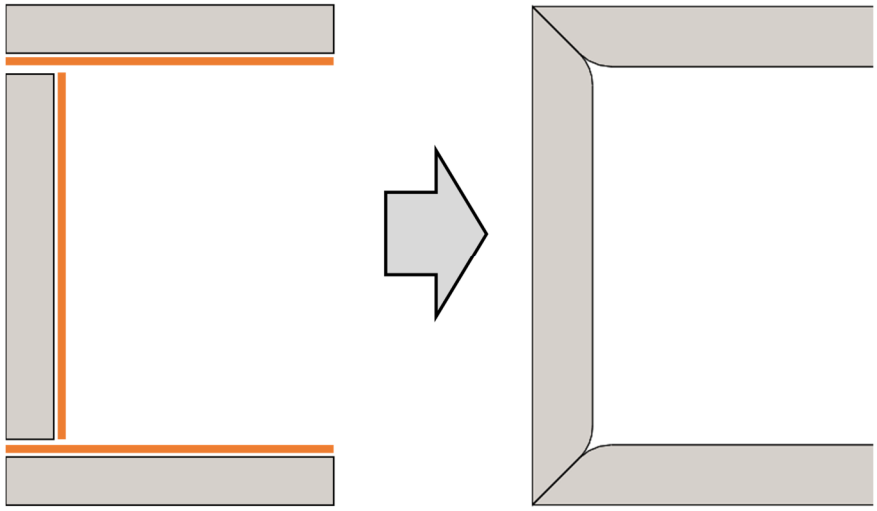

Figure 38 – Leak paths at the corners of a square cavity made from graphite plates and tungsten sheets (left), and an angled corner self-sealing approach that both seals and support the sheets on each edge

Figure 39 shows how the foil sheets and graphite pieces fit together, held in place with carbon fiber composite (CFC) bolts. The melting temperature of tungsten is 3422°C, and a common assumption is that 2/3 of the melting point is sufficient for sintering to occur, ~2190°C in the case of tungsten [34]. With sufficiently flat and clean surfaces, pressed together with the carbon fiber bolts, it was expected that the tungsten would sinter to itself and fully seal the cavity.

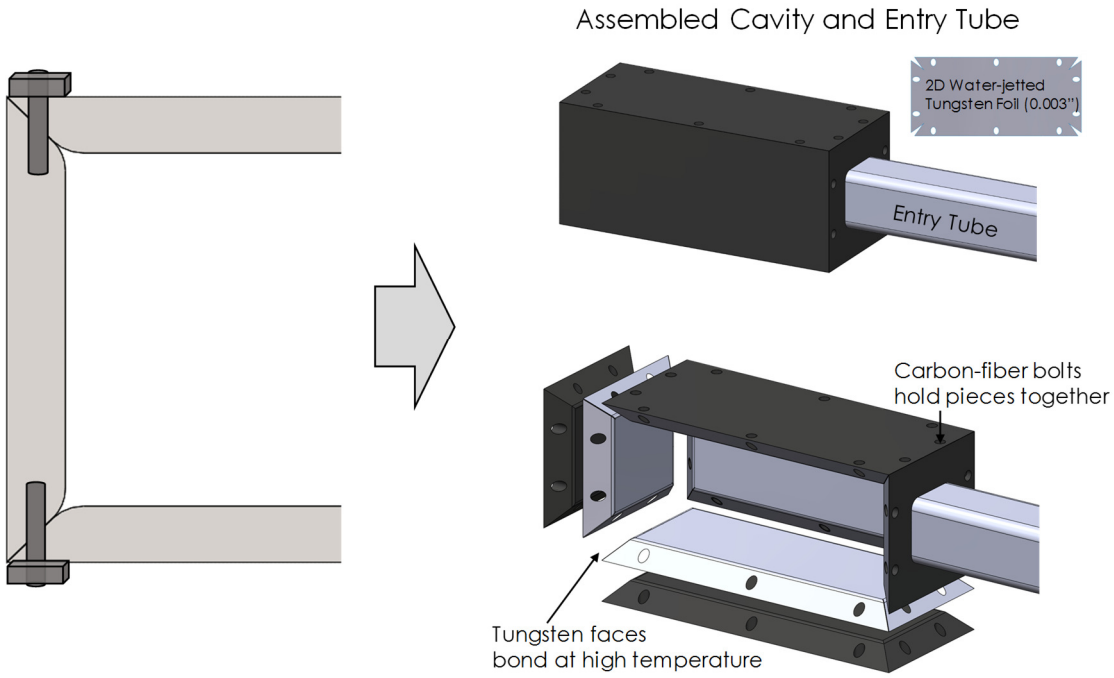

Figure 39 – Carbon fiber bolts compress angled corners, self-sealing the tungsten foil.

2.3.5. Fabrication

The aforementioned design was fabricated using high-density DS-4 grade graphite from an electrical-discharge machining (EDM) blank manufacturer, Ohio Carbon Blank, capable of holding tight tolerances in graphite parts. The graphite itself is DS-4 grade graphite from Mersen Graphite. 0.003" thick tungsten foil was sourced from The Rembar Company, and laser-cut to form the 2D sheets. Figure 40 shows the assembly process including CFC studs and nuts used to hold the plates together, the tungsten foil bent around the filleted corners, and the fully assembled cavity and entry tube. During one test, sintering temperature were achieved, but there was also a water leak that oxidized the tungsten, also shown in Figure 40 (blue material). This experiment was helpful, however, as the complete sealed tungsten cavity was extracted with sintered edges that held together even after removal of the graphite support scaffolding.

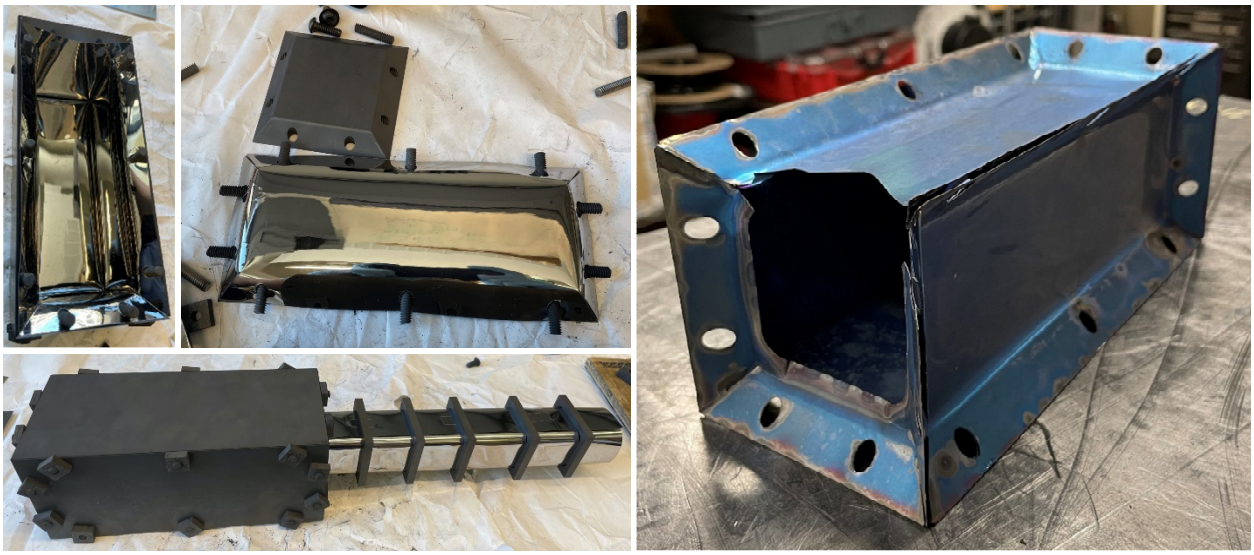

Figure 40 – Assembly of the self-sealing cavity using tungsten foil sheets, graphite supporting plates, and carbon fiber composite studs (left). A self-sealed tungsten cavity holding together with the graphite supports removed. Blue color is due to oxidation from a water leak (right).

2.4. SUMMARY

In this chapter, a discussion of some of the experimental challenges of ultra-high-temperature experiments is provided. Additionally, an explanation is provided for the design process and considerations for a scalable TPV emitter for applications in the Thermal Energy Grid Storage system proposed in Chapter 1.

Chapter 3

3. TPV Cell Room Temperature Design Components

3.1. INTRODUCTION

Using tungsten as an emitter material for TPV results in only small amounts of sublimation and deposition contaminating the cell surfaces. Even with such a low vapor pressure emitter material, however, the cells' performance will degrade as early as year after installation, shown in Figure 33. Additionally, if any contaminants or carbon make their way from the hottest part of the system this small quantity of deposition could quickly become significant. The remainder of this thesis will address a novel, patented solution to this problem, termed the Sweeping Noble Gas Curtain (SNGC). This chapter evaluates the potential of this approach, with several models and validating experiments.

3.2. SWEEPING NOBLE GAS CURTAIN (SNGC)

The Sweeping Noble Gas Curtain concept, illustrated in Figure 41, seeks to blow sublimated emitter material away from the surface of the cells with a blowing gas layer that is transparent to the light. This concept was inspired by a number of industrial cleaning and isolation processes, commonly called air curtains. With a high enough flowrate of clean gas, the diffusion of emitter material to the cell surface should be reduced. The next several sections predict the velocity and gas jet thickness needed to reduce deposition by roughly an order of magnitude, going from the modelled 3 nm/year of deposition to 3 nm/decade, which would be a much more economically acceptable cell cleaning frequency.

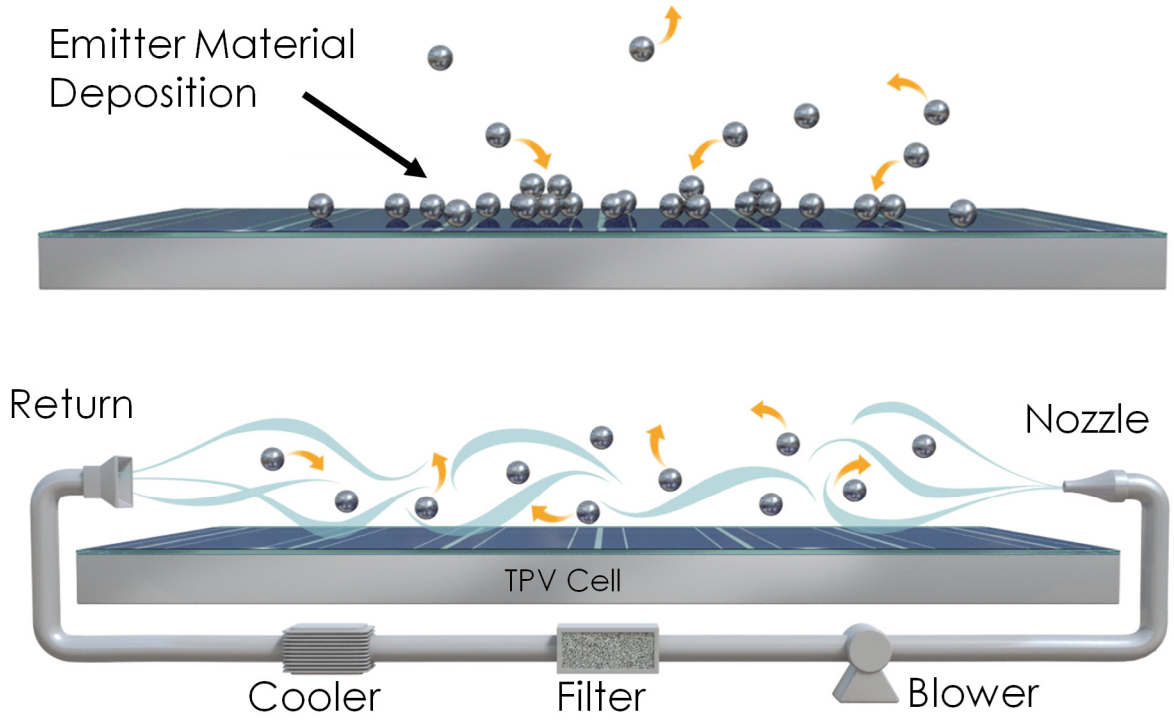

Figure 41 – Sweeping Noble Gas Curtain (SNGC) concept, showing a sweeping gas layer preventing deposition of sublimated emitter material from coating the TPV cells.

3.3. UNIFORM VELOCITY MODEL

To prevent this contamination process, a layer of gas can be blown across the cell, effectively sweeping the evaporated material away before it gets to the cell surface. This approach is enabled by operating the TPV system in a non-vacuum inert environment. Typically, TPV systems are operated in vacuum to minimize convective and conductive parasitic thermal losses. However, at the target operating temperatures, these losses are negligible compared to radiative heat transfer. Gas films have been used extensively in industry to protect surfaces from damage, notably in the design of gas turbines which use gas film cooling to enable higher turbine operating temperatures without compromising blade materials [35]. To evaluate the potential of this sweeping gas layer approach, a simple analytical model can be written to predict a number of relevant design parameters. Figure 42 shows the analyzed case of blowing gas across a cell to protect it from an emitting and sublimating surface.

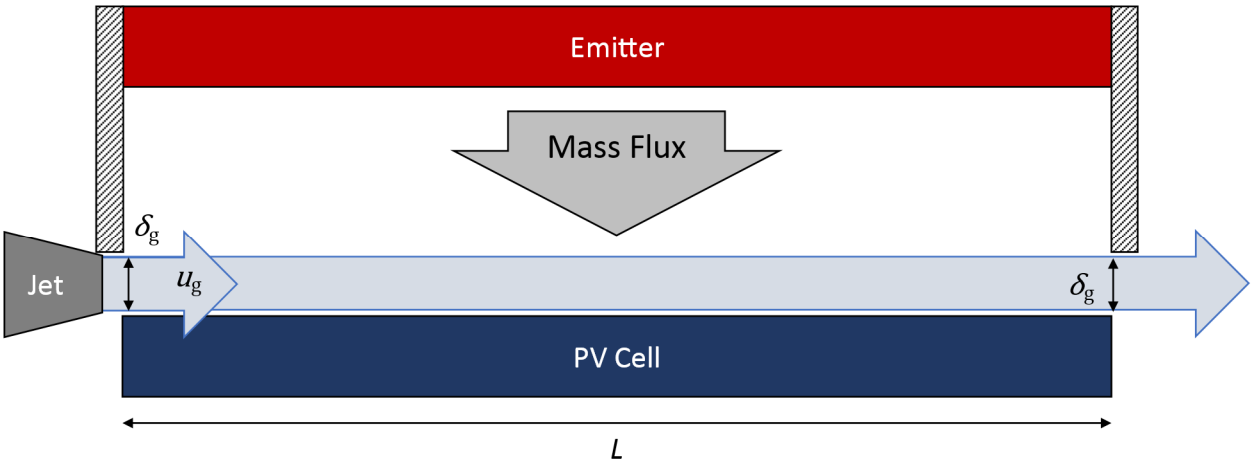

Figure 42 – Schematic of modelled geometry, boundary, and flow conditions

Assuming a laminar, uniform thickness layer of gas flows over a cell with length L between the gas inlet and outlet, an estimate can be calculated for the required gas velocity (u_g) for a given layer thickness (δ_g) to prevent deposition. Based on the laminar assumption, diffusion is the dominant mode of mass transfer through the sweeping gas layer and the mass boundary layer thickness (δ_m) as a function of time can be found using the semi-infinite body approximation [36].

$$\delta_m = 4\sqrt{Dt} \tag{15}$$

In Eq. (15, D is the diffusion coefficient (cm^2/s) and t is time since exposure to a constant concentration boundary condition. Substituting the characteristic time L/u_g for t and rearranging, an equation for required gas velocity can be obtained.

$$u_g = \frac{16LD}{\delta_g^2} \tag{16}$$

This approach, however, assumes that there is a uniform, laminar gas layer flowing across the cell surface, which may not be the case. The Reynolds number of the flowing layer can provide additional insight into what velocities are necessary for this assumption to be valid.

$$Re = \frac{u_g L^*}{\nu} \tag{17}$$

The characteristic length L^* can be either the length of the protected cell, L, or the hydraulic diameter of the flowing layer, $2\delta_g$. To maintain layer uniformity, momentum must dominate over viscous effects in the layer so *Re* should be much greater than 1. Selecting the more conservative $2\delta_g$ characteristic length case ($\delta_g << L$) and a Reynolds number of 100 (2 orders greater than 1), an estimated lower velocity limit could be written as

$$u_g = \frac{50\nu}{\delta_g} \tag{18}$$

To maintain laminar flow in the layer, *Re* should be less than 2300 using the $2\delta_g$ characteristic length or less than $5x10^5$ using the cell length L (typical regime transition Reynold numbers for pipe flow and flow over a flat plate, respectively). This sets the maximum velocity limit to either Eq. (19) or (20), whichever is smaller.

$$u_g = \frac{1150\nu}{\delta_g} \tag{19}$$

$$u_g = \frac{5 \cdot 10^5 \nu}{L} \tag{20}$$

One limitation of this approach is that predicting the required velocity with Eq. (16) does not account for the development of any momentum or thermal boundary layers that may form at the cell surface or interface between the flowing and stagnant gas region. In this way, the dynamics of the system are much more complex than this simple model, and thus require validation with a more robust numerical approach, as described in section 3.5.

3.4. WALL JET LITERATURE

The fluid mechanics of streams of gas flowing over a surface, i.e. "wall jets," have been studied since the 1950s. As discussed in the previous section, the transition from laminar to turbulent flow is a potential concern for ensuring SNGC effectiveness. An early paper on wall jets by Glauert [37] addresses this laminar turbulent transition and provides a formulation for what the velocity profile of a turbulent jet

might look like. Figure 43 compares similarity solutions for a laminar and turbulent jet. Based on this analysis, the transition to turbulence may not be a critical problem previously thought. In fact, the high velocity gas closer to the cell surface (0 on the x-axis) more closely replicates the uniform velocity assumption made in section 3.3. While this theoretical formulation is useful, the incorporation of heat transfer along with the fluid flow lends itself towards a numerical modelling approach to better capture the combined physics.

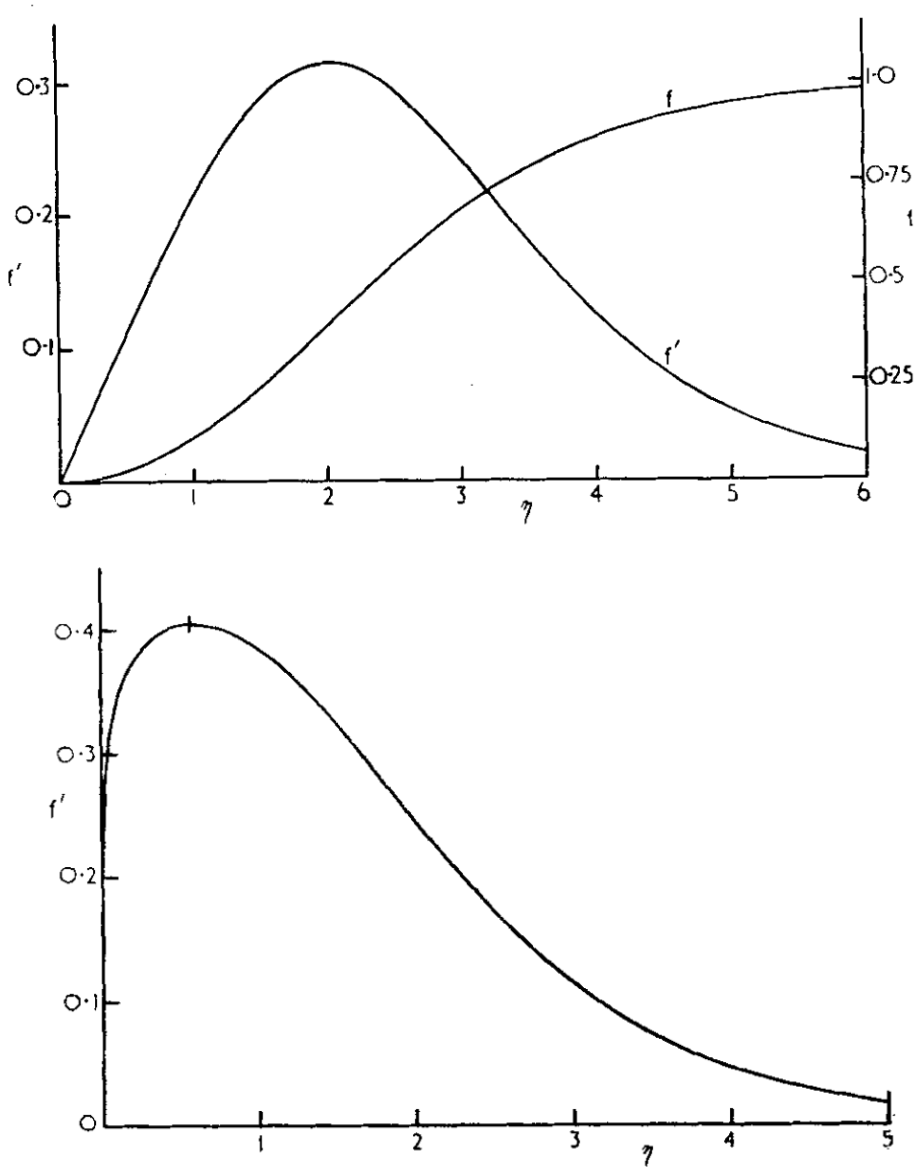

Figure 43 – Wall Jet Velocity Profiles for a laminar (top) and turbulent (bottom) wall jet. Figure reproduced from Glauert [37]

3.5. NUMERICAL MODELLING

3.5.1. Model Schematic and Parameters

The modelled geometry is identified in Figure 44 along with relevant mass and heat-transfer boundary conditions, additionally summarized in Table 1. The length-scales used for the simulation are of the same order as predicted for the full-scale system. A region of stagnant gas was also included in the geometry between the sweep layer and emitter to better simulate the fluid dynamics of the final system where a stagnant region reduces convective heat loss from the emitter. Tungsten concentration at the emitter and cell surfaces were calculated using the following equation

$$C_{\text{surf}} = \frac{P_{\text{vap,W}}}{R \cdot T_{\text{surf}}} \tag{21}$$

where $P_{\text{vap,W}}$ is the temperature dependent vapor pressure of tungsten based on tabulated values, T_{surf} is the cell or emitter surface temperature, and R is the ideal gas constant. The temperature dependent diffusion coefficient (D_{AB}) of tungsten ($_A$) in argon ($_B$) can be determined using Eq. (6) from the previous section.

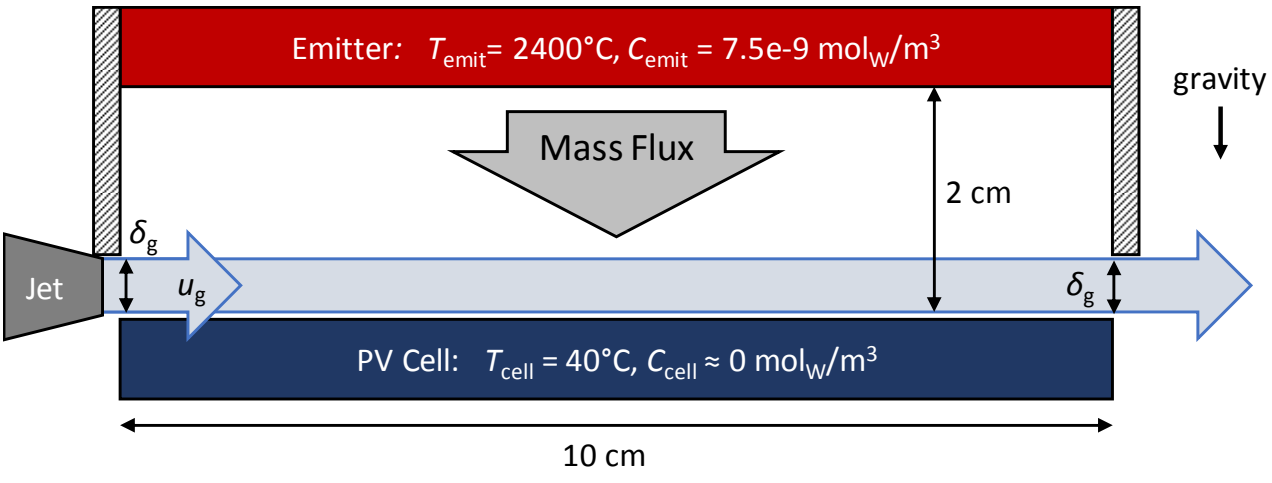

Figure 44 – Schematic of modelled geometry, boundary, and flow conditions.

COMSOL Multiphysics was used for the simulation with the CFD module. Natural convection was modelled, but contributes minimally to the results due to the orientation of the hot and cold surfaces with respect to gravity, in this case. The simulation used a time-dependent solver with 60 seconds of study time to ensure a representative steady state was reached (shorter runs resulted in changing layer behavior). A no-slip boundary condition was used on all boundary surfaces. The cross-hatched walls are adiabatic and no-flux boundary conditions.

Two jet thicknesses (δ_g) were modelled, 2 mm and 5 mm, to capture the impact of jet thickness on required jet velocity. Using the viscosity properties of argon at stp. ($\nu = 1.27\text{x}10^{-5}$ m^2/s) and Eq. (2), the required velocities for the 2 mm and 5 mm jets were 1.5 m/s and 0.25 m/s, respectively. Both of these velocities also satisfy the Reynolds number constraints shown in Eqs. (4)-(6), summarized in Table 1.

Table 4: Summary of parameters, inputs, and calculated values for numerical model

Parameter	**Value**		**Units**
Inert flowing gas	Argon		-
Emitter material	Tungsten		-
Study duration	60		s
Emitter temperature	2400		℃
Cell temperature	40		℃
Modelled jet thicknesses (δ_g)	2	5	mm
Required velocities (u_g) (Eq. 2)	1.5	0.25	m/s
Minimum velocities (Eq. 4)	0.3	0.13	m/s
Maximum velocities (Eq. 5)	7.3	2.9	m/s
Modelled velocity ranges (u_g)	0-6	0-3.2	m/s

3.5.2. Modelling Results

The results of the numerical modelling are consistent with the predictions for required flow velocities at the two considered jet thicknesses, 2 mm and 5 mm. Figure 45(a) shows tungsten deposition rate as a function of flow velocity for the two jet sizes across the modelled velocity ranges. Figure 45(b) shows three selected cases, indicated with red dots in Figure 45(a). The flow velocity chosen for each jet thickness was the lowest velocity after which the deposition rate starts to remain constant. The selected velocities, 1 m/s for the 2 mm case and 0.4 m/s for the 5 mm case show some agreement with the modelled values of 1.5 m/s and 0.25 m/s, respectively. It is hypothesized that the deviation can be

accounted for by the additional complex flow dynamics of the sweeping gas layer and stagnant gas region.

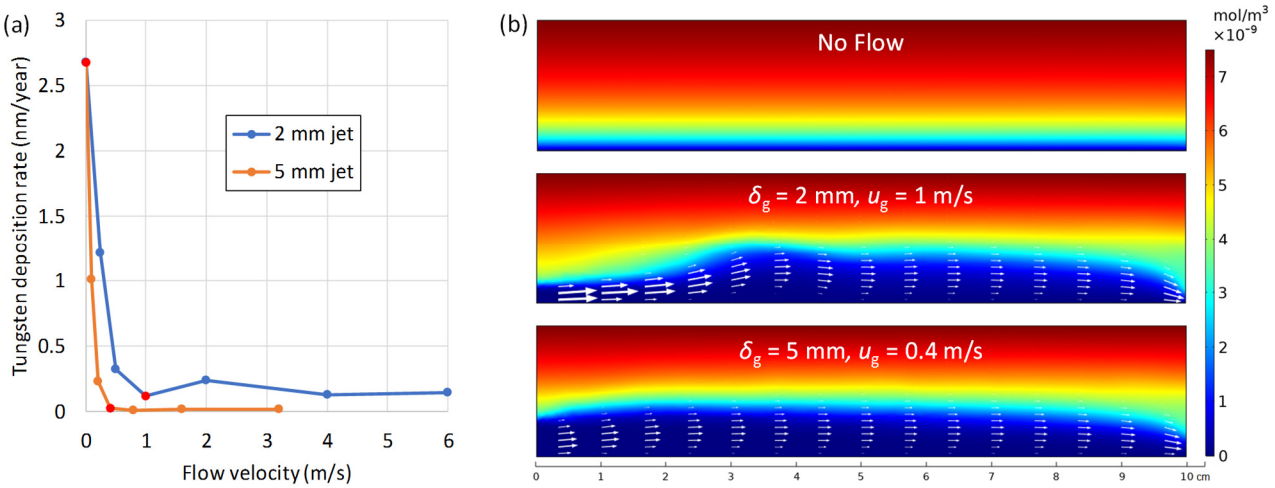

Figure 45 – (a) Tungsten deposition rate in nm/year as a function of flow velocity. Red data points indicate selected cases shown in (b). (b) Comparison of three representative tungsten concentration profiles where deposition rate begins to remain constant: no flow, a 2 mm thick jet with 1 m/s initial flow velocity, a 5 mm thick jet with 0.4 m/s initial flow velocity. White arrows indicate flow direction and relative velocity magnitude.

3.5.3. Model Extension

The next step beyond the simple case presented in the previous section, is to consider a more complex, realistic scenario and see if the SNGC is still effective. A representative square cold plate geometry was modelled in COMSOL, with gas jets blowing across the "cell" surfaces. This laminar flow model accounted for natural convection in the gas, with gravitational acceleration in the negative y-direction, heat transfer and mass diffusion in the gas, and an emitter at 2150°C. Figure 46 shows the results on this model including a color map showing concentration of the emitter material, graphite in this case, for a jet flow velocity of 2 m/s. This model clearly shows several orders of magnitude reduction in deposition rate with a flow velocity of 2 m/s or higher.

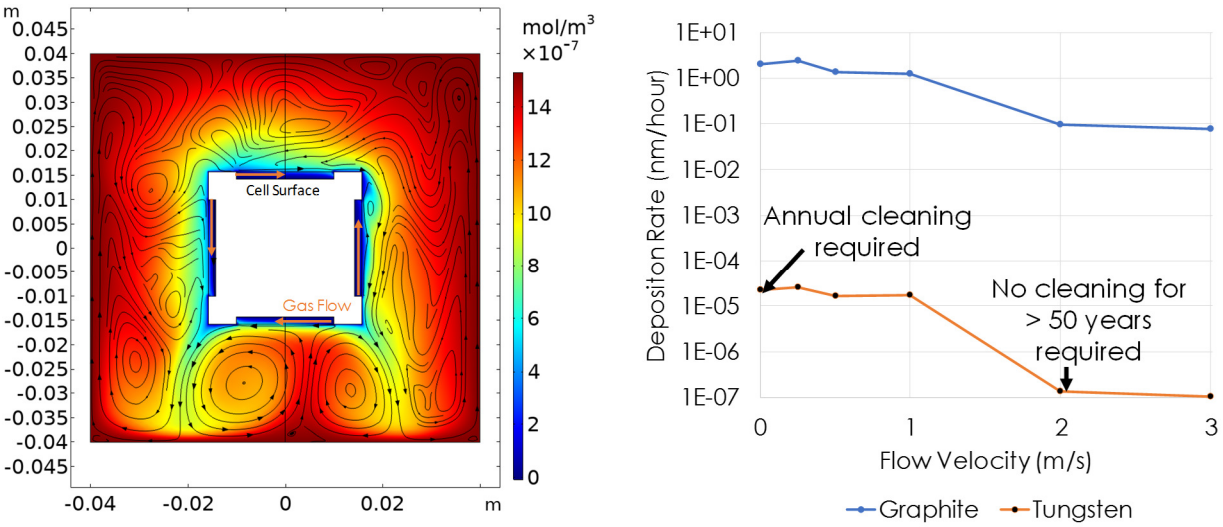

Figure 46 – 2D COMSOL modelling results for a graphite emitter with an flow velocity of 2 m/s. Color map represents concentration of sublimated emitter material, and black lines/arrows represent streamlines (left). Comparison of relative deposition rates of graphite and tungsten in the representative square geometry configuration (right).

3.6. EXPERIMENTAL VALIDATION

Due to the challenges of high-temperature experimentation described in Chapter 2, validating the SGNC modelling is difficult. Running two identical experiments often yields different results, due to the complexity and significant variability in environmental conditioning that occurs for each high-temperature run. There are a number of transient process that can change each run, including contaminant concentration in the insulation, heater and lead contact resistances, and measurement location of cavity temperature. Additionally, the deposition rates in the high-temperature case are extremely small, by design, and may show little deposition without months of testing. More detail on the high-temperature testing apparatus is provide in Chapter 5. The model was tested without the time and complexity of high-temperatures with a low-temperature, tabletop proxy experiment requiring no vacuum chamber and capable of running many tests of different flow rates per hour.

3.6.1. Low-Temperature Proxy Experiments

One challenge with designing a low-temperature experiment is recreating the nearly zero concentration boundary condition on the "cell" side. This ultra-low concentration is important, because in the high-temperature case the sweeping gas and surface both have extremely low concentrations. If the surface had a higher concentration than the gas, it would actually sublimate material into the gas, clearly deviating from the high-temperature case. Water was chosen as the evaporating medium, with a liquid nitrogen cooled cold plate to replicate the low concentration boundary. Figure 47 shows a schematic for a comparison model, showing how the water case is a good corollary for tungsten deposition.

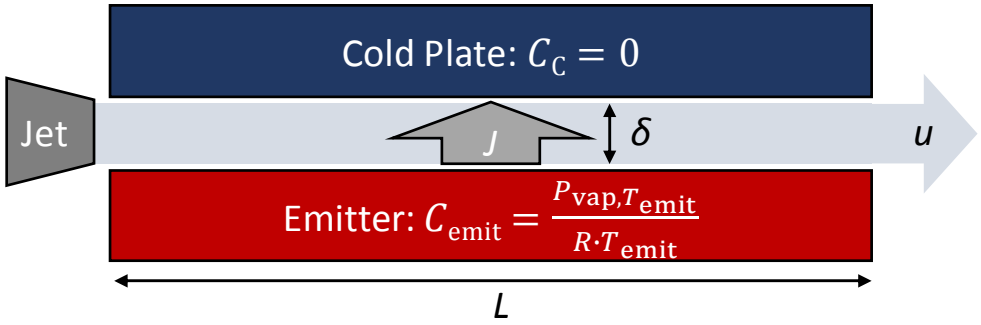

Figure 47 – Proxy experiment comparison schematic indicating variables and dimensions of the comparison geometry.

Emitter concentration is calculated using Eq. (21), the concentration at the cell is taken to be zero, the flow velocity, u, and distance, δ, between the plates, and the length, L, are all held constant between the high and low temperature cases. Eq. (23) is derived from a ratio of a Fick's law formulation of diffusion rate, Eq. (22). Eq. (24) is a formulation of the Peclet number, comparing the effect of diffusive and advective mass transfer. With two cases of similar Peclet numbers, the SNGC could be expected to perform similarly as the of the moving gas and diffusing material on the should have similar relative contributions on the total mass transfer.

$$J = -D\frac{\Delta C}{\delta} \tag{22}$$

$$\frac{J_{H_2O}}{J_W} = \frac{D_{H_2O}}{D_W} \cdot \frac{\Delta C_{H_2O}}{\Delta C_W} \tag{23}$$

$$Pe = \frac{Lu}{D} \tag{24}$$

Table 5 shows the results of this comparison, with the temperature conditions, calculated concentrations at both surfaces, temperature dependent diffusion coefficients (tungsten in argon, water in nitrogen, evaluated at the average temperature) and relative fluxes shown. Additionally, the Peclet numbers are compared and are very close for both cases.

With the 10 order of magnitude differences in fluxes, a 3 nm/year deposition rate of tungsten could be replicated within minutes with the water experiment.

Table 5 – Comparison of experimental cases including relative fluxes and Peclet numbers

Emitter Material	T_{emit}	T_C	C_{emit} **[mol/m^3]**	C_C **[mol/m^3]**	D **[m^2/s]**	J_{H2O}/J_W	L **[cm]**	u **[m/s]**	Pe
Tungsten	2400°C	40°C	1.6e-10	~0	4e-6	6e10	10	1	2.5e4
H_2O	20°C	-200°C	1.7	1.9e-27	3.3e-6		10	1	3e4

3.6.2. Experimental Apparatus

Figure 48 shows the experimental apparatus designed to test the water case. Ultra-high purity (UHP) nitrogen gas was used a sweeping gas, providing a lower cost and less hazardous alternative to argon. The experiment was design with two testing zones, both cooled with the same liquid N_2 bath, but one with a sweeping gas and one without. This control zone helped eliminate outliers caused by human error from the test data, as the control zone could be compared across many different flow velocities. The water batch was temperature controlled, and held at 20°C for the duration of all testing. This provided a known concentration boundary condition at the bottom of the chamber. The sweeping gas was also routed through the cold plate to ensure it was isothermal with the deposition surfaces, and the surface maintained the zero-concentration boundary condition. Thermal paste (ARCTIC MX-5) was used between the

cooling bath and cold plate to minimize thermal resistance, but the paste's performance at cryogenic temperatures is unknown (it becomes solid and brittle).

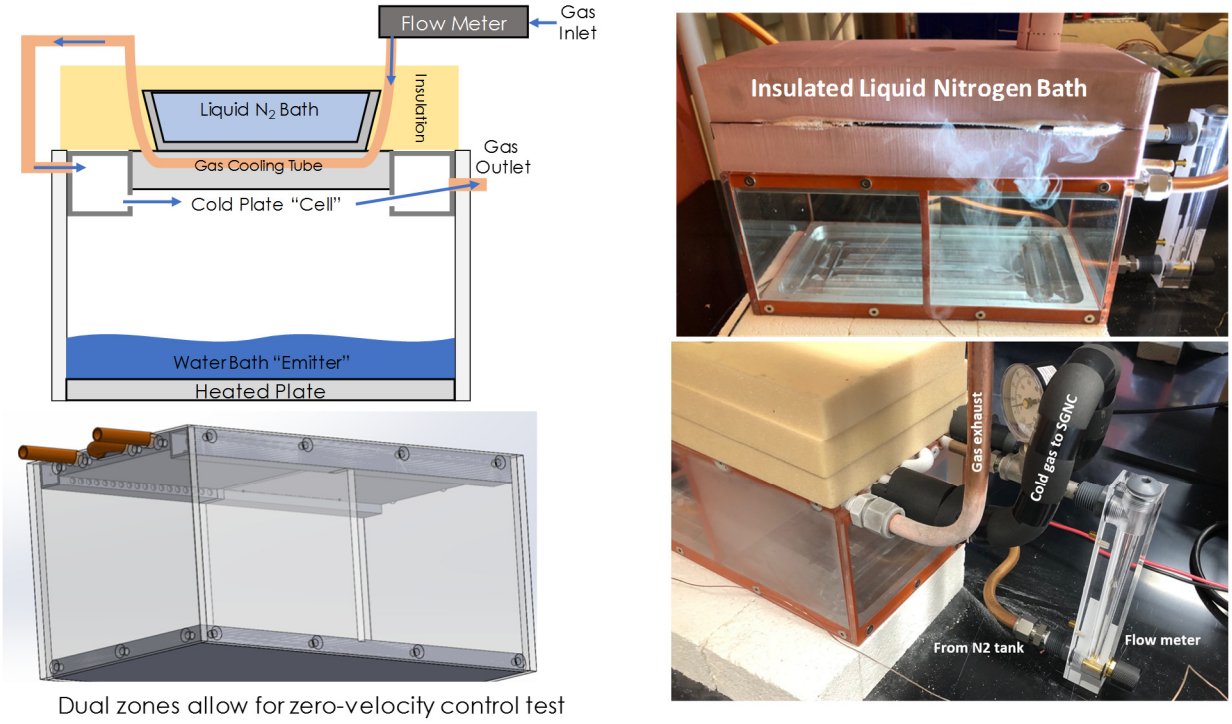

Figure 48 – Proxy experimental apparatus including schematic (top left), CAD model of the dual testing zones (bottom left), and images of the realized apparatus (right).

The first nozzle/jet geometry considered, shown in Figure 49, was a simple slot cut in the nozzle manifold with the goal of a uniform and thick jet of gas. However, as gas was introduced perpendicularly to the gas flow direction, the axial momentum component caused severe non-uniformity of the outlet velocity.

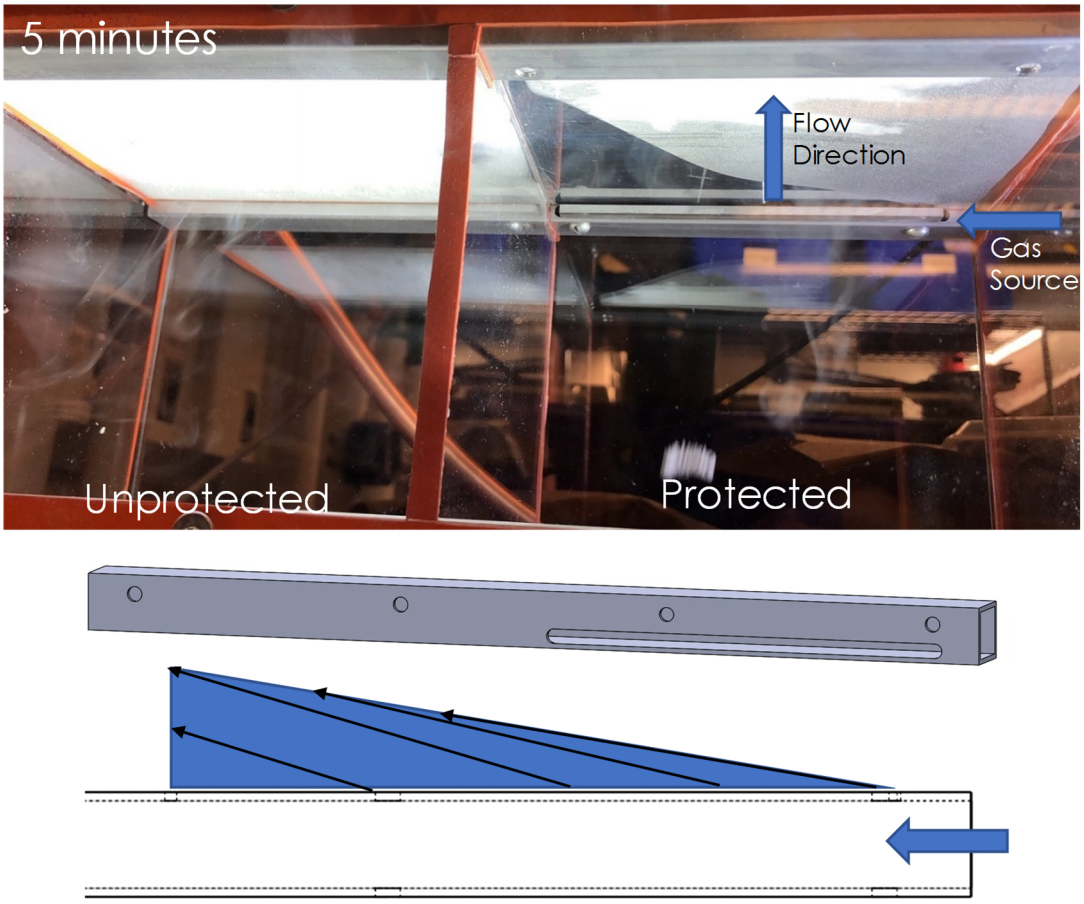

Figure 49 – Initial nozzle geometry caused significant non-uniformity in jet velocity and thereby deposition rate

The second iteration, shown in Figure 50, used individual openings to mitigate the axial velocity component, and a porous medium inside the manifold to reduce the pressure differences in the manifold and improve uniformity. This approach resulted in uniform flow, but only in large discrete jets that did not completely shield the condensing surface from deposition.

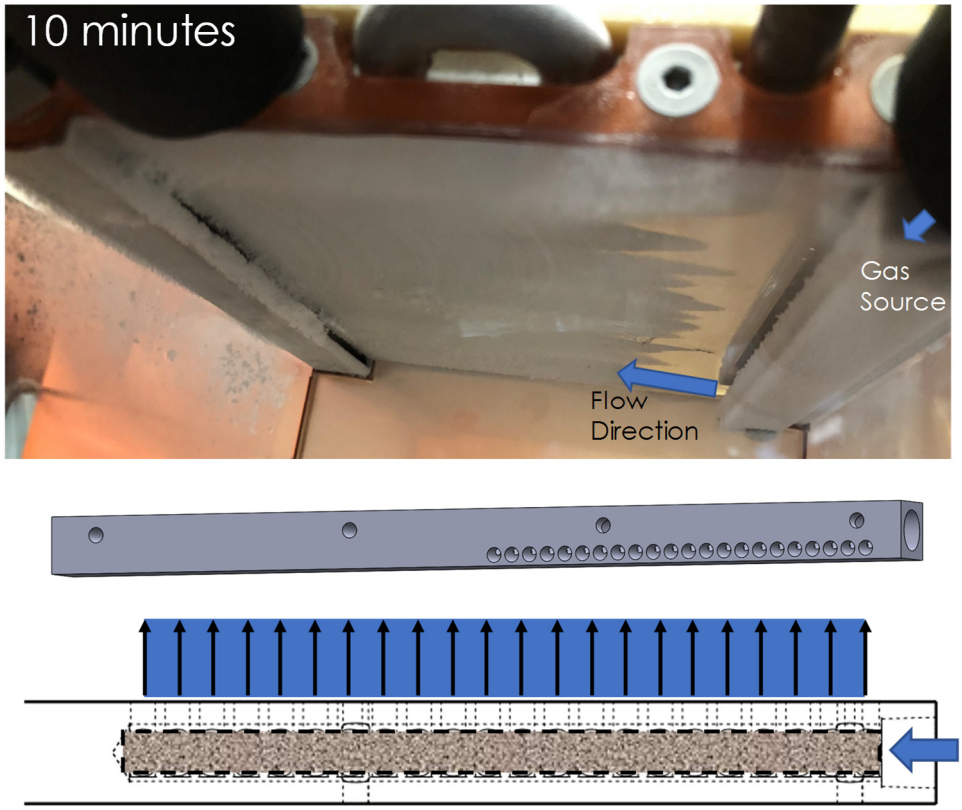

Figure 50 – Improved nozzle geometry reduced axial non-uniformity in jet velocity, but introduced a discretization of the jet causing clear variation in deposition rates

The final iteration, shown in Figure 51, used more, smaller openings with a 90° diffuser to improve uniformity and decrease the discrete jet behavior observed in the prior nozzle designs. Performance of this updated nozzle geometry was deemed sufficient to estimate the performance of the SGNC for the low-temperature experiment based on the more uniform deposition profile.

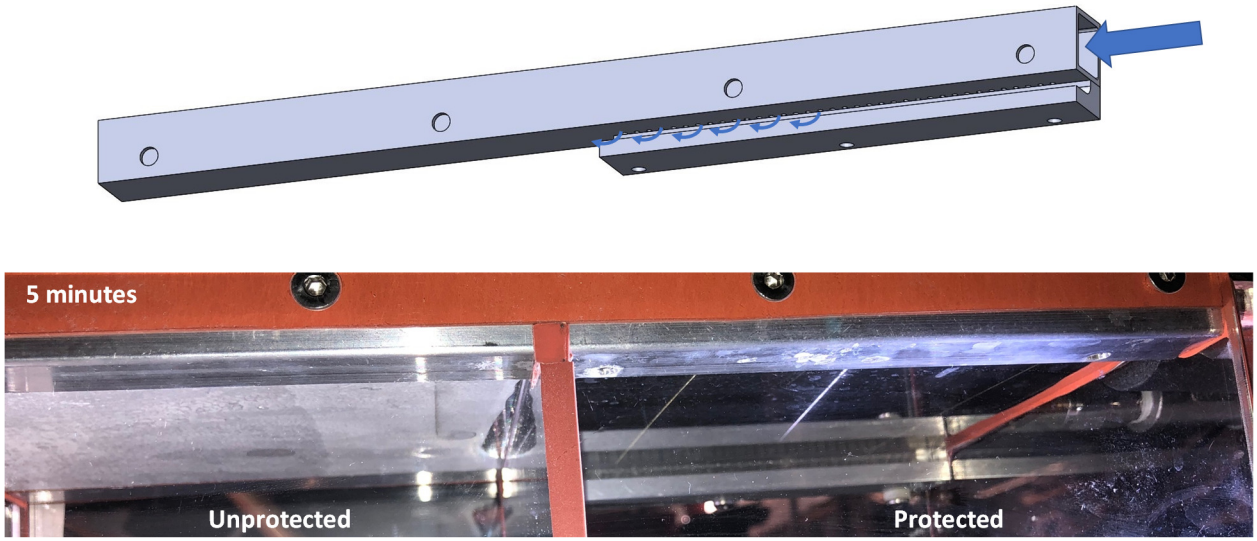

Figure 51 – Final nozzle geometry configuration (top) and example experiment showing the proxy SNGC efficacy after 5 minutes with a flow velocity of 2.5 m/s (bottom).

3.6.3. Preliminary Experiments

3.6.3.1. Procedure

Each test involved filling the liquid nitrogen bath and starting gas flow at a specified flow rate corresponding to an average flow velocity, dictated by the jet thickness and width of the testing region. The bath was allowed to fully boil off over the course of the experiment (2-5 minutes), and the bath was then filled with warm water to melt the deposited frost layer. Gas flow was stopped as soon as the frost that had formed on the cold plate began to melt from the warming cold plate. Once the water was sufficiently defrosted, the deposited material was collected from each surface using a pre-weighed absorbent pad. The time between initial cooling and the beginning of defrosting was recorded. The mass of the pad was measured before and after each test on a +/- 0.001g balance, and the total deposited material was divided by the experimental time to determine deposition rate. This procedure showed good repeatability with a standard deviation between 3% and 50% of the measured deposition rates. 2-5 data points were taken and averaged for each flow condition.

3.6.3.2. Results

Figure 52 shows the results of these preliminary experiments, plotting average deposition rate against flow velocity. The deposition rate shows a decreasing trend with higher flow velocity, as expected, but shows significant deviation from both the modelled 2D results. To better understand the results, the 2D model was expanded to 3D with the hope of better model agreement. While the agreement improved, there was still more than an order of magnitude difference from measured results.

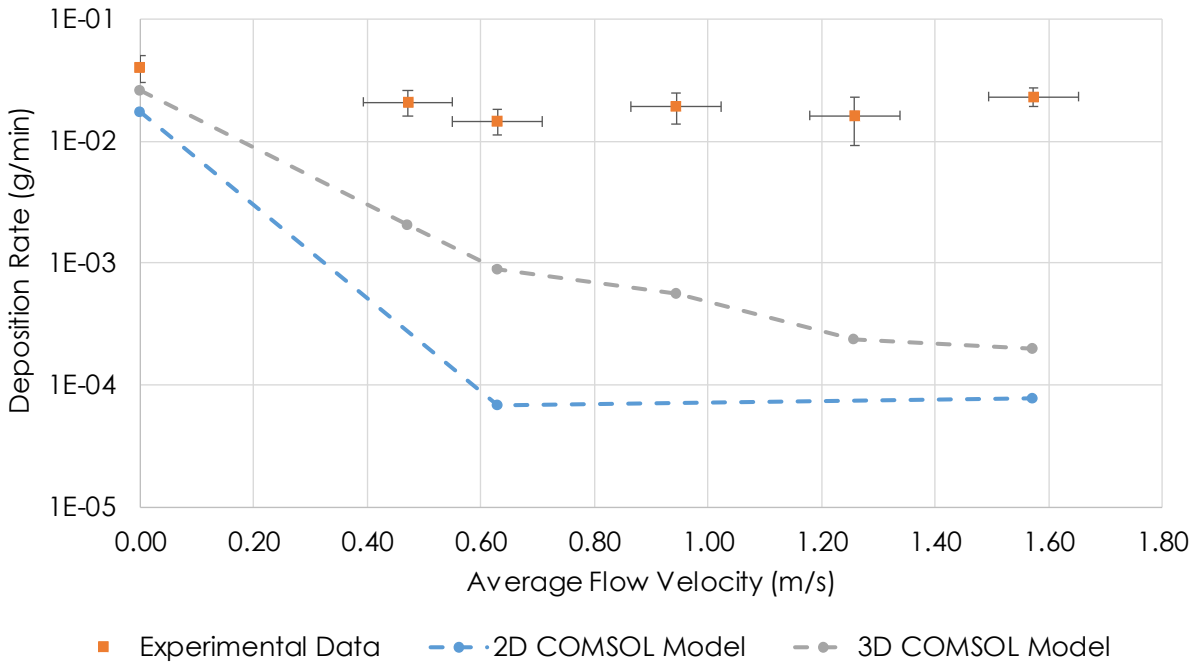

Figure 52 – Preliminary proxy experimental results showing deposition rate as a function of average flow velocity compared to a 2D and 3D COMSOL model.

3.6.4. Experimental Error Analysis

The discrepancies between the modelled and observed behavior prompted a thorough investigation into its origin or source, to better understand the system. The following potential sources of error were identified as follows, with each topic explored further in the following three sections:

1. Temperature Errors
    a. Water bath temperature measurement
    b. Sweep gas and cold plate temperatures

2. Non-linear deposition rates due to frost build up
3. Modelling issues from sub-optimal numerical solver meshes

3.6.4.1. Temperature Errors

Sensitivity of vapor pressure and thereby water concentration to temperature was a primary concern, as this could change the diffusion driving forces and result in an incorrect prediction of deposition rate. For the water bath, a +/- 5°C deviation from the 20°C set point only yielded a +/-30% variation in vapor pressure. However, while this deviation is significant, it is far from the greater than one order of magnitude discrepancy in modelled and experiment results.

The sweep gas and cold plate temperatures were not measured in the initial experiment, assumed to be very close to the liquid N_2 temperature. During this error analysis, the sweep gas was measured to be only -10°C, instead of the idealized -200°C. Table 6 compares calculated concentrations for three condenser/"cell" temperatures. From Eq. (22), the material flux scales with the concentration gradient so the difference in concentration between the "emitter" and "cell" corresponds to the mass transfer driving force. The -10°C case has a condenser concentration that is non-negligible when compared to the emitter concentration, this change could impact the diffusive mass transfer. The -100°C case, however, still has a low enough condenser concentration to prevent any significant difference in mass transfer driving force. Based on this analysis, the gas is not cold enough in this initial experiment to accurately match a model. An improved apparatus is described in the next section that accounts for this error.

Table 6 – Comparison of emitter and cell concentrations (C) of water in nitrogen at different temperature (T) conditions

T_{emit}	T_C	C_{emit} [mol/m^3]	C_C [mol/m^3]
20°C	-200°C	1.7	1.9e-27
20°C	-100°C	1.7	1.9e-7
20°C	-10°C	1.7	0.12

3.6.4.2. Non-Linear Deposition Rates

The second identified source of error was a potential non-linearity in deposition rate with time. With a constant concentration boundary condition resulting from a constant bath and cold plate temperature, the mass transfer rate should be constant and the layer should grow linearly with time. However, the thermal mass of the cold plate could take some time to cool, before deposition begins to occur. This thermal lag is hard to predict when considering the gas flow and thermal resistances between the liquid N_2 bath and the cold plate. Additionally, the growth of a frost layer on the cold plate could have resulted in either reduced deposition due to thermal insulation, or increased deposition due to disruption of the gas boundary layer. To evaluate the impacts of this non-linearity, experiments were performed at for varying test durations and compared, shown in Figure 53. Based on this analysis, the deposition rate was identified as linear only for tests between 3- and 4-minute durations. Tests longer or shorter than that showed deviation from the linear deposition trend. For the next set of experiments, tests were only run between 3 and 4 minutes.

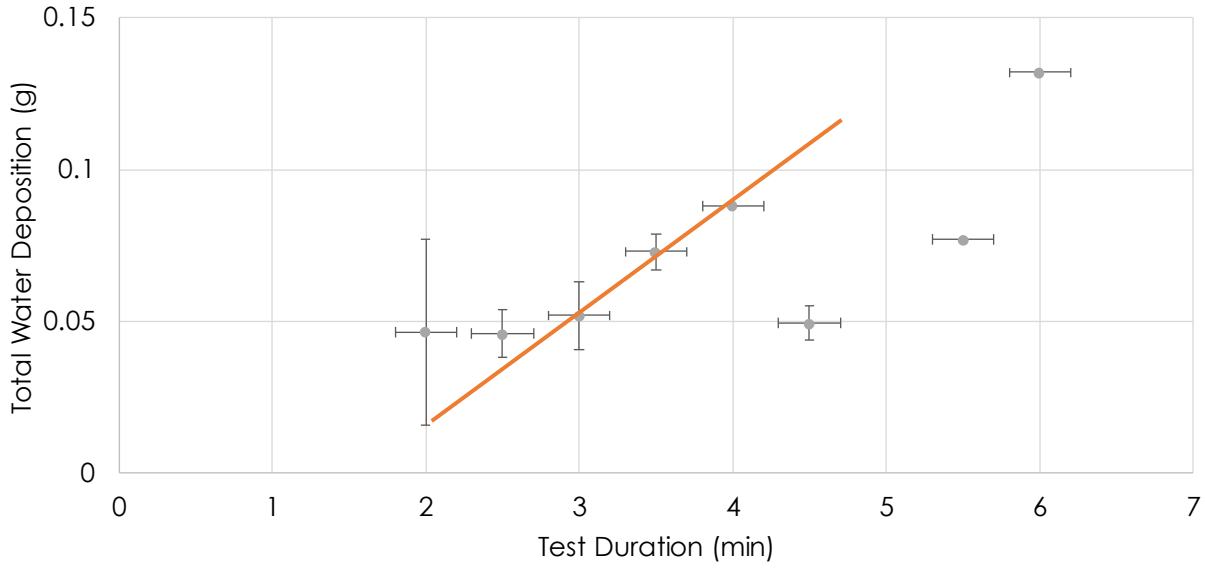

Figure 53 – Total deposition as a function of test duration suggesting a linear deposition rate is only achieved between 3 and 4 minutes of testing.

3.6.4.3. Modelling Issues

The differences in the 2D and 3D COMSOL modelling results shown in Figure 52 suggest modelling errors could be contributing to the deviation from measured values. After trying a number of different approaches, the introduction of boundary layer meshing resulted in significantly improve matching between model and experiment. This was determined to be the most likely culprit for the initial matching errors. Figure 54 shows the mesh for the 3D COMSOL model in the SNGC protected region before and after the addition of additional boundary layers. The updated model is shown in Figure 55 and much more closely matches the initial deposition rate measurements.

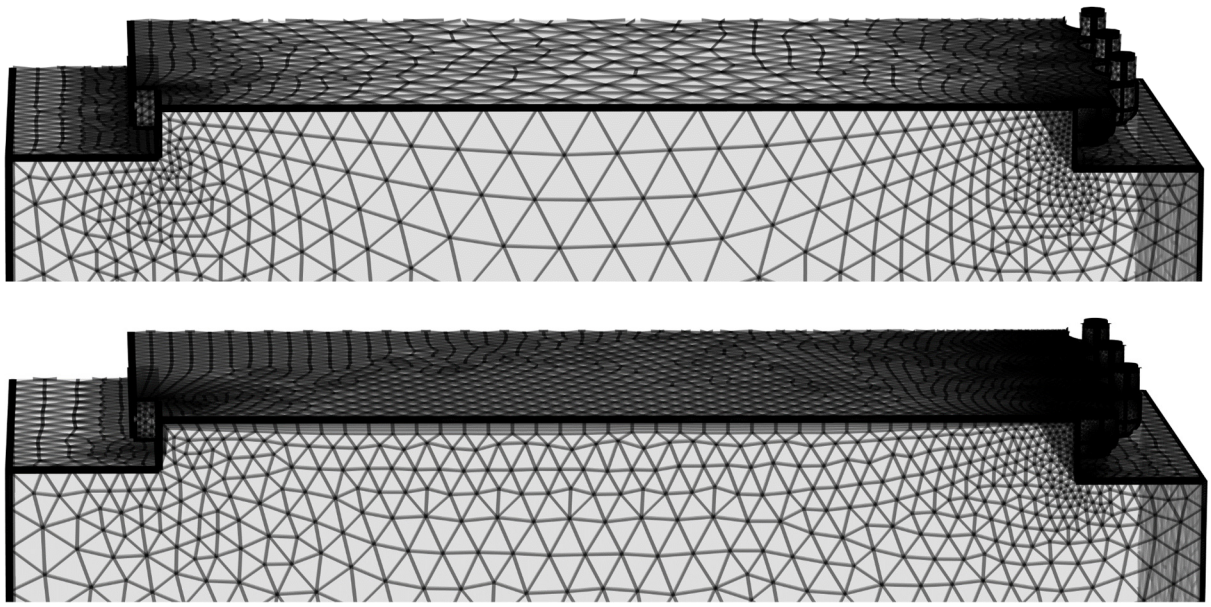

Figure 54 – Mesh comparison before (top) and after (bottom) the additional of additional boundary layers.

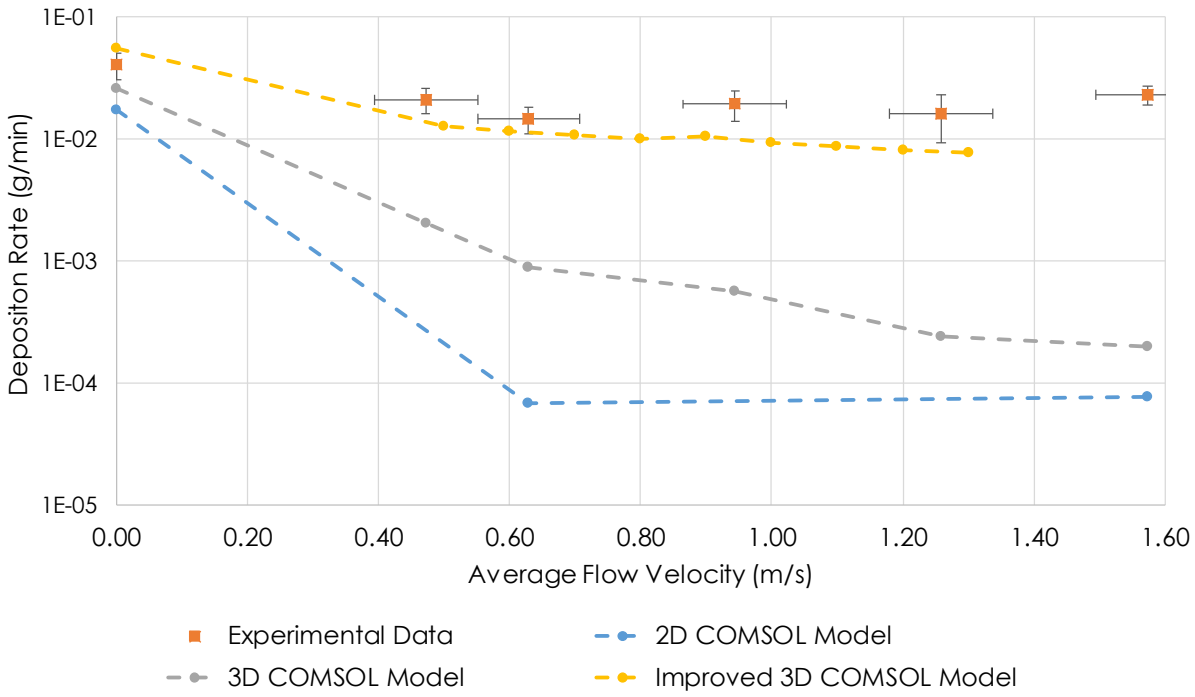

Figure 55 – Modelling results comparison before and after the additional of additional boundary layers (improved model).

3.6.5. Apparatus and Model Modifications

With the findings from the aforementioned error analysis, the apparatus was redesigned to incorporate better gas and cold plate cooling, as this was deemed the most signification deviation from theory. Figure 56 shows the added components and reconfigured liquid N_2 bath. With this new configuration, the thermal resistance between the bath and cold plate surface is also eliminated, as they are fabricated from a monolithic piece of aluminum. Figure 57 shows photographs of the updated apparatus, including the modified monolithic nitrogen bath and cold plate.

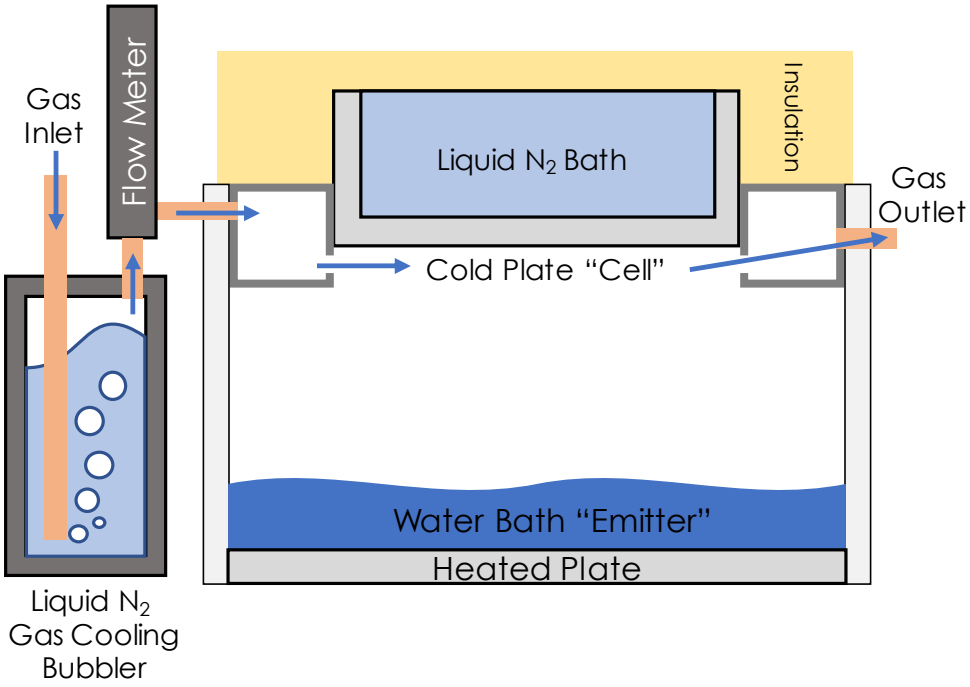

Figure 56 – Modified Apparatus including a liquid nitrogen bubbles, decreasing the sweep gas temperature to below -100°C.

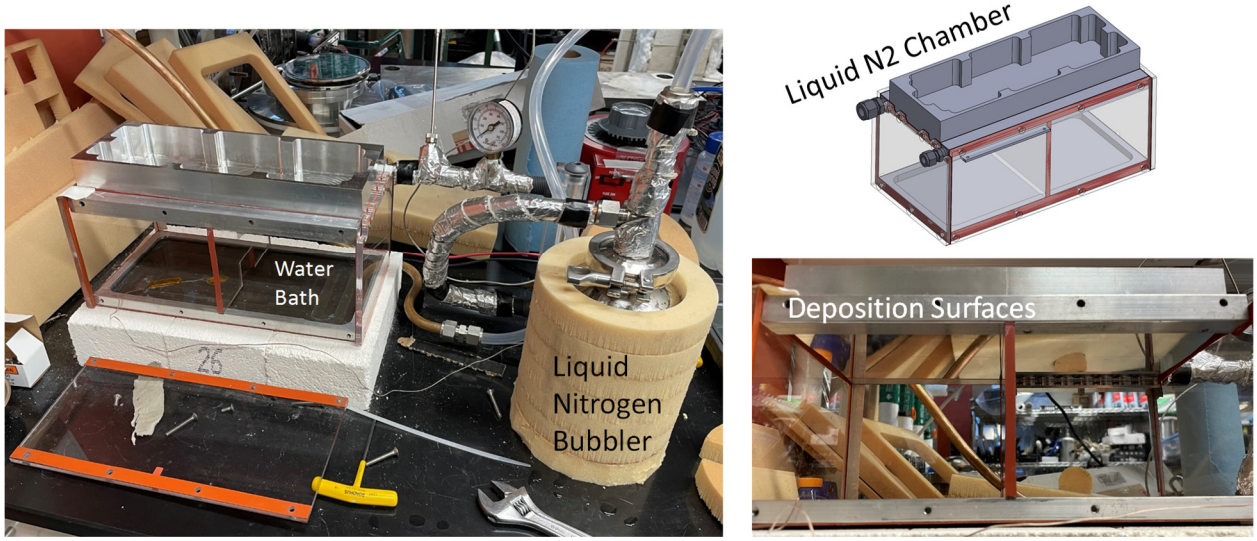

Figure 57 – Modified apparatus after fabrication. Insulated liquid nitrogen bubbler and a direct contact liquid nitrogen container ensure gas and condenser surface temperatures below -100°C.

3.6.6. Validating Experiments

The updated procedure and experimental apparatus described in the previous section yielded significantly improved model-experiment agreement, shown in Figure 58. A reduction in deposition rate was observed corresponding closely to the model prediction. Based on these results, the model and approach to estimating the effectiveness of the SGNC was deemed adequate.

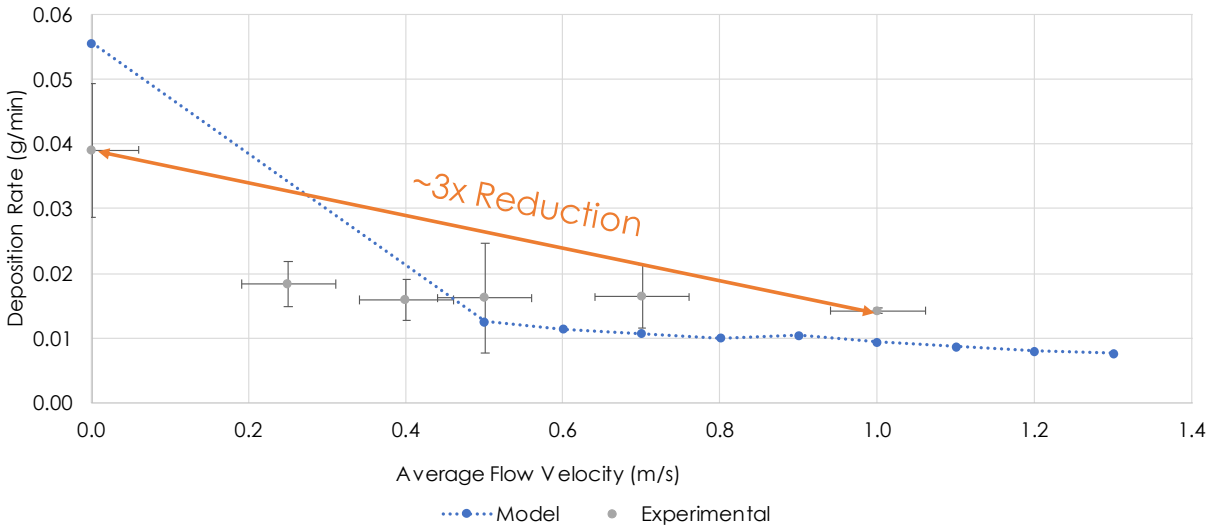

Figure 58 – Final proxy experimental results showing a 3x reduction in experimental deposition rate, following a similar trend to the modelling results.

3.7. SUMMARY

In this chapter, several models are presented, analytical and numerical, predicting the behavior and performance of the SNGC concept. Based on a COMSOL numerical model, the SNGC should be able to reduce the deposition rate of tungsten on to the TPV cells by at least 1 order of magnitude. The model was validated with a low-temperature proxy experiment using water as a representative evaporating and depositing medium, showing good agreement between theory and experiment. Based on these findings, the following chapters will discuss the design and experimentation with a cold plate with an integrated SNGC for use with the high-temperature emitter discussed in Chapter 2.

Chapter 4

4. SNGC and TPV System Integration and Testing

4.1. INTRODUCTION

Using the insights from the models and experiments presented in the prior section, a design was developed for a scalable thermophotovoltaic "cold-side" device capable of integrating the SNGC and cell testing components. The goal of this device was to provide cell cooling, power extraction, and a protective gas layer for a TPV cell exposed to a 2400°C emitter cavity. Figure 59, shows a representative system including a planar TPV cell on a cooling block, with electrical extraction on both sides of the cell and a protective gas layer. Under the 2400°C emitter condition, the amount of light hitting any surfaces of the cell and cold-plate is over 2000 times that of terrestrial sunlight. It is also more than double the critical heat flux of water, the maximum cooling that water can provide to a surface when boiling. This section highlights a number of design components of this integrated device including cooling, gas delivery, compact integration, and fabrication. Particular importance was placed on designing a system that could be scaled for commercial implementation. The goal is for this device to act as a proof-of-concept for an eventual commercial TEGS plant, capable of storing energy and connecting to the grid.

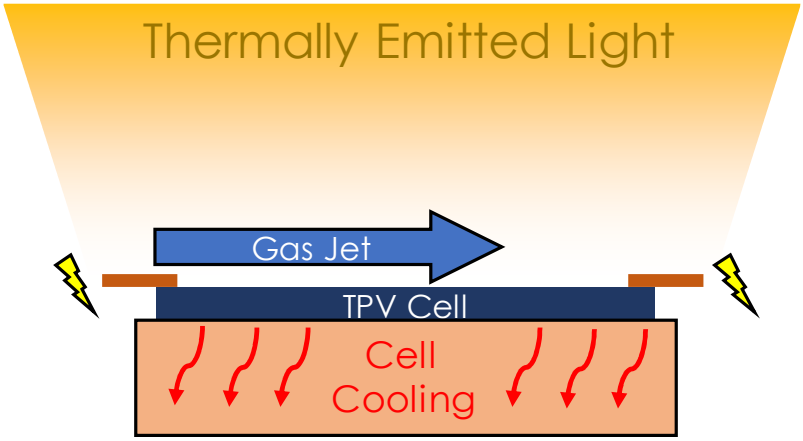

Figure 59 – Integrated system design requirements including cell cooling, power extraction, and a protective sweeping gas layer (SNGC).

4.2. CELL COOLING

The most important objective of the integrated cold plate is to cool the TPV cells under the extreme illumination conditions of a 2400°C cavity. Special care was taken to ensure this cold plate was compatible with the cavity emitter geometry and that the design could be scaled to the full scale TEGS system without significant redesigns.

4.2.1. Geometry

The first step to consider in the design of the cell cooling system was the overall geometry and cell placement. The emitter cavity described in Section 2.3.2 clearly lends itself to a cold plate covered on all sides with PV cells. Figure 60 shows a number of different iterations, with the final square geometry selected. A major consideration for this step was the amount of "inactive" cold plate surface area. Any surfaces not covered by cell and protected with the SNGC are and opportunity for absorption of the high-intensity incident thermal radiation. Minimizing this inactive area is significantly easier with more sides, and the square geometry strikes a good balance between complexity of fabrication, internal volume for coolant channels, and minimized inactive area. The triangular approach, while interesting, leaves sharp corners that may be harder to cool, and does not work well with the proposed SGNC gas routing, described later in this chapter.

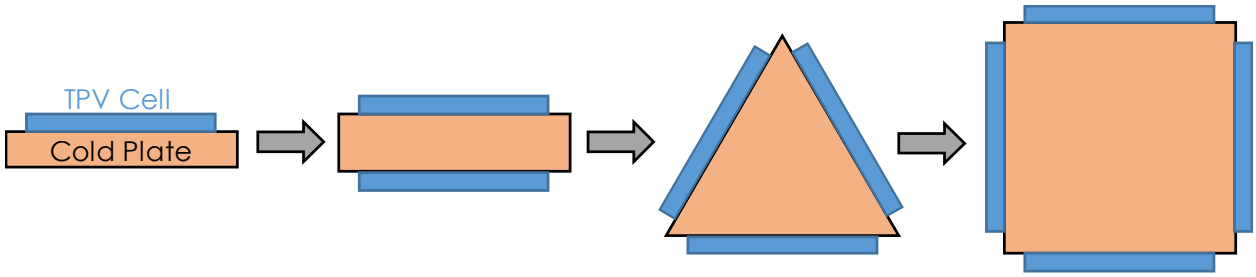

Figure 60 – Geometric configurations ranging from flat plates to the selected square cross section.

A square geometry has certain advantages, such as minimized inactive area, but introduces challenges trying to incorporate existing, proven cooling systems. Microchannel heat sinks are often used for processor cooling in electronics, but are typically designed to cool only one surface of the cold plate and often have significant inactive area [38]. Adapting a microchannel heat sink for a square cross section, instead of the flat plates of their typical configuration, was deemed too challenging and expensive for either a laboratory scale system or an industrial scale implementation. Figure 61 shows one such microchannel cold plate, with significant inactive area. Additionally, the extremely high cooling fluxes

achievable with microchannel heat sinks (>500 W/cm^2) would be useful, but not critical for the cell cooling load (~50 W/cm^2). The high cooling fluxes would be helpful for unprotected and absorbing cold plate area, which as previously mentioned is a serious problem, but those areas would likely not be the well cooled region of the microchannel heat sink, negating any advantages.

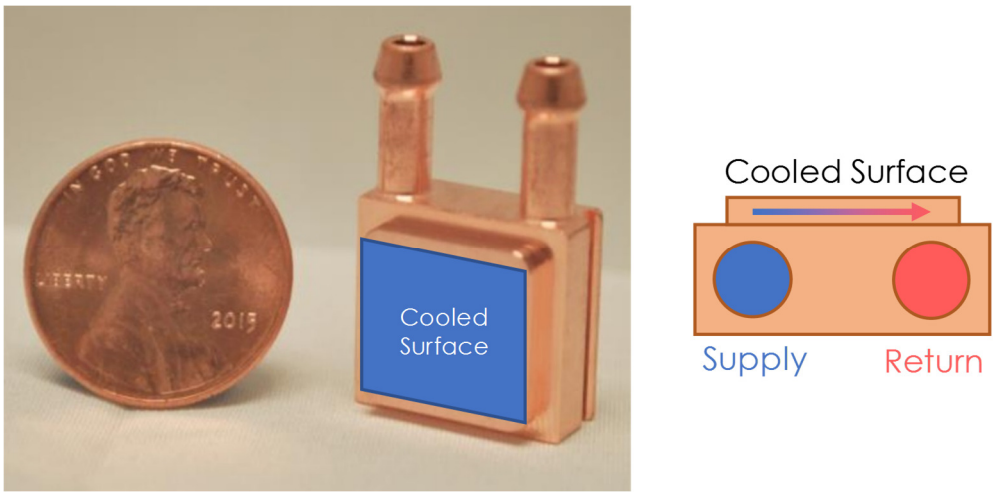

Figure 61 – Cooling system options including a Mikros M2 cold plate. Microchannel cold plates have excellent cooling performance, but typically only on one of their many surfaces [38]

4.2.2. Scalability

The design space for coolant channels is significantly more open when moving from microchannels to milli-channels (mm scale) or larger. The scalability requirement for the cold plate, however, further restricts the options for coolant channel routing. Figure 62 shows the two scales considered for this design problem, an industrial scale system with nominal dimensions for the full scale TEGS system described in Section 1.3.1, and a lab scale iteration for proof-of-concept testing. Ideally the cooling system would work for both of these applications, to prevent the need for a redesign. The laboratory scale dimensions were determined based on TPV cell availability (e.g., 1-4 cm^2 cells) and practical constraints on fabrication (not too small).

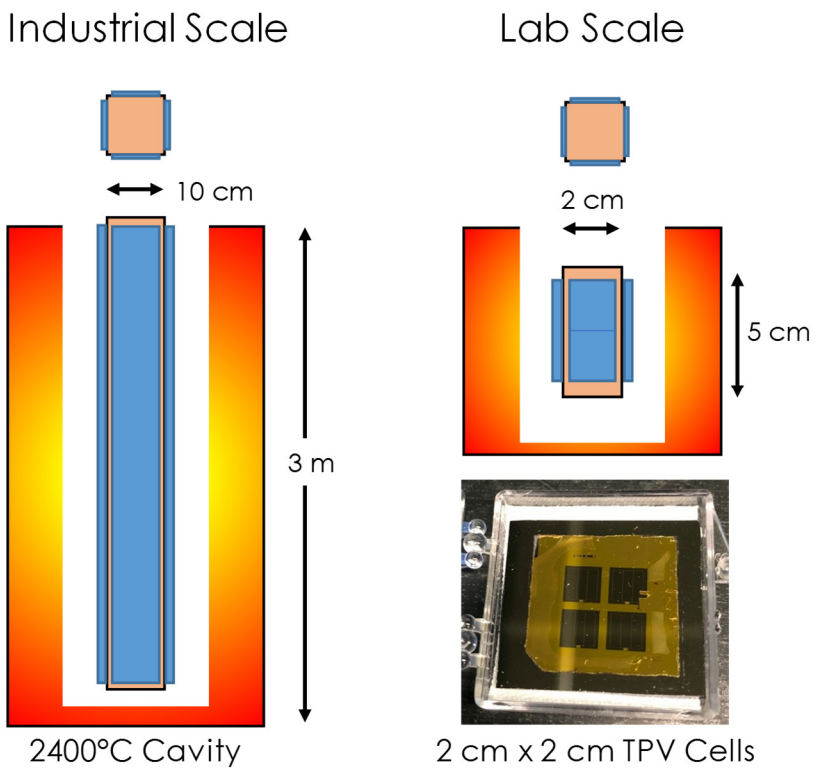

Figure 62 – Industrial and lab-scale systems for the cold plate design. Lab scale is determined by the available sizes of TPV cells, along with practical constraints on fabrication.

An axial flow configuration, illustrated in Figure 63, allows for a length-independent cooling system with minimal sealing faces. Coolant can be supplied through the center of the square cold plate, and returned through millimeter scale channels just under the cells. The main core of the cold plate could be manufactured economically at scale with an extrusion process, without any significant constraints on length. At the lab scale, the 2D cross section is easy to manufacture using traditional machining techniques. Additionally, the "out and back" flow routing allows for all the flow reversal to take place in an end cap, which can be brazed or welded onto the end of the extrusion. Resulting in a single sealing face for the entire cold plate, further simplifying and reducing the cost of manufacturing.

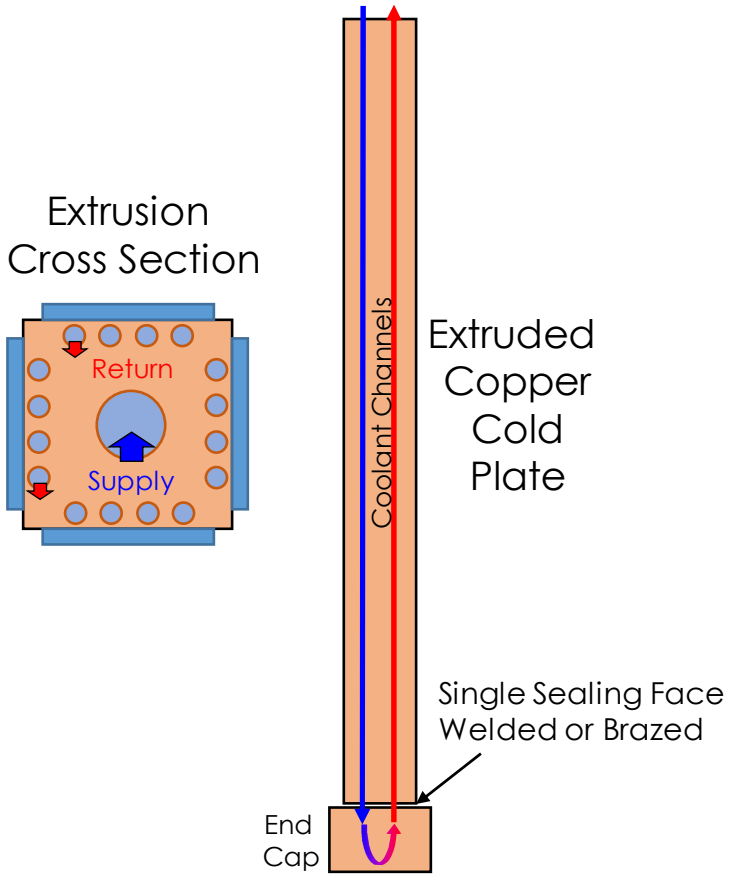

Figure 63 – Axial flow configuration with a 2D cross section extruded cold plate core and flow reversing cap

4.3. GAS DELIVERY

Designing a cold plate for cooling is a relatively straightforward task, but the simultaneous integration of the SNGC makes it a more complex challenge. This section addresses fundamentally how to ensure jet velocity uniformity at several scales, flow routing issues, and gas cooling.

4.3.1. Flow Uniformity

The low-temperature proxy experiments described in Section 3.6 highlighted how challenging it could be to ensure uniform jet velocities for the SNGC. One might try and simplify this problem with a similar out and back approach used for cooling and described in Section 4.2.2. Ensuring uniformity across a smaller cross section would be a simpler task. Figure 64(a) illustrates this idea, and also how a transition from laminar to turbulent flow could disrupt the flow or cause layer separation. Additionally, as the jet

velocity dissipates along the length of the cold plate, the effectiveness of the protecting gas layer will be reduced. While flowing out and back could work for the lab-scale demonstration, a scalable system able to be adapted to a 3-meter-long version would have serious issues. Flowing laterally, shown in Figure 64(b), however, has no such fundamental limitations. For this reason, configuration (b) was chosen to ensure scalability of the cold plate design.

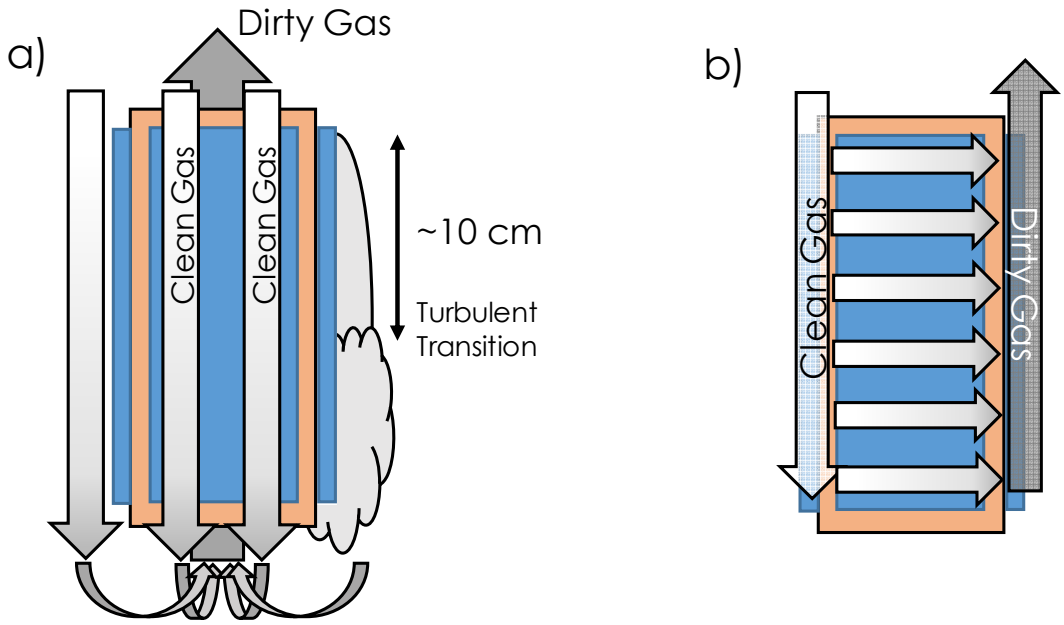

Figure 64 – Axial flow configuration (a) does not work for gas, unconstrained flow path has length limitations. Lateral flow path (b) is length independent.

The lateral flow configuration does not have the same laminar-turbulent transition issues as an axial design, but has its own share of challenges. As mentioned in Section 3.6, ensuring uniform flow with a gas inlet stream perpendicular to the outlet jet can be an issue. Figure 65 shows three cases for a gas nozzle design for the chosen lateral flow configuration. Case (a), with an open slot, does not restrict the axial velocity component of the incoming gas and results in a highly non-uniform jet. This phenomenon was also identified in Section 3.6. Case (b) shows another interesting finding, where if pressure P_2 is greater than inlet pressure P_1, for example due to a stagnation point caused by the momentum of the incoming gas, the lateral velocities along the length of the jet can also be different. This problem can be solved by drastically increasing the pressure drop through the nozzle openings. If pressure drop P_2-P_3 is high, the pressure difference between P_1 and P_2 can be ignored. This principle is used moving forward, requiring small nozzle openings relative to the manifold cross section.

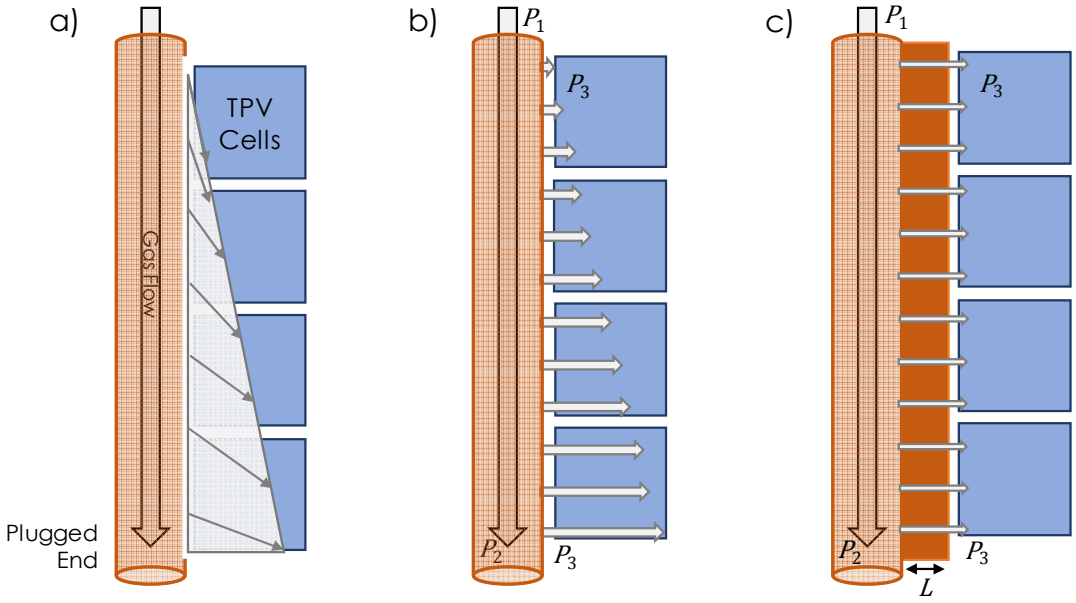

Figure 65 – Gas manifold design configurations to ensure jet velocity uniformity

4.3.2. Flow Routing

Adapting the flow configuration from the prior section to a square cold plate could be very simple. Figure 66(a) shows what may be the simplest iteration of this concept, just putting the gas lines directly on the corners. Clean gas flows to the cold plate and gas dirty with sublimated emitter material is extracted from the opposite corners. Holes could be made in the gas lines at regular intervals, using the prior findings to guide the hole size and placement to ensure uniformity. However, this configuration adds significant inactive area outside the SNGC protected zone with a rather long path to any cooled surface. Moving the gas lines into the cold plate addresses the inactive area overheating problem, and also provides more flexibility in the hole sizes and locations. By introducing an additional flow control component in the form of the jet direction covers, which divert the gas flow 135°, any non-uniformity caused by individual jets can be smoothed out. This approach, however, risks interfering with the coolant channels that take up significant space within the cold plate core. Configuration (c) combines the two clean and two dirty gas lines to just one of each, further reducing the internal volume required for gas delivery.

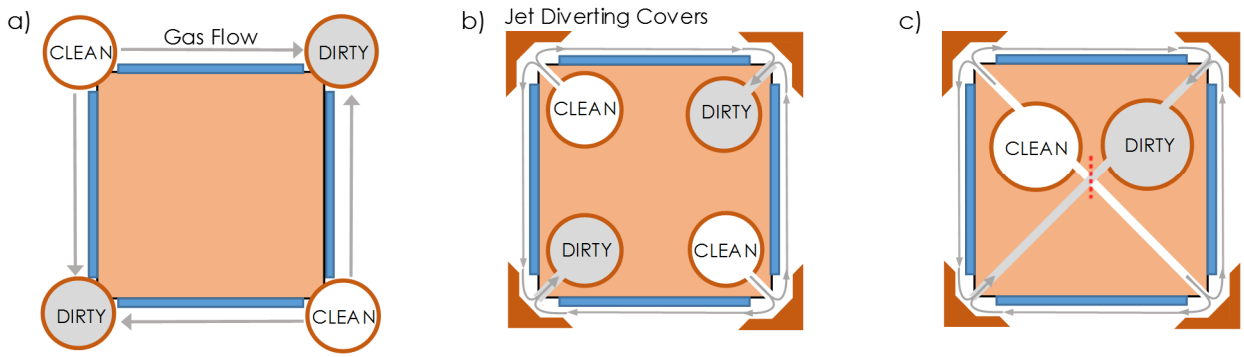

Figure 66 – a) Gas flow along edges is the simplest approach, gas gets hot. b) Moving gas lines into the cold plate resolves cooling issues. c) combining clean and dirty gas lines simplifies integration with coolant.

This reduction in gas channels comes at a cost, with the intersection of the clean and dirty flow paths to the lower two corners. This problem was helped by using many discrete nozzles to ensure uniformity, which in turn could help with the distribution as well. Figure 67 shows how alternating clean and dirty pathways along the length of the cold plate allows for crossing without intersection. Since the nozzles are discrete anyway, this could be done with little to no impact on SNGC performance.

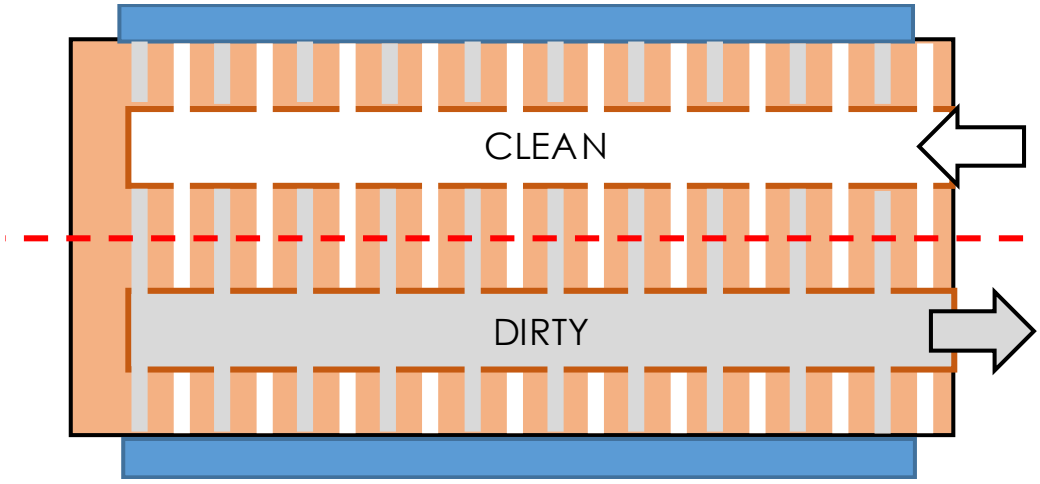

Figure 67 – Gas line intersection solution. Alternating paths for clean and dirty gas.

4.3.3. Gas Cooling

Incorporating the gas lines into the cold plate helps reduce the temperature of the sweeping gas once it has arrived at the cold plate, but what if the gas arrives hot already? To maintain an emitter cavity temperature over 2000°C, a significant amount of insulation is required, particularly if only the relatively high thermal conductivity graphite insulation is used. In the experimental iteration described in the following section, the cold plate and associated plumbing has to pass through about 25 cm of insulation before reaching the hot cavity. Figure 68 illustrates this concept, along with a simple heat transfer model predicting temperature rise in the gas lines. The model compares gas lines of varying diameters, with a constant gas flow rate of 40 LPM (based on 2 m/s average SNGC flow velocity). Also plotted on is the pressure drop, with only tube inner diameters of 6 mm or greater really practical. For a 6 mm tube, the temperature rise could >100°C, immediately overheating the cells which must be kept below 50°C. Therefore, some form of gas cooling or shielding is required.

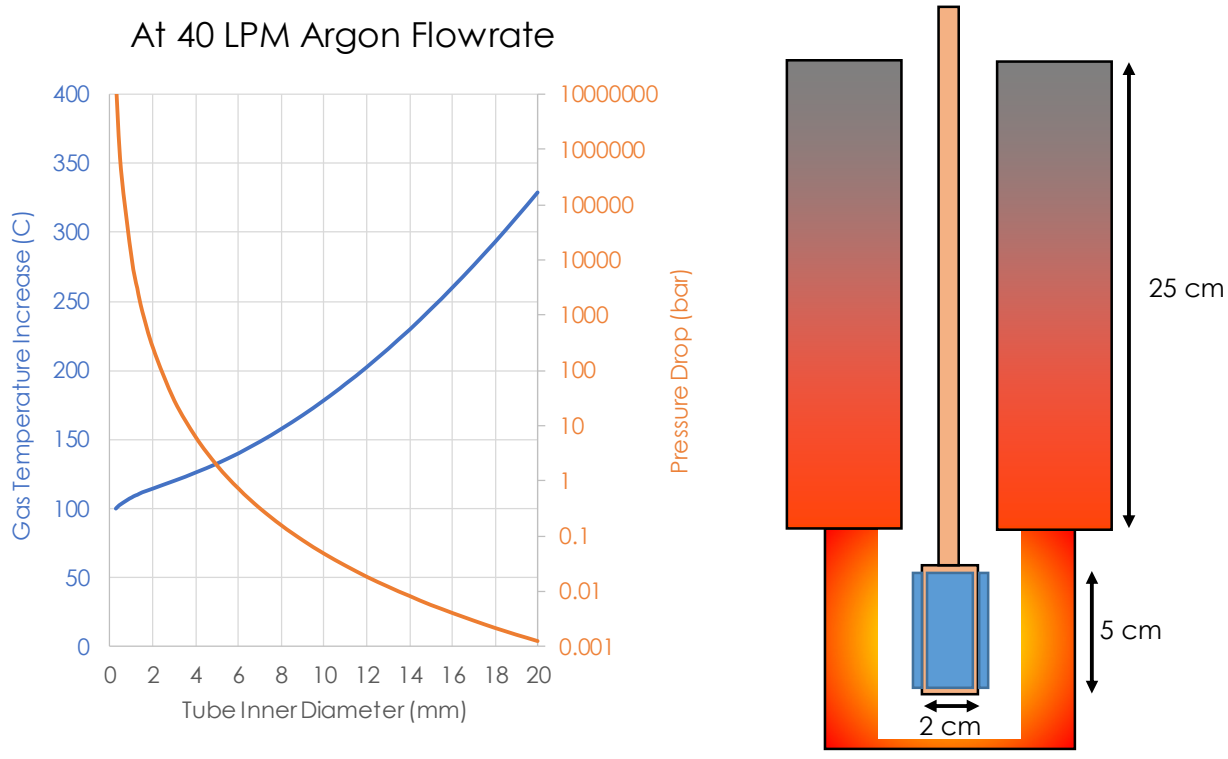

Figure 68 – Gas heats up passing through the insulation, even at small tube diameters

There are several options for keeping the sweeping gas from heating, as it travels through the insulation. Figure 69 shows a number of these, including a layer of insulation, radiation shields and active

cooling. Insulation may seem like the simplest, but since the outer layer of insulation is not directly cooled, only high-temperature insulation materials can be used. Using a thin graphite insulation layer would work, but the graphite insulation is highly optically absorbing, so may end up making the problem worse. Copper reflects about 95% of the cavity spectrum, while the graphite insulation would absorb almost all of it.

A better option for insulating in these high irradiance conditions would be radiation shields. By adding multiple layers of an optically reflective material, a majority of the heat could be shielded from the gas. For example, copper reflects 95% of the incident light, but what if there were two layers of copper with a gap between them? Similar problems to the insulation case present themselves, with the outer shield getting hot due to lack of active cooling. Additionally. The shields would need to be held somehow, contacting either the cold plate or gas lines, again defeating the purpose of the shielding in the first place.

The final, and best method identified for keeping the gas lines cool is flowing a layer of cold water over the surface. This is by far the most complex in terms of integration, but has highest likelihood of success for a high-temperature test.

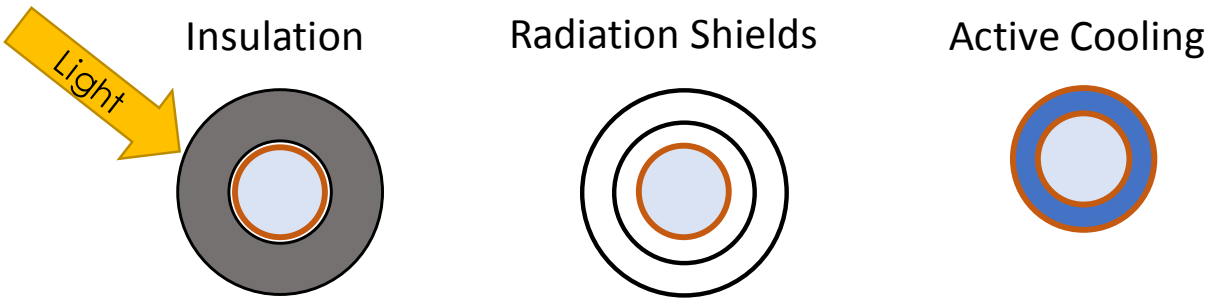

Figure 69 – Gas line cooling options

4.4. INTEGRATION AND FABRICATION

In this section so far, several cold-plate subcomponents have been designed, but not combined together. The coolant and gas have their flow pathways identified, but integrating them into a single device proved the most challenging task yet. The rest of this chapter shows the various approaches considered for combining, sealing and fabricating the complete SNGC-TPV device.

4.4.1. Combining Gas Delivery and Cell Cooling

The simplest way to add liquid cooling to the gas lines was to embed them into the existing coolant pathway. Combining both lines in the coolant return would ensure cold gas without heating the coolant prematurely. Figure 70 shows how this works, with a larger coolant return tube enabling both gas lines to be fully submerged.

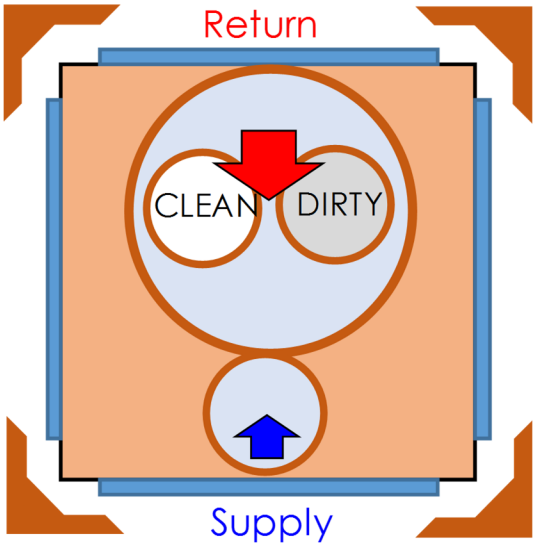

Figure 70 – Gas lines incorporated into coolant lines.

The gas lines could then be extracted from the coolant later on, outside of the hot region of the experiment with a polymer sealed bulkhead. Figure 71 shows this extraction component, with the combined coolant and gas tubes entering one side, and the coolant exiting the top while the gas lines continue through. A custom silicon gasket and sealing plate was used to ensure no coolant leaks in the experimental chamber.

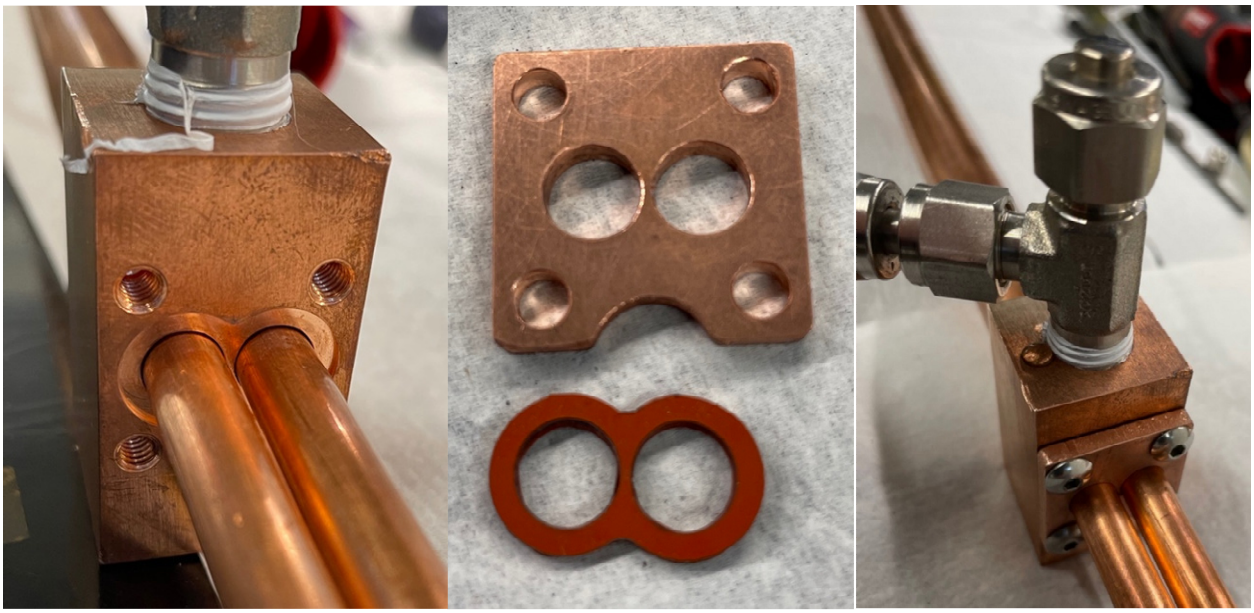

Figure 71 – Gas lines extraction block and gasket.

Figure 72 shows the complete cold plate design, with integrated cooling and gas delivery. Gas directing covers are screwed on to the cold plate core, to ensure good thermal contact between the covers and the actively cooled part of the cold plate. These covers are replaceable to allow for different jet thicknesses, and the brass screws have high thermal conductivity, preventing the covers from overheating. A majority of the inactive area of this design is on the ends, where there is significant cooling from the internal water channels. Wiring for the cells can also be run through the gas lines, to protect the wires from thermal damage.

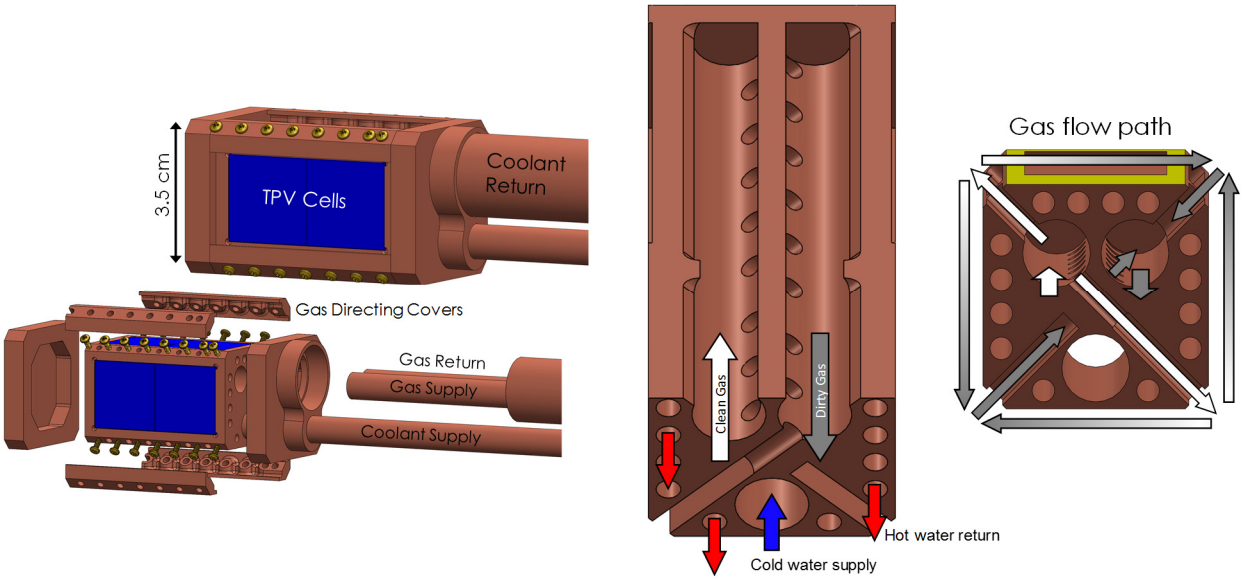

Figure 72 – Final design CAD model including exploded view (left), and gas and coolant flow paths (right).

A slightly simplified version of this design was evaluated in COMSOL to ensure no part of the system was at a risk of overheating. Figure 73 shows the results of this analysis, indicating that under normal operating conditions at 2150°C, the system would have no problem keeping cells cool. Additionally, even if all the surfaces became coated in something (e.g. highly absorbing carbon), the copper would not overheat or run the risk of melting.

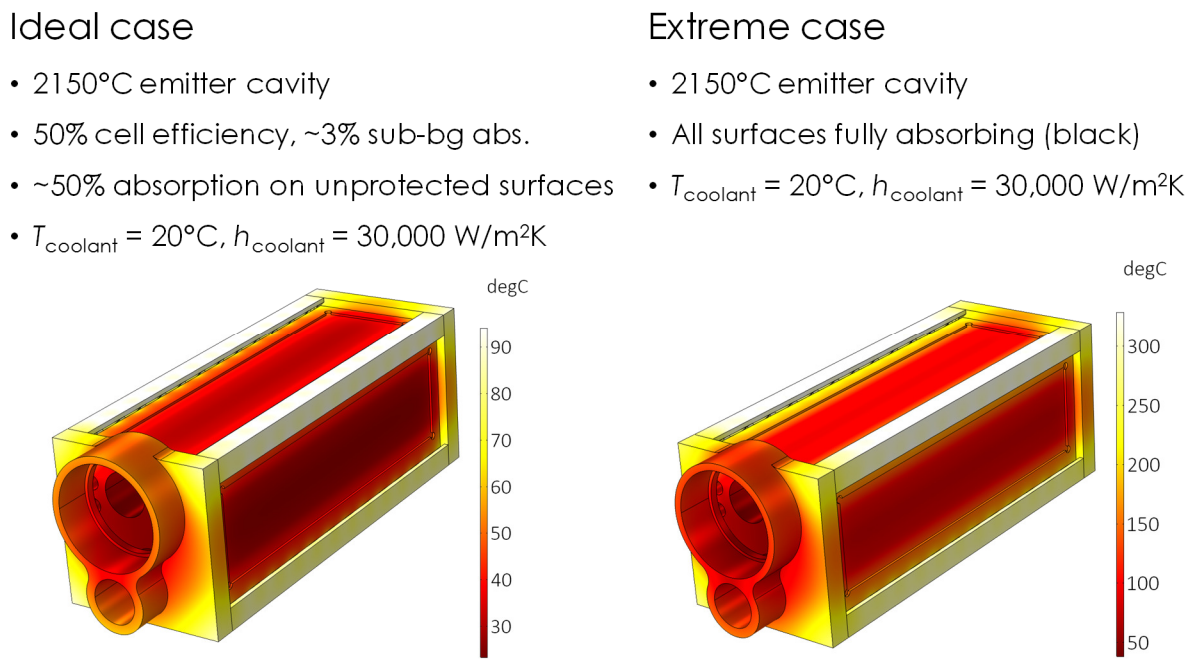

Figure 73 – COMSOL thermal model showing cooling effectiveness for the ideal operating conditions (left), and a failure condition where all the surfaces turn black (right). Even with black surfaces, no part of the system exceeds the melting temperature of copper (1085°C).

4.4.2. Sealing and Fabrication

After the full design process and thermal modelling in the previous section, the experimental SNGC-TPV device was fabricated and tested. All the cold plate components were machined from copper, taking advantage of both its very high thermal conductivity (~300 W/m-K) and optical reflectivity (>95% reflective). This was an ideal combination of properties for a cold plate experience such a extreme environment. The parts were welded together, shown in Figure 74, by a professional welder at the MIT Central Machine Shop. However, upon fabrication, there were several tiny leaks throughout the welds, leaking water which would damage the experimental system. These leaks were sealed using a radiator sealant designed for car coolant systems (K-Seal), it was dissolved in water and pumped at 50 PSI (3.5 bar) through the cold plate. This approach stopped all visible leaks, but there was still concern the sealant may not hold for repeated testing.

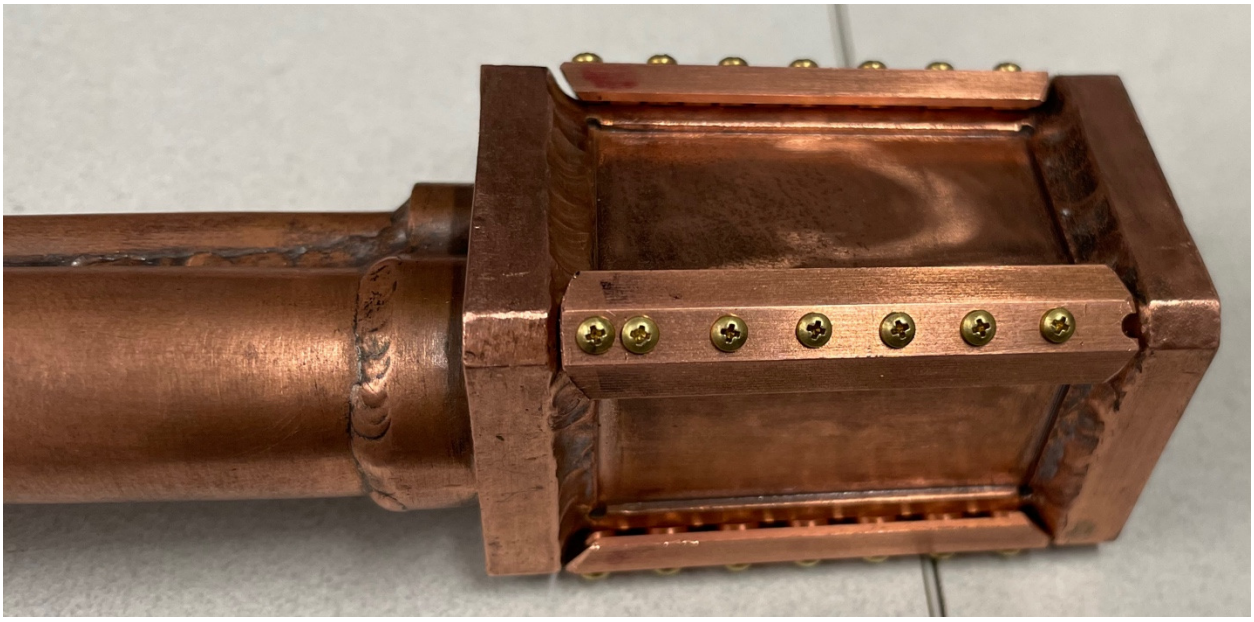

Figure 74 – Initial welded assembly including screwed on jet-directing covers.

After the sealing challenges with the welded approach, the device was redesigned to incorporate thin PTFE gaskets. The relatively small exposed area of gasket was determined to be small enough to prevent the gasket from overheating. Stainless steel screws were used to attach the caps and core together, as their higher strength was considered helpful in keeping pressure on the gasket. Additionally, plumbing connections were brazed with high-temperature braze to insure both a water tight connection, and temperature resistance. As the brazed connections were in very close proximity to the coolant, overheating concerns were not as pronounced as the cap seals.

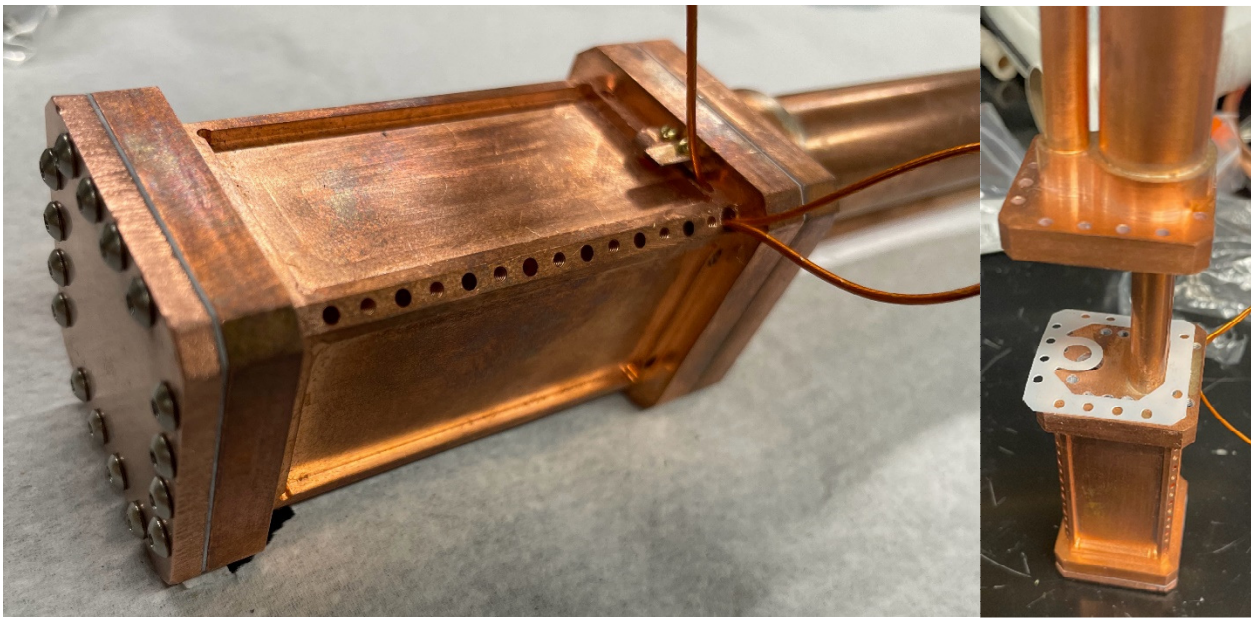

Figure 75 – Sealing using gaskets. Jet directing covers are removed, showing the exit holes for the sweeping gas and the threaded holes for the brass screws. Also shown is the electrical wiring and connections for a TPV cell, running through the gas line.

Upon testing, the gaskets were unable to withstand the high intensity thermal radiation of the emitter cavity, and melted to the point of failure in less than 5 seconds. Figure 76 shows some of the damage caused by the overheating, including deposition of evaporated PTFE and tungsten-oxide from the water leaking onto the hot tungsten liner. The stainless-steel screws may have partially contributed to the failure, as they are more optically absorbing and less thermally conducting than the brass ones.

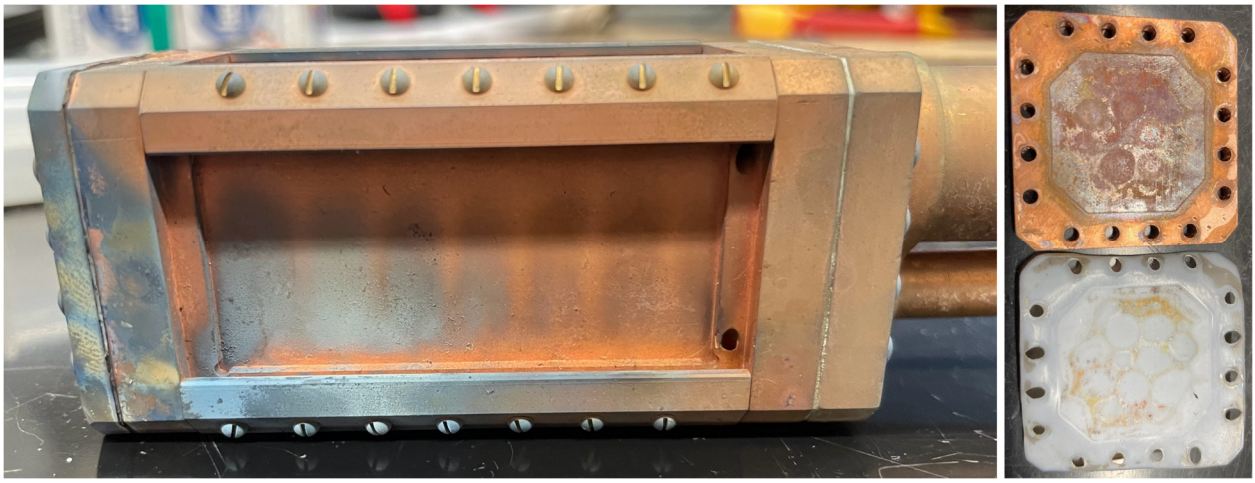

Figure 76 – Gaskets catastrophically failing to seal the modified device

After the gasket failure, welding was revisited due to the challenges with the thermal conductivity and temperature resistance of the gasket, shown in Figure 77. The bolt holes and gasketed seams were welded closed and the inevitable small leaks were sealed with solder. Vacuum was applied to the interior of the cold plate, the whole device was heated to the melting point of plumbing solder, and solder beads were applied to all the leaking locations (black circles in the middle image). This approach worked very well, resulting in completely sealed device capable of withstanding the hot emitter cavity. Even after several iterations, no melting or deformation of the solder was observed, likely due to the high thermal conductivity of the copper substrate.

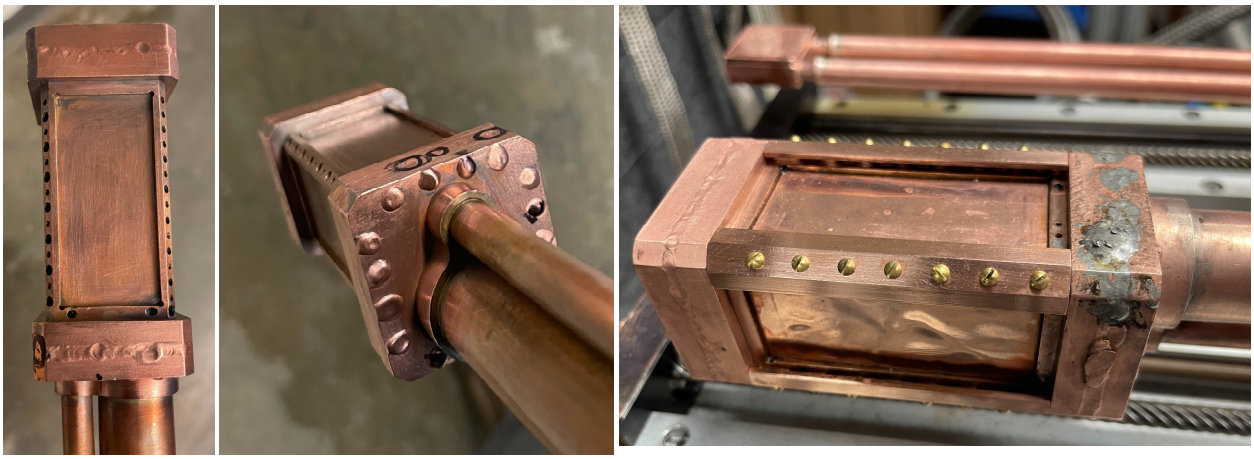

Figure 77 – Final sealing approach combining welded seams and solder to seal any leaks

4.4.1. Completed Device and Installation

The completed device was mounted on a linear actuator capable of remotely actuating the device into the emitter cavity, shown in Figure 78. The actuator was capable of full insertion (~45 cm) in 5-10 seconds. Measurements of the inlet and outlet coolant temperature were recorded to ensure any drastic changed in thermal behavior were detected.

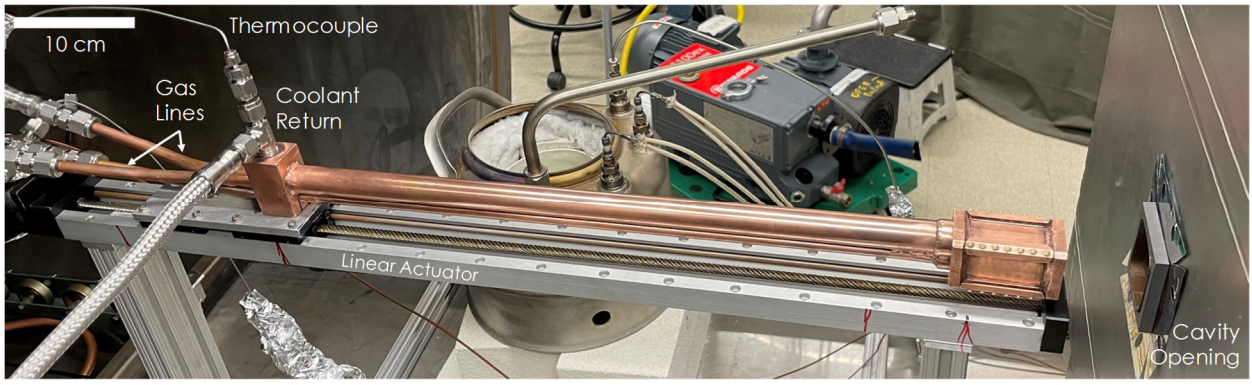

Figure 78 – Complete SNGC-TPV device mounted on linear actuator

4.5. SUMMARY

This chapter presents the SNGC integrated cold plate design developed to provide both cooling and sweeping gas to a TPV cell module. Also shown are some geometric challenges with integrating these components in a small, compact package, and also the fabrication challenges with sealing copper in such an extreme thermal environment. Finally, the completed and fabricated cold plate ready for testing at high-temperatures is presented. The next chapter further discusses the experimental apparatus and procedure used for this testing, as well as the results of the tests.

Chapter 5

5. SNGC and TPV System Testing

The final state of the investigation was testing the carefully design emitter and cold-plate assemblies. As alluded to in previous sections, a high-temperature testing apparatus capable of heating the emitter cavity to above 2000°C was developed in parallel to these subcomponents. This chapter reviews the high-temperature apparatus, as well as a selection of the testing that was performed on the complete assembled SNGC-TPV device.

5.1. HIGH TEMPERATURE EXPERIMENTAL APPARATUS

Figure 79 shows the full high-temperature experimental apparatus including the hot-side components (cavity emitter, insulation, heater) and the cold-side components (cold plate, actuator, vacuum chamber). Additional information about some of the challenges addressed with this apparatus are described in Section 2.2.

The vast majority of the high-temperature experiments were done in 0.8 atm of argon, but using a vacuum chamber for containment allowed for quick vacuuming and refilling with gas to both remove oxygen before the experiment, and remove any potentially toxic byproducts afterwards (e.g. carbon monoxide). Water cooled radiators and fans were used to cool the gas environment inside the chamber during operation, as there was a significant amount of heat dissipated during operation (~12 kW). Cooling lines were also wrapped around the chamber, shown in Figure 80, to locally cool the chamber walls.

Initial iterations of the experiment used a hybrid insulation approach with graphite insulation (thermal conductivity $k \approx 1$ W/m-K) in the hottest areas, then an alumina-silicate insulating board ($k \approx 0.1$ W/m-K), and finally a silica-microporous insulation ($k \approx 0.01$ W/m-K) layer on the outside. Due to the contamination and high-temperature stability issues described in Section 2.2, this hybrid insulation approach was later switched to pure graphite insulation. Figure 80 shows the pure graphite insulation block arranged around the tungsten lined cavity.

Heat was supplied to the system with a solid graphite serpentine heater, also shown in Figure 80, with tungsten leads transmitting the electricity through the insulation blocks. A gap of at least 2 cm was left between the leads and insulation to reduce the chance of arcing or shorting. Tungsten was selected for the

leads due to its combination of temperature resistance, and electrical conductivity. Graphite leads would have become the dominant resistance and limited heat delivery to the cavity. Heater power was approximately 12 kW. After removing the more insulating oxide materials, the cavity was only able to reach 2150°C instead of the 2400°C maximum system temperature. However, 2150°C is the average operating point of the TEGS system and was deemed sufficient for this proof of concept.

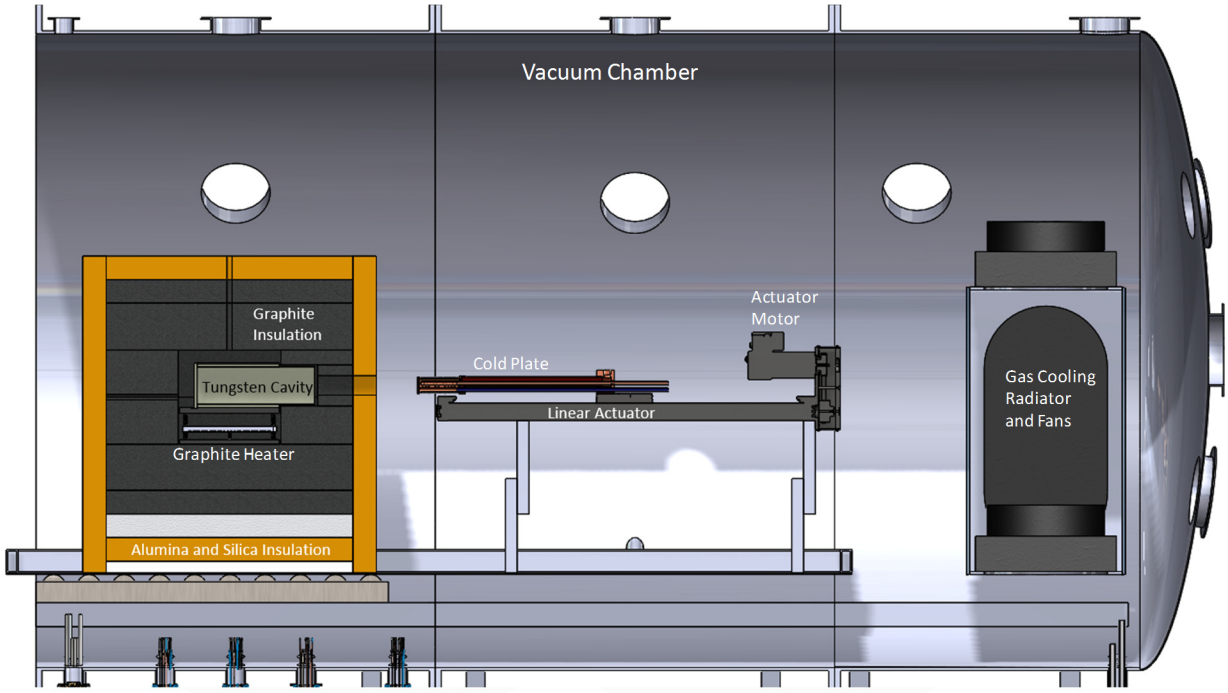

Figure 79 – High temperature testing apparatus including actuator, insulation and heater, vacuum enclosure, and gas cooling units.

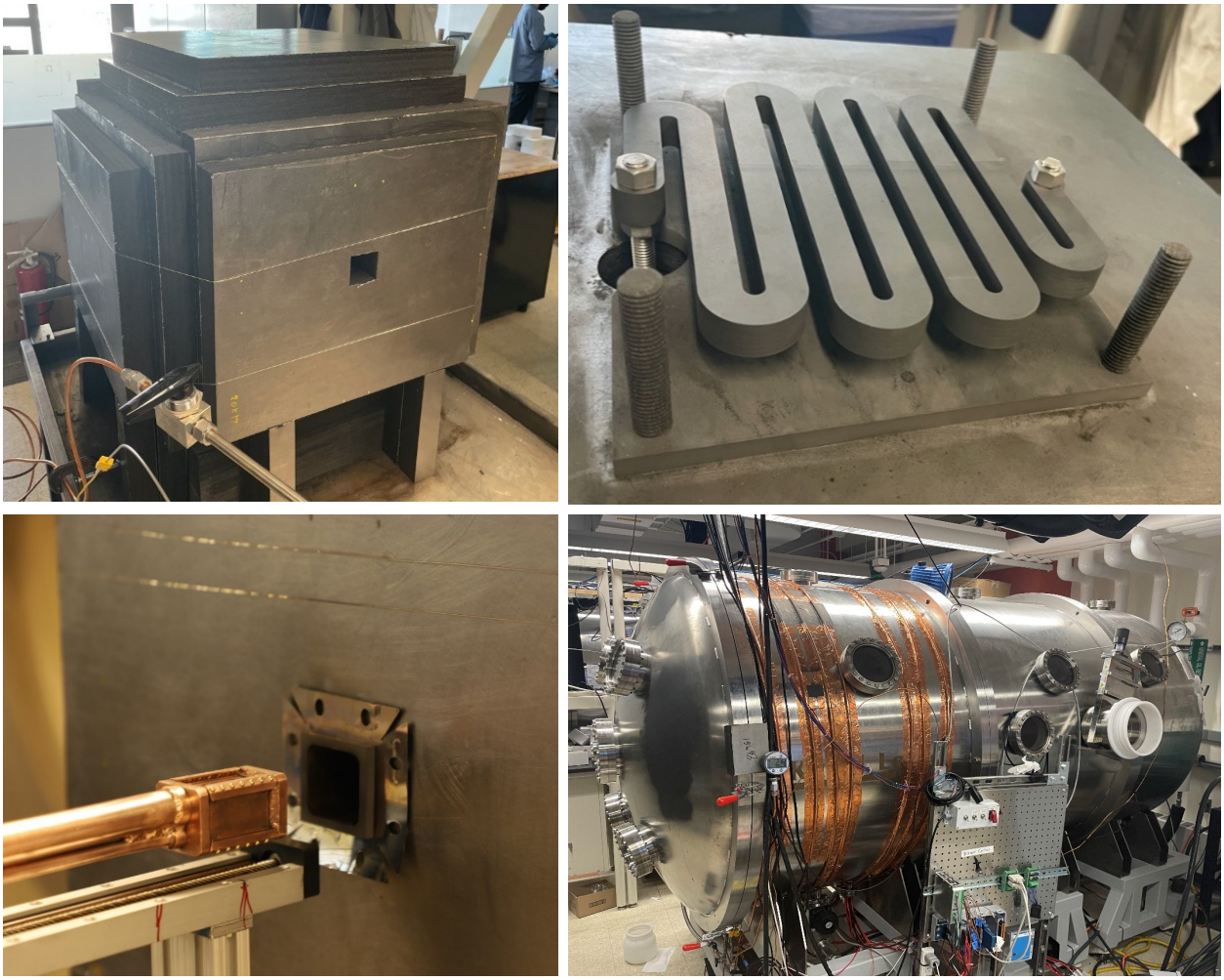

Figure 80 – High temperature testing apparatus images including all graphite insulation block (top left), graphite heating element (top right), cold plate ready for insertion in to the tungsten lined cavity (bottom left), and the vacuum chamber used for testing (bottom right).

Figure 81 shows an example test run at 2150°C, before and after the cold plate is inserted. The bright light emitting from the cavity is an example of the high-intensity environment the cold-plate is designed to operate in.

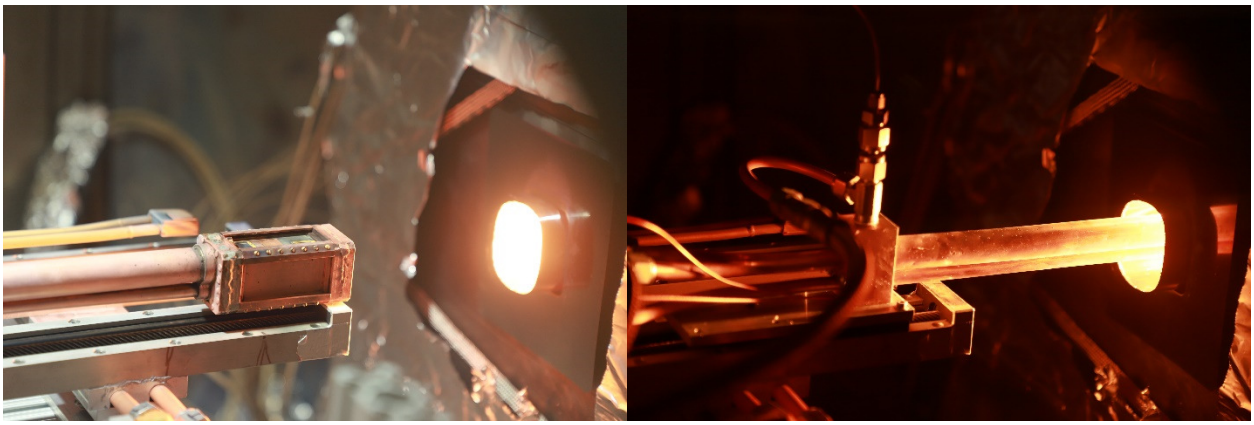

Figure 81 – Test operating at 2150°C before and during insertion

Further modifications to the apparatus throughout the testing process included the addition of a secondary, smaller cold plate and a more complex actuator set-up that allowed for switching between cold plates remotely, shown in Figure 82. Initially, the small cold plate was introduced as a sacrificial "cold-finger" to condense any evaporated contaminants from the cavity before insertion of the larger, SGNC integrated system. The hypothesis was that the cavity environment could become fully saturated with contaminants over the long (>5 hours) heat up procedure, causing increased deposition that was not representative of the steady-state sublimation rate. This ended up not being the dominant deposition mechanism, but in future testing this smaller cold plate provided a good baseline measurement for deposition rate without the protective sweeping gas layer.

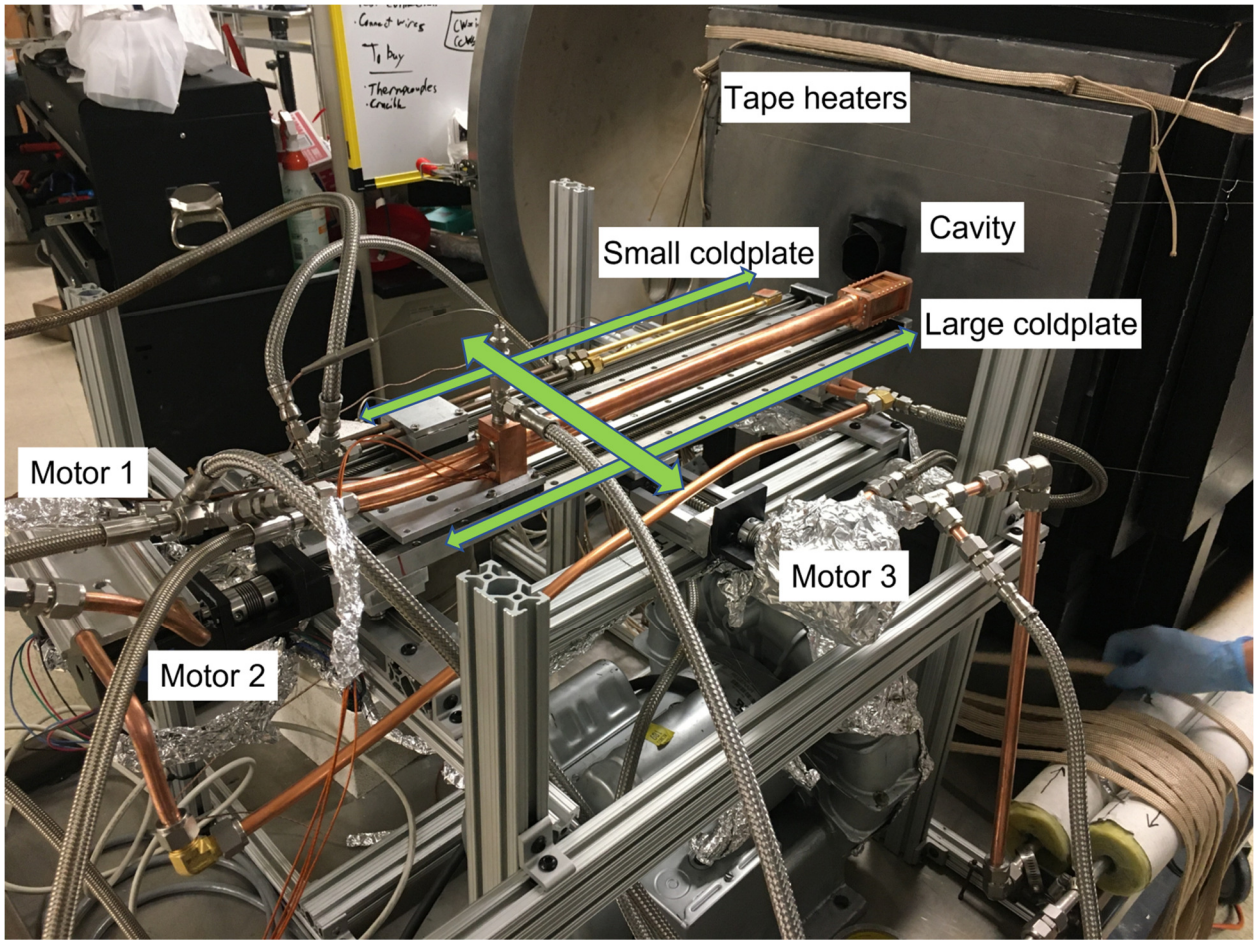

Figure 82 – Testing apparatus actuators and dual cold plates. Green arrows show direction of actuation for the cold place actuators, and switching actuator.

5.2. PRELIMINARY RESULTS

Initial high-temperature experiments were plagued with system contamination issues, resulting in significant deposition rates of various species. Figure 83 shows the results of some of these early tests, which showed what was believed to be non-carbon deposition. The composition of this contamination was evaluated via SEM, shown in Figure 84, and was eventually suspected determined to be primarily due to impurities in the graphite insulation. The layer of deposition was quite thick, ~60 μm, compared to the expected deposition on the order of 0.1-10 nm.

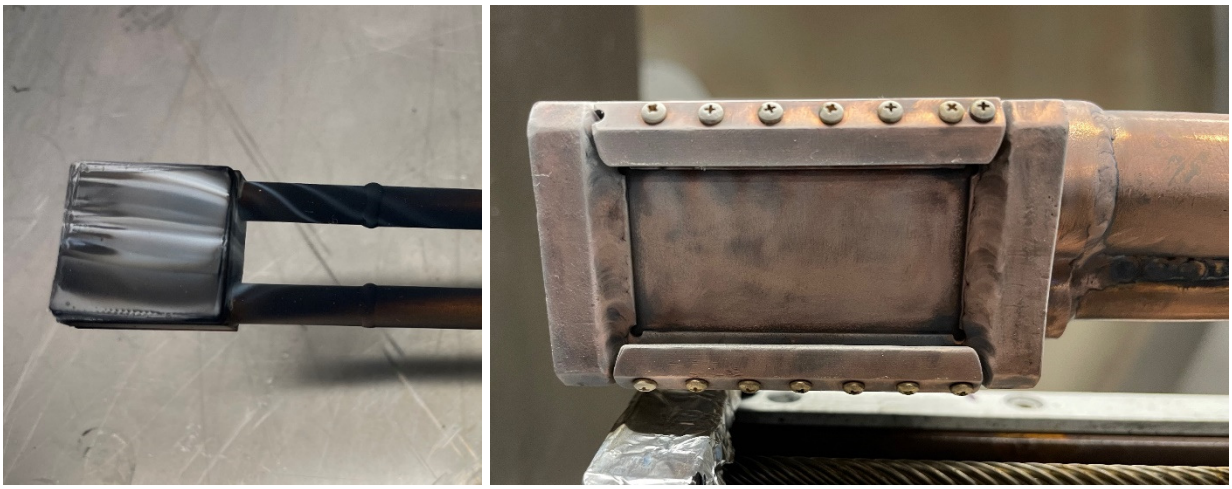

Figure 83 – Insulation contamination causing accelerated deposition after 1 hour of operation

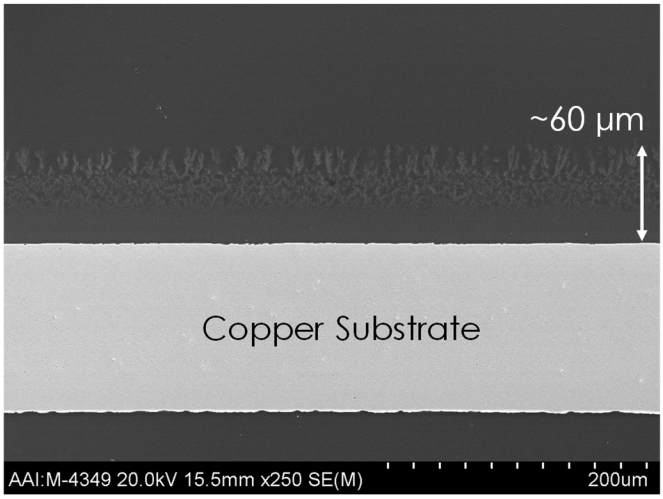

Element Line	Norm. Wt.%	Atom %
C K	4.4	8.8
N K	1.1	1.9
O K	28.6	42.8
Na K	21.0	21.8
Al K	1.1	0.9
Si K	2.8	2.4
P K	9.7	7.5
S K	0.9	0.7
Cl K	0.2	0.1
K K	1.9	1.1
Ca K	4.7	2.8
Cr K	0.2	0.1
Fe K	1.6	0.7
Ni K	0.5	0.2
Cu K	21.2	8.0
Total	100.0	100.0

Figure 84 – Cross-sectional SEM analysis of the deposition layer, showing a relatively thick and dendritic layer of deposited material

Even with the accelerated contaminant deposition, SNGC effectiveness was initially estimated using an infrared camera, shown in Figure 85. These measurements were done ex-situ, before and after a 10-minute experiment in the hot emitter cavity. Coolant of a known temperature was flowed through the cold plate, and the IR camera emittance was tuned so the temperature reading matched before and after. The change in emittance for the SNGC protected and unprotected areas were compared after the experiment and used as a qualitative proxy for measuring deposition. The relative change was used to estimate the SNGC effectiveness, as the main purpose was to prevent any changes in the optical behavior of the TPV

cells. The protected region showed a 50% lower emittance change as compared to the unprotected, suggesting some impact from the SNGC.

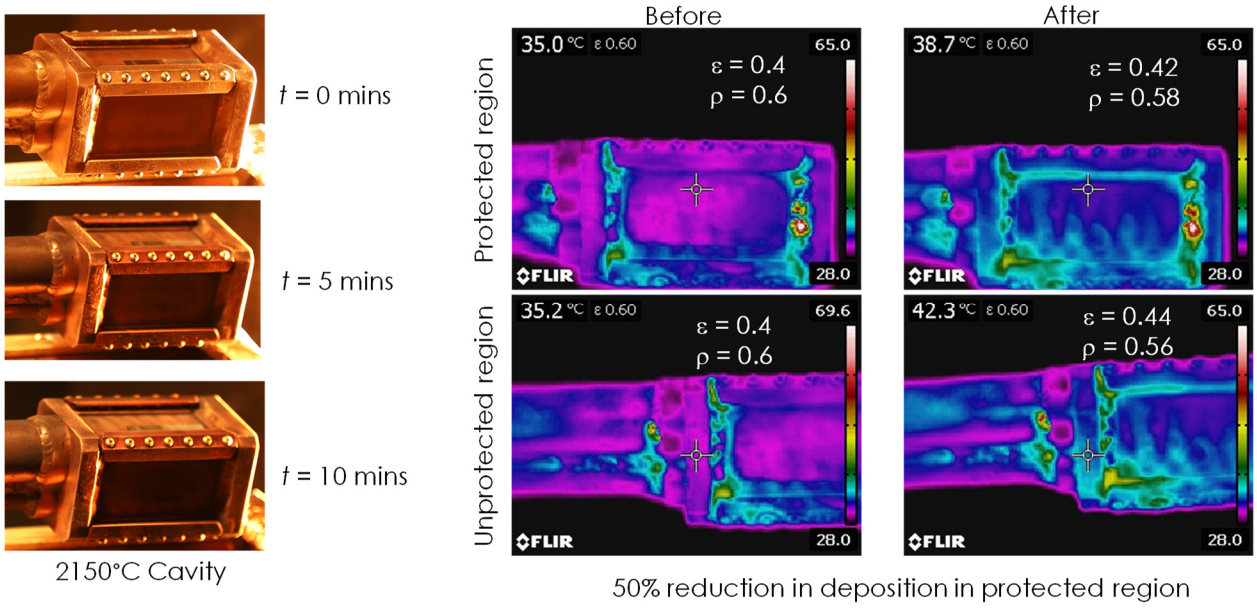

Figure 85 – SNGC effectiveness evaluation using an infrared camera. After 10 minutes in a 2150°C cavity, the relative change in reflectance of the protected and unprotected region suggests a 50% reduction in the effects of deposition

As a final attempt to resolve the insulation contaminant problem, a closed end graphite tube was machined to act as a completely sealed emitter cavity. The hypothesis was that contamination from the insulation was leaking through the very small cracks in the tungsten lined cavity. A closed end tube is not a scalable design, but was used to rule out that deposition mechanism. The tube geometry was not achievable with tungsten, due to the high cost of machining, and is very challenging to add a tungsten liner. In this case, however, the purpose was to eliminate contaminants from the insulation and not prevent carbon deposition. In fact, the higher deposition rate of carbon was useful as a method of accelerating the high-temperature deposition rate and providing stronger indication of SNGC effectiveness. The modified apparatus with the graphite tube emitter is shown in Figure 86.

Figure 86 – Addition of a graphite tube emitter to fully shield from insulation contamination and accelerate measured deposition material.

5.3. NUMERICAL MODELLING

Transitioning to a tube emitter made from graphite prompted a revisit to the deposition COMSOL model. An example of the modeled geometry is shown in Figure 87, with a color map corresponding to concentration and arrows showing velocity streamlines. Graphite was used as an emitter material, with an emitter temperature of 2150°C. Transient simulations were conducted for 5 seconds with the last 1 second of data averaged, as a stable solution was challenging due to natural convection.

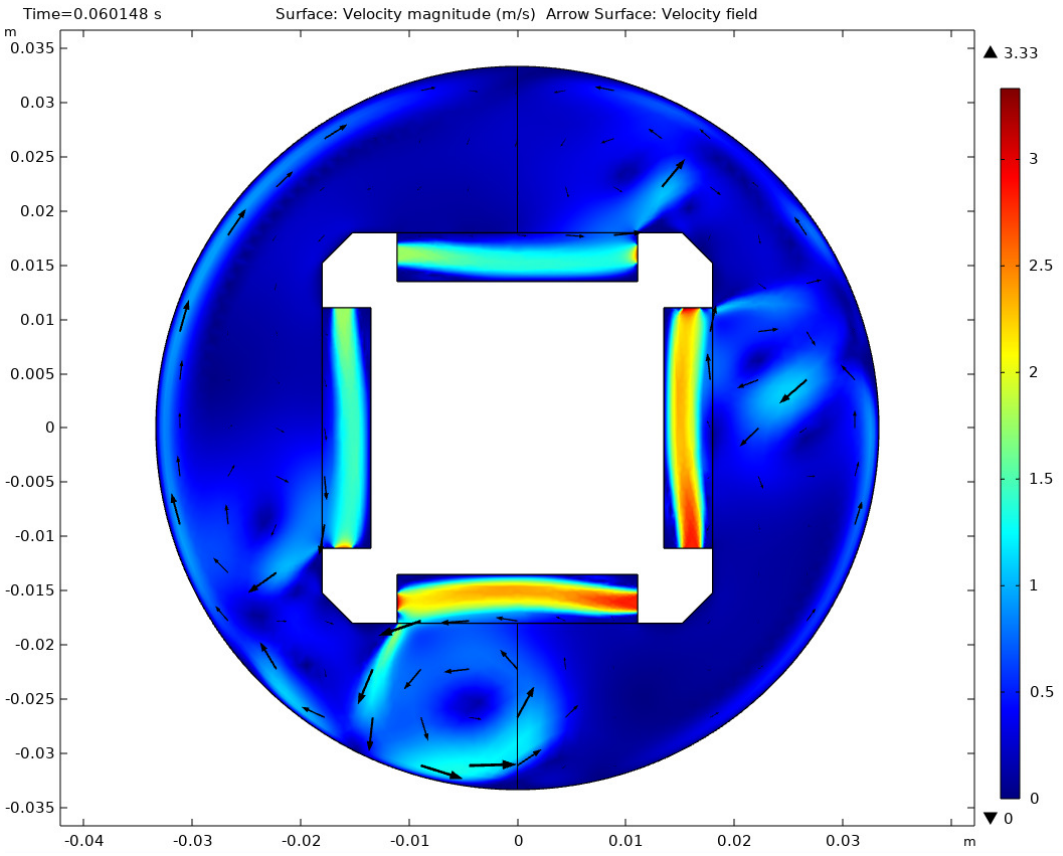

Figure 87 – Modelled concentration profiles, velocity direction and magnitude indicated with arrows

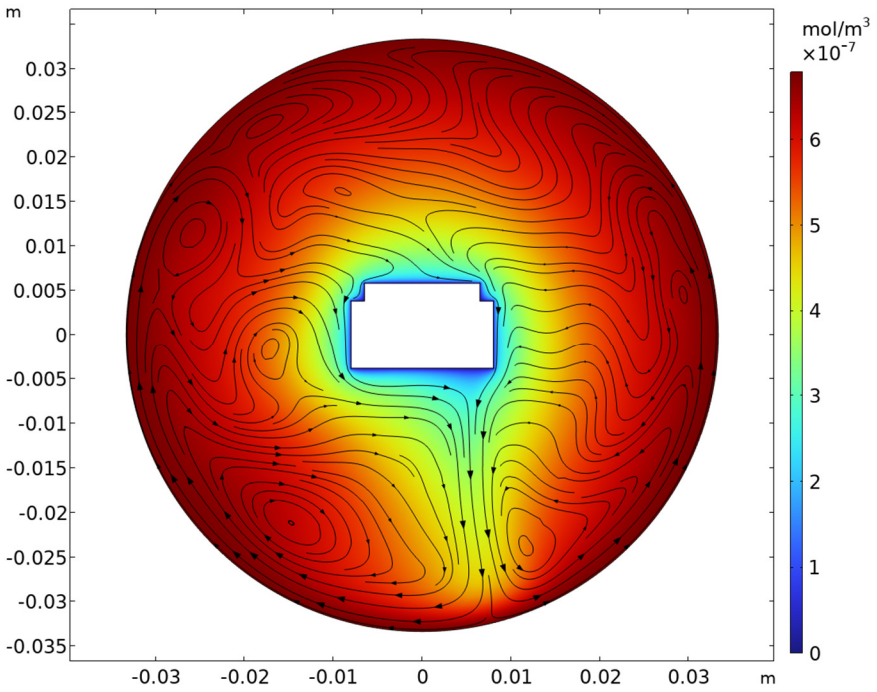

Figure 88 – Modelled concentration profiles, velocity direction and magnitude indicated with arrows for the small cold plate

Results of the updated model are shown in Figure 89, indicating an exponential decrease in deposition rate with increasing gas flow rate. The bottom and right face were highly unstable with deposition rates varying several orders of magnitude between time steps. The plotted data is an average deposition rate over 1 second (0.05 second time steps) with the maximum and minimum deposition values shown in the shaded region. Due to the complexity of the model, convergence for a 3D version of the model was unable to be achieved. A reference case of the small unprotected cold plate in an identical emitter environment is also plotted.

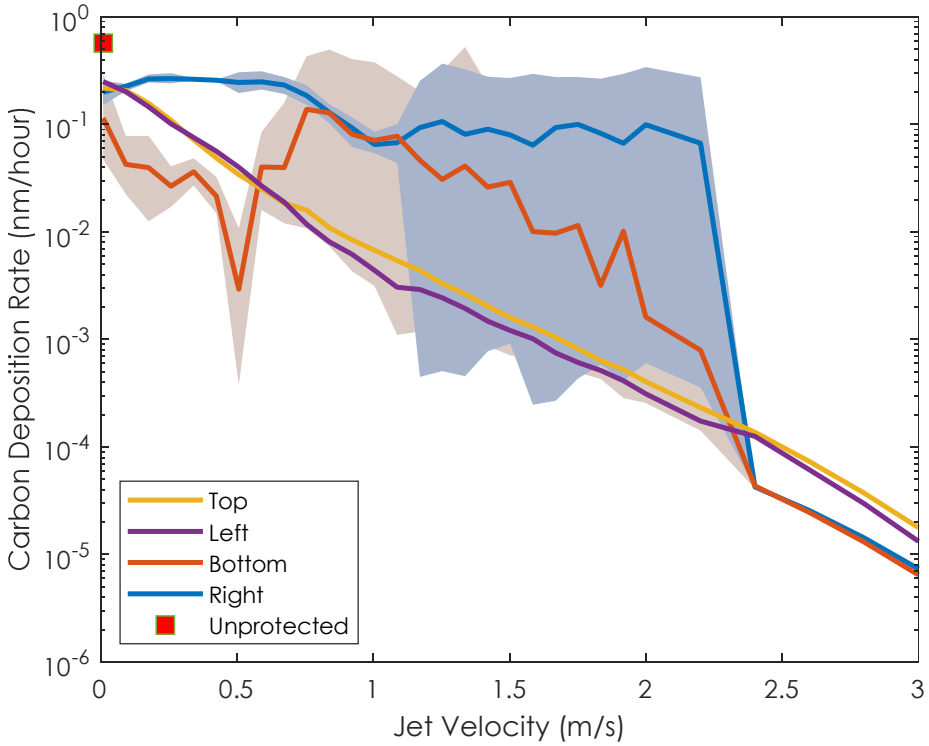

Figure 89 – Deposition profiles of all four sides of the modelled geometry at different average flow velocities. Significant instability was observed on the bottom and right sides, shaded regions represent maximum and minimum solutions.

5.4. IMPROVED HIGH TEMPERATURE SNGC TESTS

The final experiment to investigate the effectiveness of the SNGC included both the large cold plate and small cold plate, with copper foil samples soldered on to each side, shown in Figure 90. Due to the different length paths for the sweeping gas, velocity is expected to be different on the top and left compared to the bottom and right surfaces. The path diameters could be sized to result in identical velocities for a given flow rate, but in this case, it provides a convenient way to test two different gas velocities.

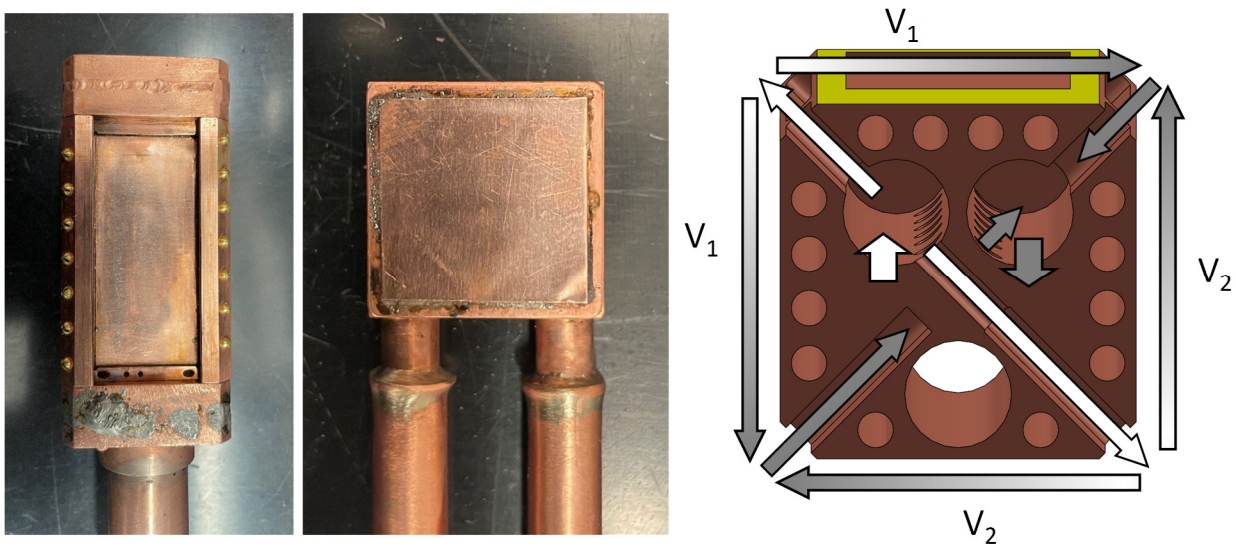

Figure 90 – Copper foil deposition samples soldered to SNGC-TPV device and an unprotected copper microchannel cold plate (left). Schematic of different jet velocities due to varying gas path length, allows for two different velocity points for each experimental run.

The actual gas velocities under the experimental operating condition were measured with a hot-wire anemometer at 0.5 mm increments along the foil samples. Velocity was measured at the inlet (where the jet leaves the jet directing covers), the middle, and the outlet. This measurement approach and apparatus is illustrated in Figure 91. The results of this velocity characterization for the inlet, middle, and outlet are shown in Figure 92, Figure 93, and Figure 94, respectively. These velocities were measured in air, but as the SGNC pump is a positive displacement roots blower, gas density and viscosity should have a little to no effect on flowrate. From the middle velocity profiles, average velocity on the top and left sides was estimated to be 1.75 m/s, while the bottom and right-side average was 2.8 m/s.

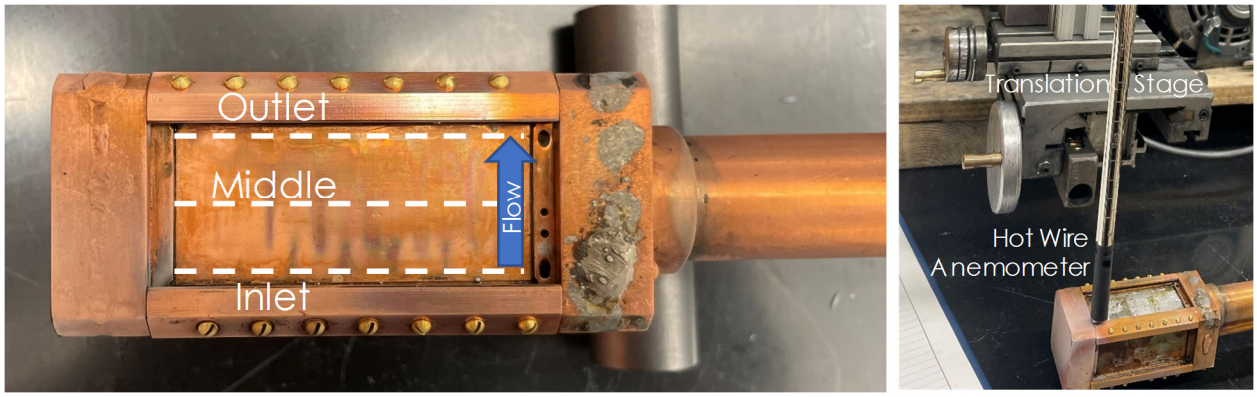

Figure 91 – Velocity measurement locations and apparatus, including a hot wire anemometer and 1-axis translation stage.

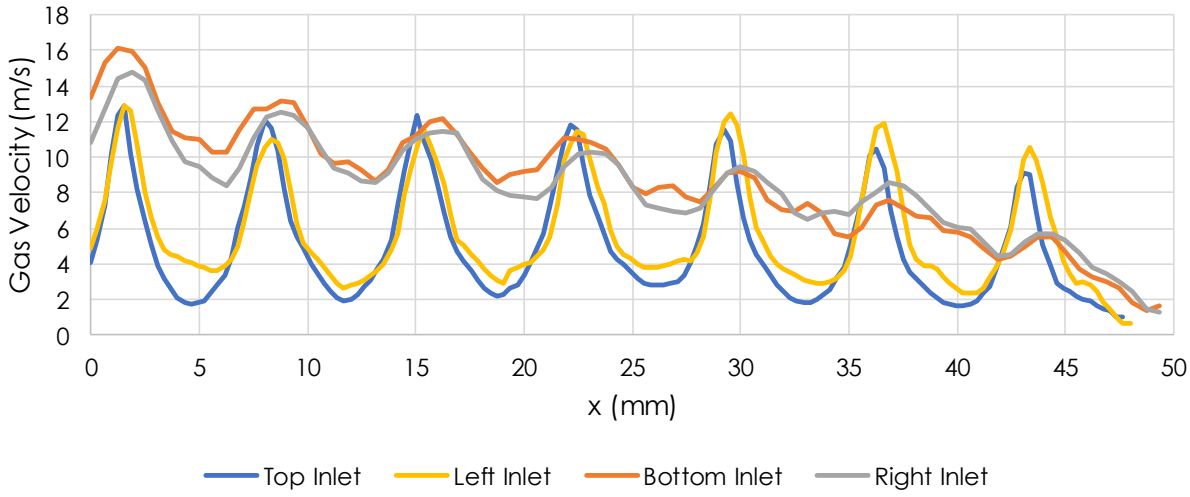

Figure 92 – Velocity profiles measured ex-situ under experimental flow conditions for the jet inlet

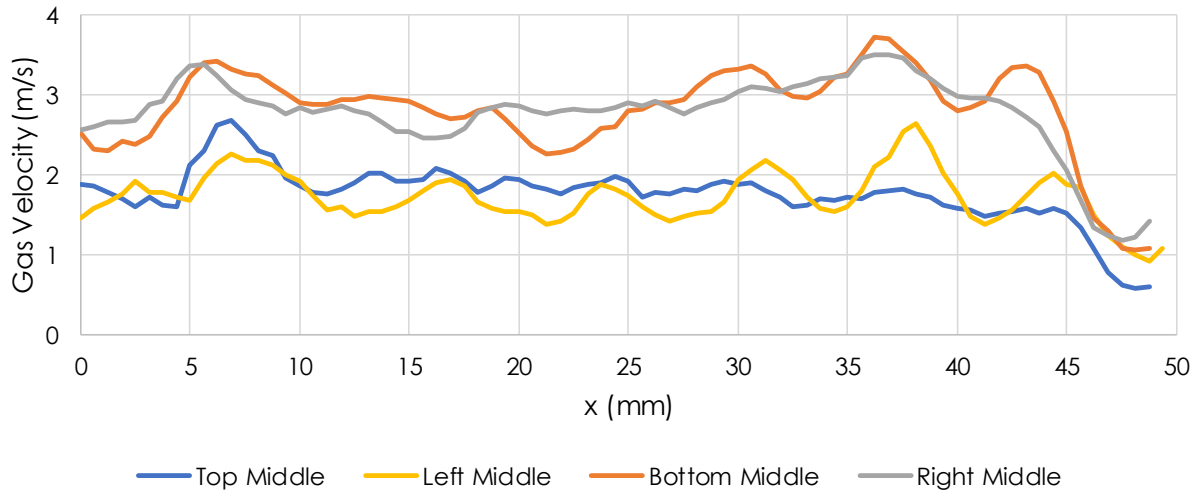

Figure 93 – Velocity profiles measured ex-situ under experimental flow conditions for the jet middle

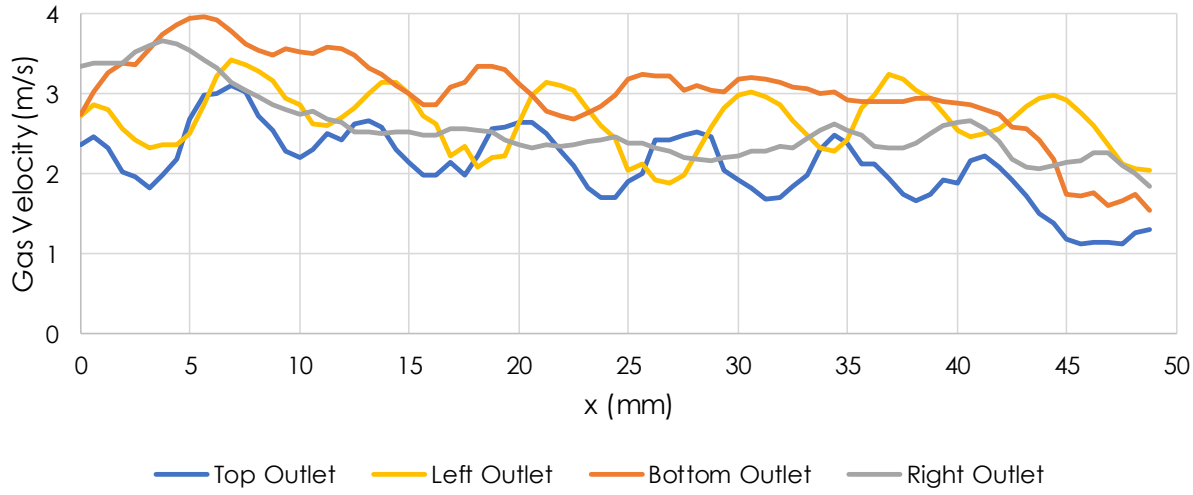

Figure 94 – Velocity profiles measured ex-situ under experimental flow conditions for the jet outlet

5.5. FINAL RESULTS

Two tests were run with the aforementioned experimental set up, both times with the cavity at 2150°C. The first test was run for 1 hour, and resulted in visible deposition on the unprotected samples, shown in Figure 95, but no visible deposition on the protected samples. The second test ran for 3 hours, and showed visible deposition on all the samples, shown in Figure 95, Figure 96, and Figure 97.

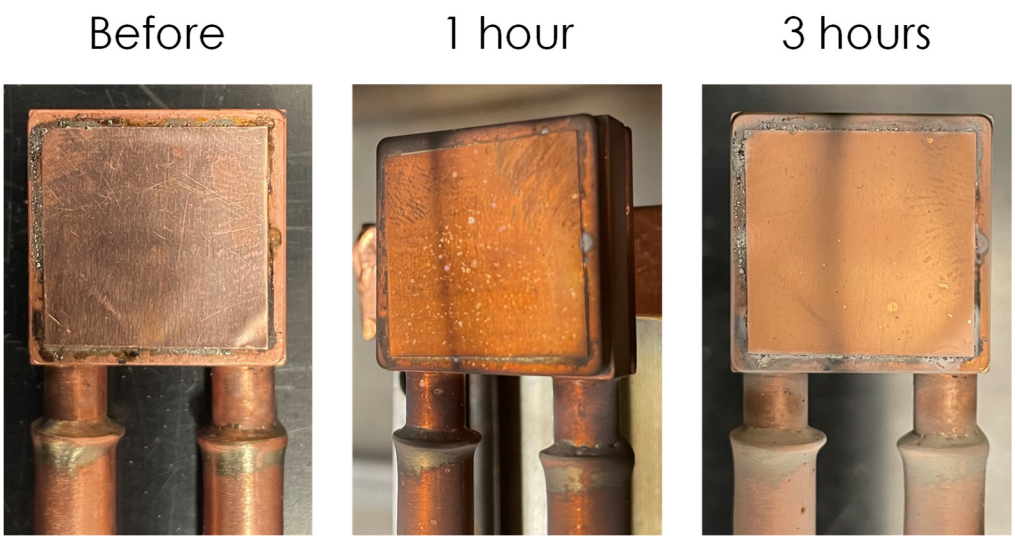

Figure 95 – Unprotected samples before and after a 1-hour test and a 3-hour test at 2150°C showing increasing amounts of deposition in the form of both black material and lighter material

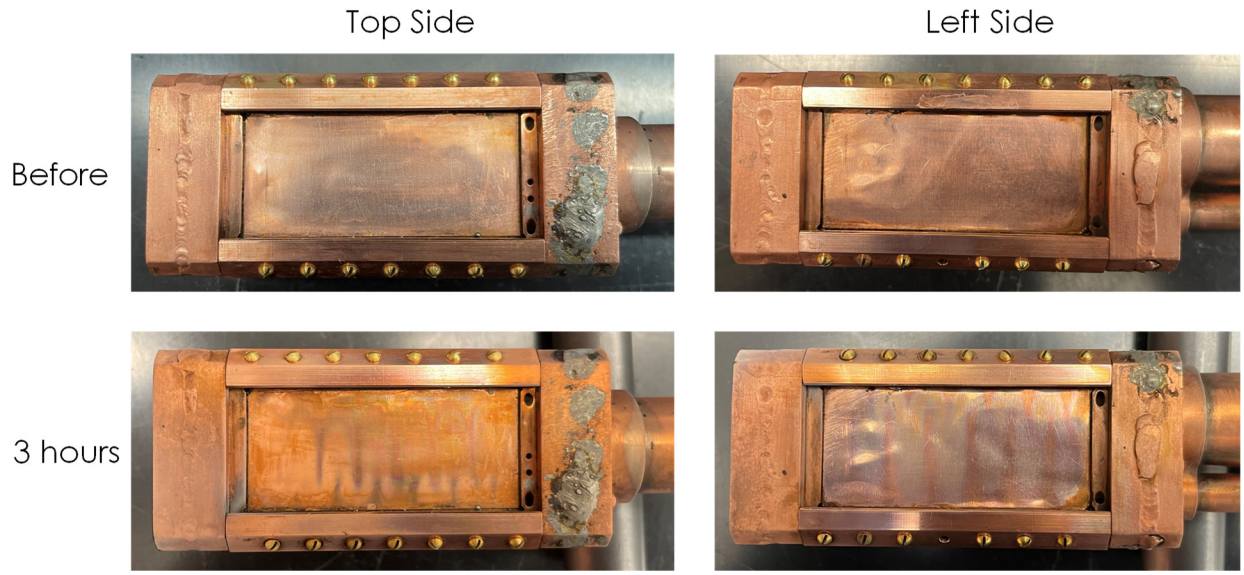

Figure 96 – Protected samples on the top and left side of the cold plate before and after a 3-hour test at 2150°C. Average middle velocity for the top and left sides was 1.75 m/s.

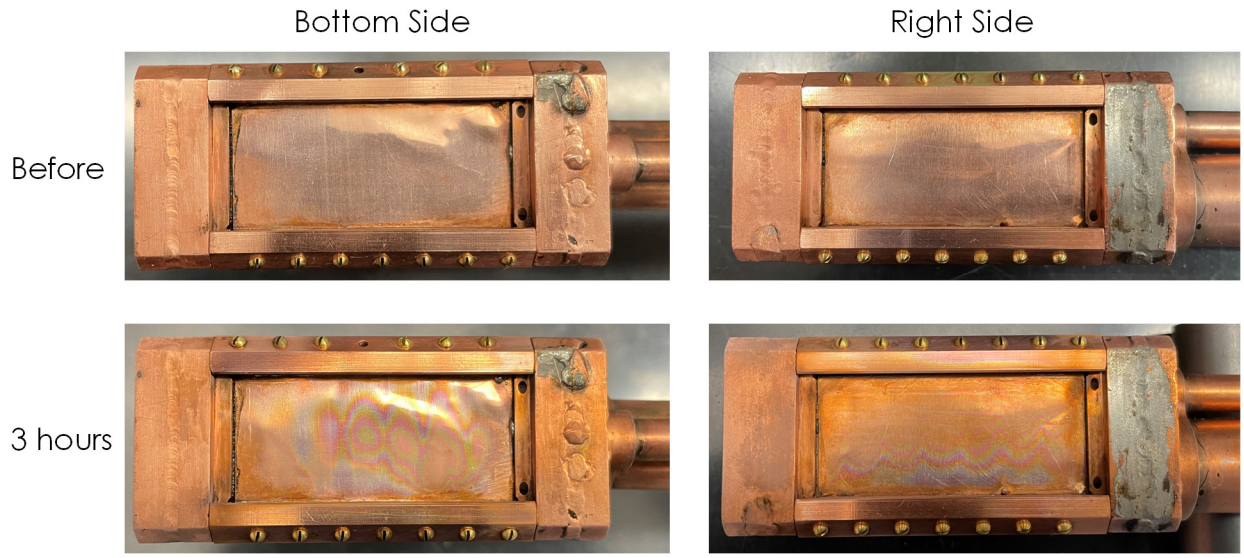

Figure 97 – Protected samples on the bottom and right side of the cold plate before and after a 3-hour test at 2150°C. Average middle velocity for the bottom and right sides was 2.80 m/s.

Cross-sectional SEM imaging was attempted for all of the samples, but no visible deposition layer was observed, even on the unprotected sample, shown in Figure 98. This is a good result, in that the impurity contamination seen in previous experimental runs seems to be resolved, but makes it challenging to evaluate the SNGC effectiveness quantitatively.

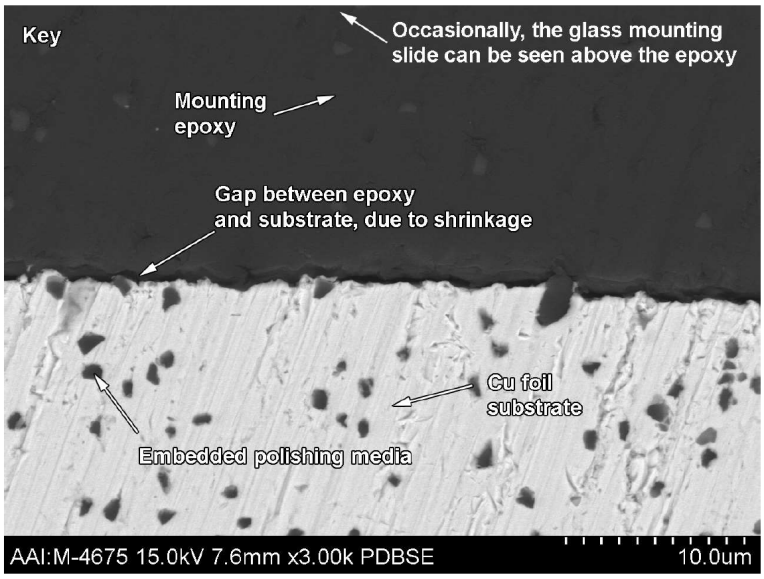

Figure 98 – X-sectional SEM measurements. No visible deposition on protected sample, even at micron scale.

In light of this measurement limitation, reflectivity of all the samples was measured to determine how the optical properties of the copper foil had changed. Figure 99 show the spectral reflectivity for the protected samples for the 3-hour test (1 standard deviation error bars), unprotected sample from the 1-hour test (3-hour test sample was consumed in SEM measurements), and a baseline copper foil sample. Also plotted is the normalized black body spectrum at 2150°C, showing the relative importance of each part of the spectrum. The average absorptance, integrated over the spectrum, of these three examples is also shown. These results clearly show a significant reduction in absorption for the protected region, compared to the unprotected region. Assuming all the deposited material is carbon, the expected thickness of a carbon layer that would cause the measured absorption was estimated using the method discussed in 2.3.1, using Eqs. (7)-(9). Assuming the deposition continued at the same rate beyond 1 hour, the expected thickness of the deposited layer on the unprotected sample would be roughly 3 times the estimated 29 nm for the 1-hour test. This would correspond to a reduction from 87 nm over 3 hours for the unprotected sample, to 4.7 nm over 3 hours for the protected sample. This 50x reduction in deposition is considered a profound success and justifies the addition of the SGNC to prevent TPV cell contamination.

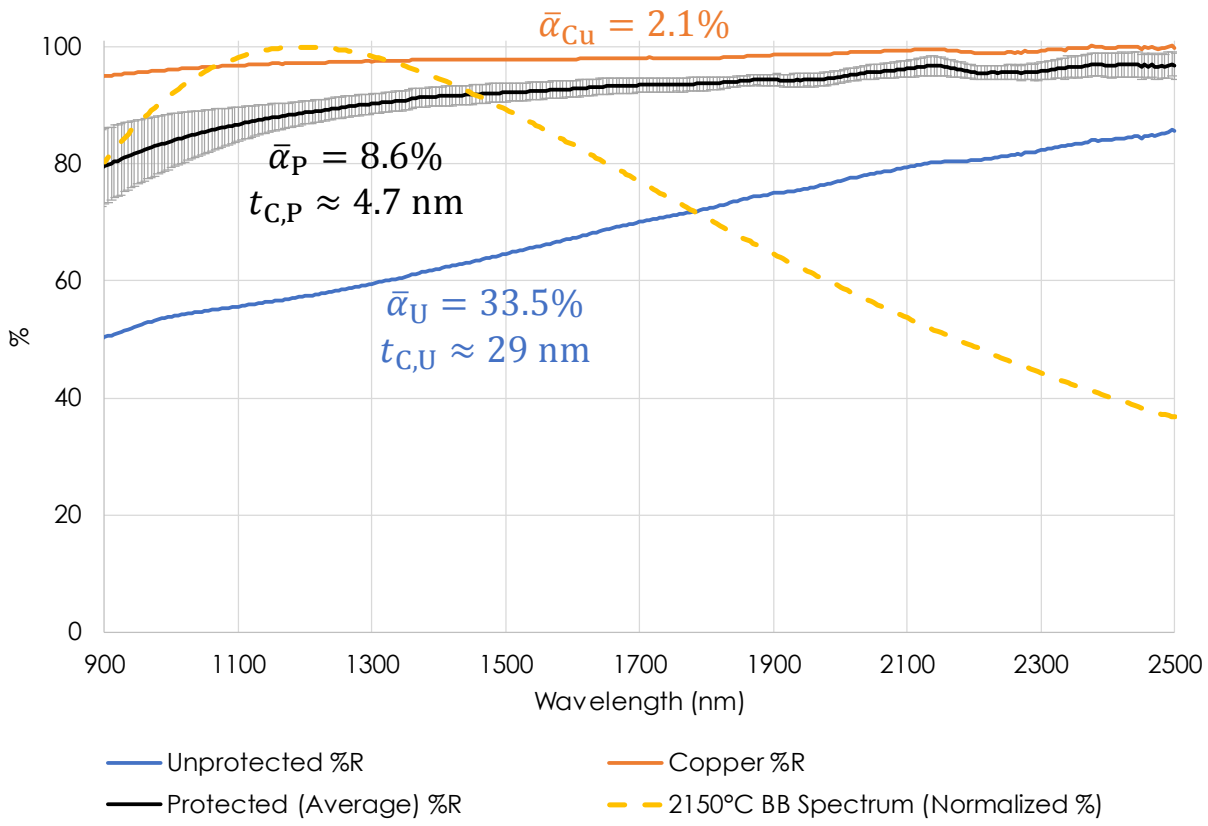

Figure 99 – Reflectance measurements for a clean copper sample, the SNGC protected foil samples (averaged, 1 s.d. error bars), and the unprotected sample. Average weighted absorptance over the shown wavelength band was also calculated, and the thickness of carbon deposition corresponding to that absorptance was calculated.

5.6. SUMMARY

This chapter describes the high-temperature testing apparatus used to evaluate the effectiveness of the SNGC integrated cold plate proposed in Chapter 4. It also highlights the unique experimental components required for this extreme testing environment, and also present the results of several tests. Through this testing, the effectiveness of the SGNC was indicated through primarily optical measurement techniques. These optical techniques could not measure deposition layer thickness directly, but based on the relative absorptions of a SNGC protected region and an unprotected region, a reduction in deposition rate of 50x is estimated. This represents a profound success and clearly shows the usefulness of the SNGC device in protecting TPV cells from deposition of sublimated emitter material.

Chapter 6

6. Summary, Future Work and Perspective

6.1. SUMMARY

This thesis presents a compilation of work towards a functional and scalable thermophotovoltaic energy converter for application in a grid-scale energy storage system. Topics include the challenges of ultra-high-temperature (>2000°C) experiments, the design process of both the "hot-side" thermal emitter and "cold-side" TPV cell cooling infrastructure, and the results of experiments testing all of the designed components. The chapters were organized as follows:

Chapter 1 discusses the changing energy landscape and how grid-scale energy storage is necessary to ensure a reliable grid heavy with intermittent renewable energy resources. Additionally, a new storage technology, Thermal Energy Grid Storage, is proposed and some of its key technological components are explained. A technoeconomic model shows that it has the potential to provide a low cost and geographically unconstrained alternative to current storage technologies.

Chapter 2 summarizes some of the challenges experienced developing ultra-high-temperature experiments. Solutions to several of these issues are also shown, which are in used to inform the design of a TPV emitter capable of operating at temperatures above 2000°C.

Chapter 3 presents several models predicting the behavior of a Sweeping Noble Gas Curtain (SNGC) approach to preventing TPV cell degradation, a problem common in high-temperature TPV systems. These models were validated using a low-temperature proxy experiment, and the experimental findings were used to inform the design of a high-temperature experimental device.

Chapter 4 highlights a number of design components of an SNGC integrated cold plate capable of keeping cells cool and clean in a >2000°C thermal emitter cavity. The challenges associated with the manufacturing of this integrated SNGC-TPV device are also discussed in detail.

Chapter 5 explains the experimental apparatus used for testing of the designed SNGC-TPV device and shows results from a number of tests. These tests showed the effectiveness of the device at preventing deposition in the region protected by the SNGC and suggests it could be a vital and useful part of a larger-scale system.

6.2. FUTURE WORK

6.2.1. Further Deposition Characterization

Some of the characterization of deposition rate was limited by the available measurement techniques. Further characterization of deposition rates for various different flow velocities and emitter materials could help tests the bounds of the SNGC approach. Operating at the lowest gas flow rates possible should minimize the parasitic power load of the gas blower. This could involve more careful measurement of deposited material thickness, using Focused Ion Beam or traditional SEM techniques. Identification of deposited species could also inform the optical calculation, to better estimate the thickness of deposited layer using the correct optical coefficients for the deposited material.

6.2.2. SNGC Uniformity Improvements

Though the average performance of the SGNC was good, there was visible variation in deposition rates at different locations on the measured samples. Further fluid flow studies and measurements could be done to improve the uniformity and ensure complete cell protection.

6.2.3. Longer Duration Testing

Longer duration testing, on the timescales of weeks or months, could also be useful in determining how the SGNC performs in a more accurate representation of the end use. The low deposition rate, even for the graphite emitter, makes for a challenging comparison for short test durations. Longer tests could both identify other, unforeseen system durability challenges. As the system is designed to operate for many years, it could be useful to identify these problems sooner rather than later in the design process.

6.2.4. TPV Module Integration

Another step towards a real implementation would be the incorporation of a full set of TPV cells, allowing for cell power measurements taken over time. This is by far the most relevant and accurate determination of deposition's impact on cell performance. These experiments, if run for sufficiently long durations, could conclusively prove the effectiveness of the SGNC at preventing cell contamination.

Additionally, based on discussions with a concentrated PV module fabrication company, TPV cell modules could be made with integrated microchannel heat sinks. This adaptation could allow for easier

replacement of damaged cells, compared to the solder-in-place approach used in the experimental section of this thesis. Figure 100 shows a potential iteration of this, designed for a commercial scale TEGS plant.

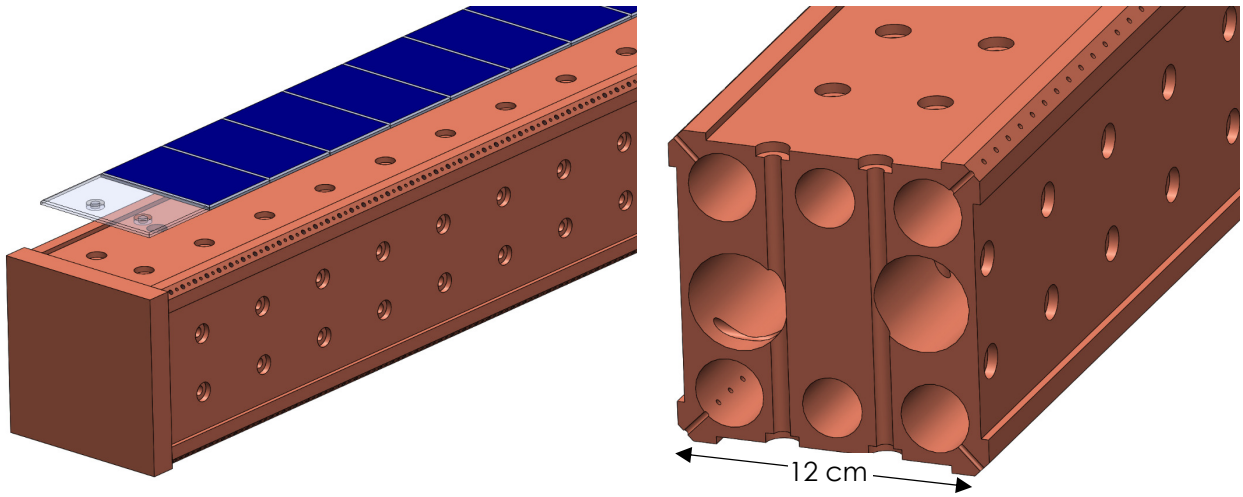

Figure 100 – TPV module including integrated microchannel heat sink, enabling non-soldering integration with cold plate core.

6.2.5. Scaling Up

The most apparent extension of the work presented in this thesis is the design and construction of a commercial scale TPV device based on the proposed designs. Adapting the experimental-scale system should be possible, as scalability was a major component of the design decision making process. Combining the TPV device with an actual storage block and molten tin loop would be helpful in proving the viability of the TEGS concept as a whole.

6.3. PERSPECTIVE

Energy storage is predicted to be an important component of a renewable and reliable grid, but existing storage technologies are insufficient to meet this need. The proposed Thermal Energy Grid Storage has the potential to achieve the cost and scale targets for widespread implementation, with a key enabling technology being a thermophotovoltaic heat engine. While these energy converters have been demonstrated in laboratory environments, the durability challenges of a commercial scale system have not been addressed. The discoveries and designs presented in this thesis represent a step towards this large-scale iteration of TPVs, and proposed a pathway towards the significant extension of TPV lifetimes and usefulness.

References

[1] U.S. Energy Information Administration, “Electricity Monthly Update - December 2021,” 2021.

[2] S. Robbins and D. Chu, “Energy Storage for Peaker Plant Replacement Presenters Energy Planner,” no. May, 2022.

[3] P. Denholm, E. Ela, B. Kirby, and M. Milligan, “NREL Technical Report: The Role of Energy Storage with Renewable Electricity Generation,” 2010.

[4] P. Albertus, J. S. Manser, and S. Litzelman, “Long-Duration Electricity Storage Applications, Economics, and Technologies,” *Joule*, vol. 4, no. 1, pp. 21–32, 2020.

[5] B. Dunn, H. Kamath, and J.-M. Tarascon, “Electrical Energy Storage for the Grid: A Battery of Choices,” *Mater. Grid Energy*, vol. 334, no. November, pp. 928–935, 2011.

[6] M. S. Ziegler *et al.*, “Storage Requirements and Costs of Shaping Renewable Energy Toward Grid Decarbonization,” *Joule*, vol. 3, no. 9, pp. 2134–2153, 2019.

[7] H. Thomas, A. Marian, A. Chervyakov, S. Stückrad, D. Salmieri, and C. Rubbia, “Superconducting transmission lines - Sustainable electric energy transfer with higher public acceptance?,” *Renew. Sustain. Energy Rev.*, vol. 55, pp. 59–72, 2016.

[8] MIT Energy Initiative, “The Future of Energy Storage,” 2022.

[9] C. Amy, H. R. Seyf, M. A. Steiner, D. J. Friedman, and A. Henry, “Thermal energy grid storage using multi-junction photovoltaics,” *Energy Environ. Sci.*, vol. 12, no. 1, pp. 334–343, 2019.

[10] A. Datas and A. Martí, “Thermophotovoltaic energy in space applications: Review and future potential,” *Sol. Energy Mater. Sol. Cells*, vol. 161, no. October 2016, pp. 285–296, 2017.

[11] A. LaPotin *et al.*, “Thermophotovoltaic efficiency of 40%,” *Nature*, vol. 604, no. 7905, pp. 287–291, 2022.

[12] Z. Omair *et al.*, “Ultraefficient thermophotovoltaic power conversion by band-edge spectral filtering,” *Proc. Natl. Acad. Sci. U. S. A.*, vol. 116, no. 31, pp. 15356–15361, 2019.

[13] Y. X. Yeng *et al.*, “Photonic crystal enhanced silicon cell based thermophotovoltaic systems,” *Opt. Express*, vol. 23, no. 3, p. A157, 2015.

[14] R. Sakakibara *et al.*, “Practical emitters for thermophotovoltaics: a review,” *J. Photonics Energy*, vol. 9, no. 03, p. 1, 2019.

[15] R. M. Swanson, “Recent Developments in Thermophotovoltaic Conversion,” in *Photovoltaic Solar Energy Conference*, 1981, p. 1097.

[16] Z. Wang *et al.*, “Selective emitter materials and designs for high-temperature thermophotovoltaic applications,” *Sol. Energy Mater. Sol. Cells*, vol. 238, no. July 2021, p. 111554, 2022.

[17] C. Amy, C. C. Kelsall, A. LaPotin, M. Pishahang, and A. Henry, “Chapter 3 - Ultrahigh temperature sensible heat storage and heat transfer fluids,” in *Ultra-High Temperature Thermal Energy Storage, Transfer and Conversion*, A. Datas, Ed. Woodhead Publishing, 2021, pp. 57–84.

[18] C. Amy *et al.*, “Pumping liquid metal at high temperatures up to 1,673 kelvin,” *Nature*, vol. 550, no. 7675, pp. 199–203, 2017.

[19] C. Amy, M. Pishahang, C. Kelsall, A. LaPotin, and A. Henry, “High-Temperature Pumping of Silicon for Thermal Energy Grid Storage,” *Energy*, p. 121105, Jun. 2021.

[20] C. Amy, “Thermal Energy Grid Storage: Liquid Containment and Pumping,” Massachusetts Institute of Technology, 2020.

[21] Kyocera, “Alumina (Aluminum Oxide, Al2O3),” 2013. [Online]. Available: http://www.makeitfrom.com/material-data/?for=Alumina-Aluminum-Oxide-Al2O3.

[22] International Tungsten Industry Association, “Tungsten Properties.” [Online]. Available: https://www.itia.info/tungsten-properties.html. [Accessed: 01-Jan-2018].

[23] Ohio Carbon Blank, “AR-14 Graphite.” [Online]. Available: https://www.ohiocarbonblank.com/.

[24] C. V. Thompson, “Ellingham Diagrams [Class Handout].” 2016.

[25] A. H. P. Skelland, *Diffusional Mass Transfer*. Malabar, Florida: Krieger Publishing Company, 1974.

[26] D. F. O. H. Tsung Chen, “Correlating diffusion coefficients in binary gas systems use of viscosities in a new equation and nomogram,” *Ind. Eng. Chem. Process Des. Dev.*, vol. 1, no. 4, pp. 249–254, Oct. 1962.

[27] A. D. Rakić, A. B. Djurišić, J. M. Elazar, and M. L. Majewski, “Optical properties of metallic films for vertical-cavity optoelectronic devices,” *Appl. Opt.*, vol. 37, no. 22, p. 5271, 1998.

[28] G. Cheng, “Energy Transfer By Waves,” in *Nanoscale Energy Transport and Conversion: A Parallel Treatment of Electrons, Molecules, Phonons, and Photons*, pp. 159–226.

[29] Y. S. Touloukian and D. P. DeWitt, “Thermal Radiative Properties: Metallic Elements and Alloys,” *Thermophys. Prop. Matter, Vol.7*, p. 1599, 1970.

[30] D. Olson, “Mineral Commodity Summaries 2022 - Graphite,” 2022.

[31] K. B. Shedd, “Industrial Mineral Surveys 2022 - Tungsten,” 2022.

[32] C. P. Buhsmer and P. H. Crayton, “Carbon self-diffusion in tungsten carbide,” *J. Mater. Sci.*, vol. 6, no. 7, pp. 981–988, 1971.

[33] C. Song, X.-S. Kong, and C. S. Liu, “First-principles studies on carbon diffusion in tungsten,” *Chinese Phys. B*, vol. 28, no. 11, 2019.

[34] P. S. Liu and G. F. Chen, “Making Porous Metals,” in *Porous Materials*, 2014, pp. 21–112.

[35] R. S. Bunker, “A Review of Shaped Hole Turbine Film-Cooling Technology,” *J. Heat Transfer*, vol. 127, no. 4, p. 441, 2005.

[36] B. R. Bird, W. E. Stewart, and E. N. Lightfoot, *Transport Phenomena*, 2nd ed. John Wiley & Sons, 2007.

[37] M. B. Glauert, “The wall jet,” *J. Fluid Mech.*, vol. 1, no. 06, p. 625, 1956.

[38] Mikros Technologies, “M2 Cold Plate Datasheet.”